Dissertation

submitted to the

Combined Faculty of Mathematics, Engineering and Natural Sciences

of Heidelberg University, Germany

for the degree of

Doctor of Natural Sciences

Put forward by

M.Sc. Luz Anny Pamela Ochoa Parra

born in: Bogotá, Colombia

Oral examination: July 8, 2025

Signal analysis in ion treatment monitoring with charged nuclear fragments – A simulation study

Referees: Prof. Dr. Oliver Jäkel

Prof. Dr. Mark E. Ladd

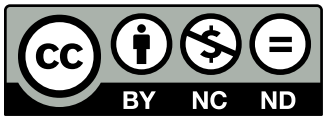

Abstract

Carbon-ion radiotherapy (CIRT) offers highly localized dose delivery and enhanced biological effectiveness. However, its precision also makes it highly sensitive to anatomical changes between treatment fractions. In-vivo monitoring of the dose delivery via detection of secondary radiation has emerged as a non-invasive method for assessing such changes.

The ongoing InViMo clinical trial conducted at the Heidelberg Ion-Beam Therapy Center (HIT) and the German Cancer Research Center is evaluating the feasibility of identifying and localizing anatomical changes in patients with skull base tumors by measuring the localization of the primary carbon ions' breakup (fragments) in the patient. The results are very promising to date. For this purpose, a monitoring system composed of seven mini-trackers was designed and developed in order to measure fragment tracks outside the patient. Interpreting the signals proved highly complex, highlighting the need for access to physical quantities that cannot be measured experimentally, such as the true origin of the fragments.

The primary objective of this thesis was to develop, validate, and implement a Monte Carlo (MC) simulation framework for in-vivo monitoring of CIRT. The developed simulation framework, based on the FLUKA MC code, was first validated against experimental data using a single mini-tracker. Thereafter, the framework was extended to simulate the full monitoring system, comprising the seven mini-trackers, and integrated into FICTION, a CT-based dose calculation Monte Carlo environment developed at HIT. It was used to simulate a cohort of eight patients treated at HIT, including retrospective cases, patients from the InViMo study, and a prostate cancer case, all under realistic clinical conditions. Signal analysis demonstrated that shallow anatomical changes, such as nasal swelling or cavity filling, were successfully detected and localized using reconstructed fragment origin. Deep-seated changes, those distant from the detector or near the end of the beam range proved more challenging to resolve. For the prostate case, the signal from the clinical InViMo detection system was found not to be sufficient to capture the changes in the rectal filling. Therefore, an alternative in-table detection system was designed using the simulation framework. A significant improvement in the detectability of such changes was demonstrated. These results highlight the framework's versatility.

In conclusion, an MC–based simulation environment for studying in-vivo treatment monitoring in carbon-ion therapy was established and validated in this thesis. By enabling detailed modeling of the fragment creation and tracking in patient-specific geometries, the framework can be used for a deeper understanding of the complex clinical signal and for the optimization of monitoring strategies. Its flexibility across anatomical sites makes it a highly valuable tool for future investigations of the clinical potential of fragment-based treatment verification.

Zusammenfassung

Die Kohlenstoffionen-Strahlentherapie (CIRT) ermöglicht eine hochlokalisierte Dosisverteilung und eine erhöhte biologische Wirksamkeit. Ihre Präzision macht sie jedoch auch besonders empfindlich gegenüber anatomischen Veränderungen zwischen den einzelnen Behandlungsfraktionen. Das in-vivo Monitoring der Dosisverteilung durch die Detektion sekundärer Strahlung hat sich als nicht-invasiver Ansatz zur Bewertung solcher Veränderungen etabliert.

Die laufende InViMo-Studie, die am Heidelberger Ionenstrahl-Therapiezentrum (HIT) und am Deutschen Krebsforschungszentrum durchgeführt wird, untersucht die Machbarkeit der Identifikation und Lokalisierung anatomischer Veränderungen bei Patient*innen mit Schädelbasistumoren durch Messung der Lokalisation des Zerfalls (Fragmente) der primären Kohlenstoffionen im Patienten. Die bisherigen Ergebnisse sind sehr vielversprechend. Zu diesem Zweck wurde ein Monitoringsystem, bestehend aus sieben Mini-Trackern, entworfen und entwickelt, um Fragmentspuren außerhalb des Patienten zu messen. Die Interpretation der Signale erwies sich als hochkomplex und verdeutlicht die Notwendigkeit des Zugriffs auf physikalische Größen, die experimentell nicht gemessen werden können, wie z. B. der wahre Ursprung der Fragmente.

Das Hauptziel dieser Arbeit war die Entwicklung, Validierung und Implementierung eines Monte-Carlo-(MC)-Simulationsframeworks für das in-vivo Monitoring der CIRT. Das entwickelte Simulationsframework, basierend auf dem FLUKA-MC-Code, wurde zunächst anhand experimenteller Daten unter Verwendung eines einzelnen Mini-Trackers validiert. Anschließend wurde das Framework erweitert, um das vollständige Monitoringsystem, bestehend aus den sieben Mini-Trackern, zu simulieren, und in FICTION integriert, einer CT-basierten Monte-Carlo-Umgebung zur Dosisberechnung, die am HIT entwickelt wurde. Es wurde verwendet, um eine Kohorte von acht am HIT behandelten Patientinnen zu simulieren, darunter retrospektive Fälle, Patientinnen aus der InViMo-Studie und ein Fall mit Prostatakrebs, alle unter realistischen klinischen Bedingungen. Die Signalanalyse zeigte, dass oberflächennahe anatomische Veränderungen, wie Nasenschwellung oder das Auffüllen von Hohlräumen, erfolgreich erkannt und lokalisiert wurden, basierend auf dem rekonstruierten Fragmentursprung. Tiefsitzende Veränderungen, solche in größerer Entfernung vom Detektor oder in der Nähe des Reichweitenendes des Strahls, erwiesen sich als schwieriger zu erfassen. Im Prostatakrebsfall erwies sich das Signal des klinischen InViMo-Detektionssystems als nicht ausreichend, um die Veränderungen in der Rektumfüllung zu erfassen. Daher wurde mit dem Simulationsframework ein alternatives Detektionssystem im Behandlungstisch entworfen. Eine signifikante Verbesserung der Detektierbarkeit solcher Veränderungen konnte demonstriert werden. Diese Ergebnisse unterstreichen die Vielseitigkeit des Frameworks.

Zusammenfassend wurde in dieser Arbeit eine MC-basierte Simulationsumgebung zur Untersuchung des in-vivo Monitorings in der Kohlenstoffionentherapie etabliert und validiert. Durch die detaillierte Modellierung der Fragmenterzeugung und -verfolgung in patient*innenspezifischen Geometrien kann das Framework für ein besseres Verständnis des komplexen klinischen Signals und zur Optimierung von Monitoringstrategien eingesetzt werden. Seine Flexibilität über anatomische Regionen hinweg macht es zu einem äußerst wertvollen Instrument für zukünftige Untersuchungen zum klinischen Potenzial der fragmentbasierten Behandlungsverifikation.

Contents

Chapter 1

Introduction

Carbon-Ion Radiotherapy

Ion-beam therapy offers precise tumor targeting while sparing healthy tissues. Unlike conventional photon-based radiotherapy, which deposits energy continuously along its path, ion beams exhibit a steep dose fall-off beyond the target, reducing unnecessary radiation exposure to adjacent organs [1].

Among the clinically available ion-beam therapies—proton, carbon, and helium ions—carbon-ion radiotherapy (CIRT) stands out due to its superior physical and biological properties. The higher mass of carbon ions reduces lateral scattering, resulting in a more confined dose distribution compared to protons. This makes CIRT particularly effective for tumors near critical structures, where precision is essential. Additionally, carbon ions have a higher relative biological effectiveness (RBE), particularly in hypoxic and radio-resistant tumors, where conventional radiotherapy often fails [2]. These properties have made CIRT a preferred modality for head and neck cancers, skull base tumors, and central nervous system malignancies, where precise dose delivery is crucial.

Despite these advantages, the steep dose gradients of CIRT introduce significant treatment challenges. Unlike photon-based radiotherapy, where dose deposition is more distributed, CIRT relies on anatomical stability throughout treatment. Even small anatomical variations, such as tumor shrinkage, weight loss, tissue swelling, or air cavity changes, can cause substantial deviations between the planned and actual dose distributions [3]. These variations may lead to tumor underdosage, reducing treatment efficacy, or excessive irradiation of healthy tissues, increasing the risk of complications.

Safety margins are applied around the tumor to address these uncertainties, compensating for potential anatomical changes. However, this strategy increases the volume of irradiated healthy tissue, raising the likelihood of radiation-induced side effects [4]. While safety margins help manage unpredictable inter-fractional changes, they do not provide a systematic method to determine when and how anatomical variations significantly impact dose distribution. A treatment verification approach is needed to monitor these changes, guiding adaptive treatment strategies to ensure optimal dose delivery throughout therapy [5].

Carbon-Ion Radiotherapy Treatment Monitoring

Various in-vivo monitoring approaches have been developed, primarily relying on the detection of secondary radiation produced during ion-beam interactions with tissue [6, 7]. Positron emission tomography (PET), which detects $\beta+$ emitters generated by nuclear interactions to infer beam range. While PET-based monitoring has been implemented in clinical environments at the National Center for Oncological Hadrontherapy (CNAO) in Italy [8] and at the National Institutes for Quantum Science and Technology (QST) in Japan [9, 10], it suffers from biological washout effects, long acquisition times, and low signal yield, which limit its effectiveness. Another method is prompt gamma imaging (PGI), where high-energy γ-rays emitted during irradiation are used to estimate beam stopping position. However, in CIRT, PGI has low detection efficiency, making its clinical applicability challenging [11].

A promising alternative for CIRT treatment verification is charged secondary ion tracking, which focuses on detecting nuclear fragments produced in the patient during treatment [12]. The use of charged nuclear fragments for in-vivo monitoring has been explored in multiple experimental and simulation studies by our research group at the German Cancer Research Center (DKFZ) [13–18]. To further investigate its feasibility in clinical CIRT, our research group developed a clinical tracking system employing seven 4-chip Timepix3 mini-trackers [19]. This clinical detection system is currently used in the In-Vivo Monitoring (InViMo) clinical trial at the Heidelberg Ion-Beam Therapy Center (HIT) in Germany [20]. The clinical trial focuses on monitoring patients with skull base tumors undergoing CIRT, aiming to assess the capability of charged nuclear fragment tracking for in-vivo monitoring in clinical scenarios.

The core of this monitoring approach is the reconstruction of fragmentation vertices -the origin points of nuclear fragments within the patient- over multiple treatment sessions. By comparing fragment distribution patterns across different fractions, the system aims to identify inter-fractional anatomical changes that may affect treatment accuracy. However, accurately interpreting fragment data is a major challenge due to multiple Coulomb scattering (MCS) [21], fragment absorption in tissue, and variations in tissue density. These factors influence the detected fragment yield and distribution, making it difficult to directly correlate observed signals with anatomical changes directly.

Motivation: MC -Based Simulation Framework for CIRT Monitoring

This thesis focused on developing a Monte Carlo-based framework for treatment monitoring in carbon-ion radiotherapy (CIRT) to support the experimental effort. As a first step, a single mini-tracker unit (AdvaPIX TPX3 Quad) was implemented in FLUKA and validated experimentally through measurements of secondary nuclear fragments, as described in [22]. Building on this, the full clinical setup comprising seven mini-trackers, reflecting the detection system used in the InViMo trial, was modeled in FLUKA. This extended implementation was coupled with FICTION (FLUKA Integrated Framework for CT-based calculations in Ion Therapy) [23, 24], a framework developed at HIT that enables CT-based Monte Carlo simulations of CIRT monitoring in clinical scenarios. The framework's clinical applicability was initially evaluated with simulations performed on an anthropomorphic

head phantom, in which an anatomical modification was introduced in the nasopharynx to mimic an inter-fractional density change. The results showed good agreement with experimental data, confirming the validity of the framework [18].

A key contribution of this thesis is the simulation of a cohort of eight patients treated with CIRT at HIT, using the developed FLUKA Monte Carlo-based CIRT monitoring workflow (see Section 3.2.4). For each patient, two simulations were performed: one using the planning CT and another using a follow-up CT acquired later in the treatment course to account for inter-fractional anatomical variations. The primary goal of these simulations was not only to replicate secondary ion production and emission tracking but also to access information that cannot be obtained from measurements alone, such as the true origin of fragmentation vertices, heavy ion nuclear interaction points (HINIs), and physical dose distributions. This simulation-derived data provides essential context for interpreting clinical measurements, enabling a more accurate understanding of fragment signal formation. In particular, it allows the correlation of inter-fractional anatomical changes, quantified as differences in Hounsfield Units (HU) between CT scans, with the Monte Carlo-predicted fragment and dose distributions.

Moreover, as the clinical detection system was tailored for head and neck treatments, a new in-table monitoring setup was developed using seven AdvaPIX TPX3 Quad mini-trackers (see Section 3.2.3). This configuration enables integration into treatment positions beyond the head region and shows potential for extension to other tumor sites treated with CIRT, such as pelvic tumors. The results presented in this work demonstrate the capability of the developed simulation framework to support the interpretation of secondary fragment signals in clinical workflows and to contribute toward the development of adaptive strategies for treatment verification.

Chapter 2

Theoretical Background

2.1 Fundamental Interactions of Charged Particles

In ion beam radiotherapy, charged particles such as carbon ions must be accelerated to therapeutic energies, typically in the range of 100 to $400\,\mathrm{MeV/u}$, to ensure adequate penetration into tissue. These ions are guided and accelerated using electromagnetic fields, a process governed by the Lorentz force:

$$\vec{F}_{\text{Lorentz}} = q(\vec{E} + \vec{v} \times \vec{B}) \tag{2.1}$$

where q is the particle charge, $\vec{E}$ is the electric field, $\vec{B}$ is the magnetic field, and $\vec{v}$ is the particle velocity. This principle underlies particle acceleration, magnetic beam steering, and beam shaping systems used in clinical facilities.

Once delivered to the patient, carbon ions interact with matter primarily through electromagnetic and nuclear forces. The main interactions responsible for energy loss in tissue are:

- **Ionisation and excitation:** The dominant mechanism at therapeutic energies, where energy is transferred to atomic electrons via inelastic collisions.
- **Elastic nuclear scattering:** The ion is deflected by the Coulomb field of nuclei with minimal energy loss, resulting in angular spread and beam broadening.
- **Inelastic nuclear interactions:** Collisions that result in nuclear fragmentation and the production of secondary particles.

Due to their velocity-dependent energy loss, carbon ions deposit energy non-uniformly along their track. The energy loss per unit length increases as the particle slows down, culminating in a sharp maximum near the end of its range known as the Bragg peak. This feature is characteristic of all charged hadrons but is more pronounced for heavier ions such as carbon, owing to reduced range straggling and lateral scattering. Range straggling refers to statistical fluctuations in energy loss and penetration depth, while lateral scattering describes angular deviations caused primarily by multiple Coulomb interactions [25]. The resulting depth-dose curve consists of a gradual entrance region (plateau), a sharp Bragg peak, and a steep fall-off. Nuclear interactions and range straggling contribute to the peak's finite width and the low-dose tail beyond it, as seen in the Figure2.1.

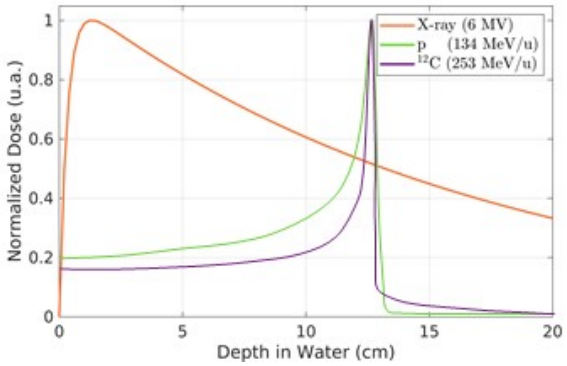

Figure 2.1. Normalized depth dose for 6 MV X-rays, 134 MeV/u protons, and 253 MeV/u carbon ions. The curves are sketched based on approximated data and do not represent measured or simulated values, and are presented for illustrative purposes only.

Stopping Power and Energy Deposition The Bragg peak and depth-dose distribution characteristic of ion beams arise from the velocity-dependent energy deposition along the particle track. This phenomenon is quantified by the *stopping power* S [26], defined as the mean energy loss per unit path length of a charged particle:

$$S = -\frac{dE}{dx} = S_{\text{el}} + S_{\text{nuc}} + S_{\text{rad}} \tag{2.2}$$

For heavy charged particles such as carbon ions, the dominant contribution to stopping power at therapeutic energies is due to inelastic interactions with atomic electrons, referred to as *electronic stopping power* S_{el}. Additional contributions include nuclear stopping power (S_{nuc}), from elastic collisions with nuclei, and radiative stopping (S_{rad}), associated with bremsstrahlung, though both are negligible at these energies. The electronic stopping power is often expressed in its mass-specific form, normalized by the material density ρ, called mass electronic stopping power (S_{el}/ρ):

$$\frac{S_{el}}{\rho} = \left(-\frac{dE}{\rho dx}\right)_{\text{el}} = K\frac{Zz^2}{A\beta^2}\left[\ln\left(\frac{2m_e c^2\beta^2\gamma^2 W_{\max}}{I^2}\right) - 2\beta^2 - \delta - \frac{C}{Z}\right], \tag{2.3}$$

where $K = 0.1535\,\text{MeV}\,\text{cm}^2/\text{mol}$ is the coefficient for stopping powers derived from physical constants, z is the charge of the incident ion, Z, A, and I are the atomic number, mass number, and mean excitation potential of the medium, m_e is the electron mass, c is the speed of light in vacuum, $\beta = v/c$ and $\gamma = 1/\sqrt{1-\beta^2}$ are the relative velocity and Lorentz factor, $W_{\max}$ is the maximum energy transferable to a single electron, δ accounts for medium polarization at high β (density effect correction), and C is the shell correction associated with electron binding in inner shells.

Equation 2.3 reveals several key dependencies. First, stopping power is inversely proportional to β^2, explaining the rise in energy deposition as particles slow down. At relativistic energies, after reaching a minimum around $\sim 1000\,\text{MeV/u}$, the stopping power begins to increase again due to relativistic effects. Second, the z^2 scaling illustrates the much higher stopping power of heavier ions like carbon compared to protons. Third, the stopping power is also proportional to Z/A of the target, reflecting the number of electrons per unit mass: this implies lower stopping power in high-Z media such as bone. Additionally, the logarithmic dependence on $W_{\max}$ and the I parameter demonstrates the sensitivity

to the medium's electron structure. Importantly, this formulation, which integrates soft and hard collision regimes, is independent of an arbitrary cutoff energy W_c, making it suitable for a wide range of ion types.

2.1.1 Multiple Coulomb Scattering

Charged particles undergo elastic scattering by atomic nuclei via the Coulomb force. While a single scattering event produces a small angular deviation, the cumulative effect of many such interactions is known as Multiple Coulomb Scattering (MCS).

The root-mean-square scattering angle θ_0 is approximated by:

$$\theta_0 = \frac{13.6\ \text{MeV}}{\beta cp} z \sqrt{\frac{x}{X_0}} \left[1 + 0.038 \ln\left(\frac{x}{X_0}\right)\right] \tag{2.4}$$

where p is the momentum of the incident particle, x the thickness of the traversed material, and X_0 the radiation length of the medium. This angular spread can degrade the spatial precision of the beam, though it is less pronounced for carbon ions compared to lighter charged particles, owing to their greater mass and momentum.

2.1.2 Nuclear Interactions and Fragmentation

When carbon ions interact inelastically with the nuclei of the medium, nuclear fragmentation may occur. These reactions are governed by complex nuclear physics, and their cross-sections depend on energy, target composition, and the structure of the projectile ion.

The fragmentation process is commonly described by the abrasion-ablation model. During the *abrasion* phase, the peripheral nucleons of both projectile and target are stripped due to their geometric overlap. The excited remnants then de-excite in the *ablation* phase via emission of nucleons, light fragments, and gamma radiation.

Secondary fragments produced include protons, neutrons, alpha particles, and light ions ($Z < 6$). These have broader angular distributions and longer ranges than the primary ions, contributing to a dose tail beyond the Bragg peak. While the contribution to total dose is modest, it introduces uncertainties in distal edge definition.

Fragmentation processes are crucial for both dose calculation and treatment monitoring, as some fragments exit the patient and can be detected externally.

2.2 Carbon-Ion Therapy

2.2.1 Overview and Clinical Advantages

Carbon-ion therapy (CIT) offers distinct physical and biological advantages over conventional photon and proton radiotherapy. These benefits derive from the fundamental properties of carbon ions and have been systematically outlined in both theoretical and clinical studies [27].

From a physical perspective, ion-beam therapy enables highly localized dose delivery via the Bragg peak phenomenon. In contrast to photons, which deposit energy exponentially

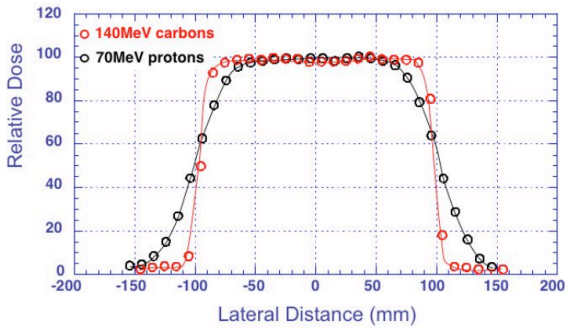

Figure 2.2. Lateral penumbra of 140 MeV/u carbon ions and 70 MeV protons. Reprinted from [30].

with depth, charged particles exhibit a sharp increase in energy deposition at the end of their range, allowing high tumor doses while minimizing exposure to surrounding normal tissues. This depth-selective deposition is enhanced in carbon ions due to their reduced range straggling, approximately a factor of $\sim 1/\sqrt{12} \approx 3.5$ compared to protons, resulting in a narrower Bragg peak and improved longitudinal dose conformity, as illustrated in Figure 2.1.

Carbon ions also exhibit less lateral spread due to their higher mass and reduced susceptibility to multiple Coulomb scattering (MCS). This yields a narrower lateral penumbra relative to protons [28, 29], improving dose conformity in all three dimensions. Figure 2.2 illustrates the comparative lateral dose profiles for carbon and proton beams [30].

On the biological side, carbon ions possess high linear energy transfer (LET), which induces dense ionization clusters along the track. This leads to complex DNA damage, particularly double-strand breaks, that are less amenable to cellular repair mechanisms. The relative biological effectiveness (RBE) of carbon ions is significantly higher than that of photons or protons, typically ranging from 1.3 to 5, depending on LET, cell type, and biological endpoint [31]. Notably, the RBE increases along the beam path, peaking near the Bragg maximum and enhancing the peak-to-plateau dose ratio.

A further radiobiological advantage of carbon ions is their reduced oxygen enhancement ratio (OER). High-LET radiation, such as carbon ions, is less dependent on oxygen concentration to induce lethal damage, whereas low-LET radiation (e.g., photons or protons) typically relies on oxygen to enhance radiation effectiveness. Therefore, carbon-ion therapy maintains efficacy even in hypoxic tumor regions that are typically resistant to low-LET radiation [27].

2.2.2 Clinical Challenges: Range Uncertainty and Anatomical Changes

Despite these benefits, the precision of carbon-ion therapy also renders it particularly vulnerable to treatment uncertainties. Even small deviations in patient setup or internal anatomy can lead to significant variations in the deposited dose due to the steep dose gradients and the range-dependent nature of ion beams [4].

Treatment precision is further challenged by systematic and random uncertainties. Systematic uncertainties, which affect every treatment fraction in the same way, originate primarily in the planning phase. These include image artefacts and limited resolution in the

planning CT [32], as well as uncertainties in converting Hounsfield units (HU) to stopping power, which introduce range errors of approximately ∼1 mm and dose uncertainties of 2–3% on average, increasing to 6.3% for head-and-neck cases [33, 34]. An additional and substantial contributor is biological modeling: the RBE-weighted dose is sensitive to inter-model differences (e.g., LEM vs. MKM), patient-specific factors, and tumor heterogeneity. RBE prediction uncertainties can reach 20–30% [35], and simulations have shown resulting variations in dose delivery of up to ∼40% [36]. Due to this variability, most carbon-ion centers use fixed RBE values in planning, although biologically optimized treatment is under active research.

Patient positioning must also be reproduced with high accuracy across all treatment fractions. Although robotic treatment couches can achieve sub-millimeter precision, as reported at HIT in [37], residual setup uncertainties still contribute to the overall dose deviation.

Random uncertainties vary between treatment fractions and can originate from both physiological and anatomical changes. These include respiration, heartbeat, and intra-fractional organ motion, as well as inter-fractional changes such as tumor shrinkage, inflammation, or patient weight loss. For instance, studies have reported body weight reductions of approximately 3–8 kg (up to 10%) and mean PTV shrinkage as high as ∼150 cm^3 in head-and-neck cancer patients during treatment. Such anatomical changes may lead to misalignment of the Bragg peak, causing underdosage of the tumor or overdosage of adjacent tissues.

To address these challenges, carbon-ion therapy incorporates carefully defined safety margins. According to ICRU Report 93 (2016) [34], treatment planning involves a hierarchy of volumes: the gross tumor volume (GTV), which represents the visible tumor; the clinical target volume (CTV), accounting for microscopic extension; and the planning target volume (PTV), which adds margins to compensate for positioning and anatomical uncertainties. In some cases, an internal target volume (ITV) is introduced to cover expected internal motion. Although standard CTV-to-PTV margins are typically 2–3 mm in carbon-ion therapy [4], these still increase the irradiated volume of healthy tissue and can lead to dose heterogeneity, including hot and cold spots in both the CTV and adjacent organs at risk (OARs).

Given the sensitivity of carbon-ion therapy to anatomical and positional variability, active research is ongoing to develop monitoring strategies capable of detecting and compensating for such changes either in real time or between treatment fractions. In the following section, the most prominent monitoring techniques are introduced, along with their physical principles, advantages, limitations, and current stage of development.

2.3 Monitoring Methods

Monitoring the patient's anatomy and detecting anatomical changes as early as possible is essential for maintaining treatment accuracy. However, routine imaging is not performed for every patient, as it would increase both radiation exposure and clinical workload. Imaging is typically reserved for cases where significant changes are expected, increasing the risk of undetected variations. To address this, various in-vivo monitoring techniques are under investigation. These methods aim to detect changes during irradiation by analyzing signals generated within the patient, based on the assumption that anatomical modifications affect

measurable secondary emissions, as described in the following.

2.3.1 Positron Emission Tomography (PET)

Positron Emission Tomography (PET) is one of the most studied techniques for in-vivo monitoring of ion beam range during carbon-ion therapy. When carbon ions interact with tissue, nuclear fragmentation leads to the production of positron-emitting isotopes, such as ^{10}C, ^{11}C, ^{13}N, and ^{15}O. These β^+ emitters decay by releasing a positron, which subsequently annihilates with an electron, resulting in the emission of two 511 keV photons in approximately opposite directions. By detecting these coincident photons, a spatial distribution of the activity can be reconstructed, providing an indirect estimate of the ion beam path within the patient [38, 39].

Three acquisition modalities exist for PET-based monitoring: in-beam (during irradiation) [40], in-room (immediately after irradiation within the treatment room) [41], and offline (after patient transport to a separate PET scanner) [42]. In-beam PET requires dedicated detectors capable of acquiring data between beam spills, while in-room and offline PET can use standard clinical PET/CT scanners.

Compared to proton therapy, PET monitoring of carbon-ion beams is more favorable, as β^+ emitters originate from both the projectile and target fragmentation. This dual contribution provides better correlation with the beam range [42]. However, PET imaging also faces several limitations. First, the temporal resolution is constrained by the half-lives of the isotopes, which range from seconds to minutes, e.g., $t_{1/2}(^{10}\mathrm{C}) =\sim 20\,\mathrm{s}$ and $t_{1/2}(^{11}\mathrm{C}) =\sim 20.4\,\mathrm{min}$. As a result, signal decay and biological washout can significantly alter the measured activity distribution within minutes of irradiation [38]. Second, the residual kinetic energy of the positrons introduces spatial blurring due to their travel before annihilation, degrading the effective resolution of the image [43].

Another major limitation is the relatively low yield of annihilation photons, especially in carbon-ion therapy, where fewer particles are used to deliver the same biological dose as compared to protons. Consequently, the number of β^+ emitters and resulting coincidence events is reduced by approximately two orders of magnitude compared to diagnostic PET scans [44]. Furthermore, PET does not measure the dose distribution directly, and interpretation of the signal relies on simulations or reference distributions, typically obtained from Monte Carlo simulations [45]. To enhance reliability, hybrid approaches have been developed that combine PET with other techniques such as prompt gamma [46, 47] or secondary ion tracking [48].

2.3.2 Prompt Gamma Imaging (PGI)

Prompt gamma monitoring is another in-vivo technique developed to verify ion beam range during treatment. When high-energy carbon ions interact with atomic nuclei in tissue, excited nuclear states are produced. These nuclei de-excite rapidly, within less than $\sim 10^{-16}$ s, emitting high-energy prompt gamma rays. Since prompt gamma production occurs along the beam path and correlates well with the primary ion range, it enables real-time treatment verification without biological washout effects [49].

A wide variety of detection technologies have been proposed to utilize prompt gammas using collimated and uncollimated time-based techniques such as prompt gamma timing (PGT) [50] and prompt gamma peak integral (PGPI) [51], which exploit the time-of-flight of gamma photons.

Prompt gamma monitoring offers several advantages over PET. It provides real-time feedback, with no delay due to radioactive decay, and is not affected by biological washout. Moreover, the prompt gamma emission profile exhibits a stronger correlation with the distal dose falloff than the β^+ emitter distribution used in PET [43]. Additionally, the energy spectrum of the emitted gammas can yield compositional information about the irradiated tissue [52].

Despite these advantages, the technique still faces important technical challenges. The high energy of prompt gammas (up to several MeV) requires thick and radiation-resistant collimators and fast, sensitive detection systems. Background radiation, especially from neutrons and scattered photons, significantly affects the signal-to-noise ratio. Moreover, the efficiency of gamma detection is limited due to Compton scattering and the need for heavy shielding [53]. Although the count rate of prompt gamma photons can be 10 to 80 times higher than for PET signals, high-performance electronics are essential to manage the high data throughput and to enable accurate spatial reconstruction.

Prompt gamma imaging (PGI) has been widely explored for proton therapy, and several Monte Carlo studies have demonstrated its feasibility for carbon-ion beams. Simulations using knife-edge slit cameras predicted accurate range verification at clinical energies [54]. These findings were recently validated experimentally with a prototype camera that measured prompt gamma profiles from carbon-ion irradiation of a plastic phantom, achieving a spatial resolution of approximately $\sim$ 4mm, closely matching simulation results [55].

2.3.3 Fragment Tracking

Fragment tracking is a promising method for in-vivo range verification in carbon-ion therapy. It relies on detecting charged nuclear fragments emitted when carbon ions undergo inelastic nuclear interactions in tissue (see Section 2.1.2). These secondary particles, having sufficient energy, can exit the patient and be externally detected. Since such fragmentation is unique to ions heavier than hydrogen, this technique is specific to carbon and heavier beams [16].

Compared to other modalities like prompt gamma imaging, fragment tracking offers a favorable signal-to-noise ratio, as the measured signal arises directly from therapeutic interactions. However, spatial resolution is limited by multiple Coulomb scattering (MCS), especially along the beam axis, and the fragment yield decreases rapidly with detection angle [14].

Fragmentation vertices are reconstructed using tracking detectors with at least two sensitive layers. A particle crossing both layers enables the reconstruction of its path, which is extrapolated backward to estimate the origin point. Accumulating many such tracks yields a vertex distribution that has been shown to correlate with the Bragg peak position [13, 56]. Changes in this distribution between treatment fractions can reflect anatomical changes [18].

To ensure accurate vertex reconstruction, detectors must achieve high spatial resolution

and detect individual particles. Tree technologies have been evaluated: scintillating fiber-based trackers, CMOS pixel detectors, and hybrid pixel semiconductor detectors.

Scintillating Fiber Detectors One established method for detecting charged fragments is the use of multi-layer trackers composed of scintillating fibers. A system consisting of six planes—each comprising two orthogonal layers of scintillating fibers—was developed, followed by a plastic scintillator and a calorimeter for additional event selection and characterization [57]. The scintillating fibers emit light upon particle traversal, which is guided via total internal reflection to photodetectors. Initial clinical trials with this detection system have been initiated [58, 59].

CMOS Pixel Detectors A recent study explored the use of CMOS (complementary metal–oxide–semiconductor) pixel sensors for four-dimensional (4D) online monitoring in carbon-ion therapy, specifically targeting density changes induced by respiratory motion in lung cancer patients. The experimental setup included 12 MIMOSA-28 (Minimum Ionizing MOS Active Pixel Sensor) sensors arranged in four separate trackers, each consisting of three stacked sensors. Each MIMOSA-28 sensor had an active area of approximately 2×2 cm^2, composed of 928×960 pixels with dimensions of 20.7 μm $\times$ 20.7 μm. The total sensor thickness was 50 μm, including a 14 μm epitaxial layer. The system operated at a frame rate of approximately 5 kHz with an integration time of 186.5 μs. In experimental evaluations at the Marburg Ion-Beam Therapy Center, this setup successfully detected range overshoots due to sharp density transitions, achieving reliability rates of $83.0 \pm 1.5\%$ and $92.0 \pm 1.5\%$, depending on the analyzed volume and iso-energy layers [60].

Semiconducting Pixel Detectors Our group has investigated the use of hybrid pixel semiconductor detectors, based on Timepix technology, for multiple applications including LET measurement, helium ion radiography, and carbon-ion therapy (CIRT) monitoring. In the latter case, the monitoring system is based on two parallel layers of hybrid pixel detectors with high spatial and temporal resolution.

When a charged fragment traverses both layers, its trajectory is reconstructed and extrapolated back to estimate the fragmentation vertex [13]. Millimeter vertex localization has been demonstrated [20]. The compact form factor, high granularity, and robustness of Timepix-based detectors make them well-suited for clinical use. Their performance in beamline conditions has also been validated, confirming their feasibility for CIRT monitoring [19]. An in-depth description of the physics behind semiconductor detectors is presented below.

2.4 Detection Principles Underlying the Clinical Monitoring System

Although the clinical system setup is presented in detail in the Materials and Methods section (Section 3.1.2), this section focuses on the fundamental detection principles behind the hybrid silicon pixel detectors (Timepix3) employed for clinical monitoring.

2.4.1 Semiconductor Detectors

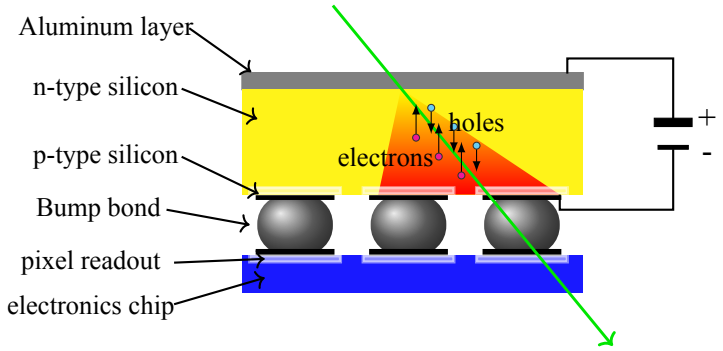

Figure 2.3. Sketch of the Timepix3 hybrid pixel detector layout (not to scale). The yellow region indicates the silicon sensor chip, including the high-resistivity n-type and p-type layers. The top gray layer corresponds to the aluminum backside contact. A green arrow emulates the trajectory of an incoming charged particle. Electrons and holes are represented by magenta and green dots within the silicon sensor, along with arrows indicating their respective drift directions. The diagram also shows the bump bonds, the pixelated readout layer, and the Timepix3 electronics chip.

Semiconductor detectors operate based on p-n junction technology. A p-n junction is created by combining p-doped and n-doped regions in a silicon substrate. P-doping introduces atoms with fewer valence electrons, forming mobile positive charge carriers (holes), while n-doping introduces atoms with excess electrons. Their junction forms a depletion zone, free of mobile charge carriers, across which an electric field is established.

Applying an external reverse-bias voltage widens the depletion zone and strengthens the electric field, improving the detector's sensitivity to ionizing radiation [61]. When a charged particle traverses the depletion region, it deposits energy and creates electron-hole pairs. These carriers are driven by the electric field: electrons toward the anode, holes toward the cathode. Their motion produces a measurable current, forming the basis of the detection signal. Position sensitivity is achieved by segmenting the sensor into individual pixels.

In hybrid detectors like Timepix3, the sensor and readout electronics are fabricated separately and connected via bump bonds [62]. Each pixel in the sensor is paired with a readout circuit, allowing independent signal acquisition from each pixel. The bump bonds provide both mechanical and electrical connectivity between the two layers.

The Timepix3 chip enables simultaneous measurement of the time of arrival (ToA) and time over threshold (ToT) for each pixel. ToA records when the signal crosses a defined threshold, while ToT correlates with the charge collected, and thus the energy deposited. This dual readout allows for both time-resolved and energy-resolved event reconstruction.

When a particle deposits energy in the silicon sensor, it creates a charge cloud that can spread across multiple neighboring pixels before reaching the electrodes. This may result in clusters of adjacent pixels registering partial signals. Only pixels collecting a signal above a set threshold are read out. At low bias voltages or low energy deposits, some charge may be lost below the threshold, leading to underestimation of energy or merged signals from nearby particles.

Another important effect is time walk, signals of higher amplitude rise faster and thus cross the threshold earlier than lower-amplitude signals. This causes timing distortions depending on the deposited energy. The combined ToA and ToT information enables post-processing corrections for time walk.

2.5 Monte Carlo Simulation

In the context of this thesis, we develop a Monte Carlo-based simulation framework for in-vivo CIRT monitoring via the detection of secondary nuclear fragments, to support the analysis and interpretation of measured signals.

The Monte Carlo method provides numerical solutions to complex problems by simulating the random evolution of individual components interacting according to known physical laws. In radiation transport, this involves tracking particles as they undergo random interactions, based on cross sections, within a defined geometry [63]. By mimicking these microscopic events many times, macroscopic quantities such as dose or energy deposition can be estimated. The strength of the method lies in its simplicity: a complex system is modeled through repeated sampling of its elementary processes.

2.5.1 Phase Space Description and the Boltzmann Equation

Monte Carlo simulations model particle transport by tracking individual particles as they move and interact within a medium. Each particle's state is represented in a multidimensional *phase space*, encompassing its spatial coordinates $\mathbf{x}$, momentum $\mathbf{p}$, time t, and intrinsic properties such as particle type or spin, collectively denoted by α [64].

The distribution of particles in phase space is described by the probability density function $f(\mathbf{x}, \mathbf{p}, \alpha, t)$. The infinitesimal number of particles dN in a differential phase space volume is given by:

$$dN = f(\mathbf{x}, \mathbf{p}, \alpha, t)\, d^3x\, d^3p\, dn_\alpha \tag{2.5}$$

The temporal evolution of f is governed by the *Boltzmann transport equation*, which, in its general form, is expressed as:

$$\frac{\partial f}{\partial t} + \mathbf{v} \cdot \nabla_{\mathbf{x}} f + \mathbf{F} \cdot \nabla_{\mathbf{p}} f = \left(\frac{\partial f}{\partial t}\right)_{\text{coll}} \tag{2.6}$$

Here, $\mathbf{v}$ is the particle velocity, $\mathbf{F}$ represents external forces, and the term on the right-hand side accounts for changes in f due to collisions and interactions [65].

Solving the Boltzmann equation analytically is often infeasible for complex systems. Therefore, Monte Carlo methods are employed to simulate particle trajectories and interactions stochastically, sampling from relevant probability distributions to approximate the behavior dictated by the Boltzmann equation [64].

2.5.2 Sampling Techniques

Sampling is integral to Monte Carlo simulations, enabling the generation of random variables that model physical processes. Common sampling methods include:

- **Inverse Transform Sampling**: Utilizes the inverse of the cumulative distribution function (CDF) to transform uniformly distributed random numbers into samples from the desired distribution.
- **Rejection Sampling**: Generates candidate samples from an easy-to-sample distribution and accepts them based on a criterion related to the target distribution.
- **Alias Method**: Efficiently samples from discrete probability distributions by preprocessing the distribution into a table that allows constant-time sampling.

The choice of sampling technique depends on the specific distribution and computational considerations [66].

2.5.3 Pseudo-Random Numbers and Reproducibility

Monte Carlo simulations rely on pseudo-random number generators (PRNGs) to produce sequences of numbers that approximate the properties of random sequences. These sequences are determined by an initial *seed* value. Using the same seed ensures reproducibility of simulation results, which is crucial for debugging and verification purposes [67].

2.5.4 Variance Reduction Techniques

Although Monte Carlo simulations are highly accurate, they often require substantial computational time due to their statistical nature. This can be particularly limiting when simulating rare events, deep penetration problems, or regions with low particle flux. To address this, various *variance reduction techniques* (VRTs) have been developed with the goal of decreasing the statistical uncertainty of the results without proportionally increasing the number of simulated particle histories. The overall simulation efficiency is often quantified by the figure of merit (FOM), defined as $\text{FOM} = 1/(\sigma^2 T)$, where σ^2 is the variance of the scored quantity and T is the computational time [64].

Variance reduction techniques aim to improve this efficiency by focusing computational effort on the most statistically relevant parts of the problem. For example, *splitting* and *Russian roulette* are complementary methods that modify the number of particles based on their importance: particles entering high-relevance regions may be split into multiple lower-weight particles, whereas particles in low-relevance regions may be terminated with adjusted probability [68]. Another widely used method is *importance sampling*, in which particle histories are biased to occur more frequently in regions or for processes that contribute significantly to the quantity of interest, while preserving the unbiased nature of the simulation through appropriate weight adjustments [64].

In addition, *forced collisions* ensure interactions in designated regions by modifying the sampling of free paths, and *geometry-based biasing* can enhance particle transport toward

detectors or scoring volumes. More advanced schemes such as *weight windows* dynamically control particle weights across space to maintain statistical balance and efficiency [69].

Particle Transport and Tallies

In Monte Carlo simulations, particle transport refers to the step-by-step modeling of each particle as it travels through a medium, undergoing physical interactions governed by known cross sections. The process begins with the generation of a primary particle, whose path is propagated until a stopping condition is met, typically when its kinetic energy falls below a user-defined threshold, when it exits the geometry, or when it is absorbed.

At each step, the free path length to the next interaction site is sampled from an exponential distribution based on the material's macroscopic cross section. The type of interaction—such as elastic scattering, inelastic nuclear interaction, or ionization—is sampled from the cumulative probability distribution constructed from the respective partial cross sections. If secondary particles are produced during the interaction, they are added to a particle stack for subsequent transport. This iterative procedure continues until all particles in the stack have been processed [64].

Throughout the simulation, physical quantities of interest are accumulated using *tallies*. Tallies are scoring mechanisms that record information such as energy deposition, particle fluence, dose, or secondary particle production. They may be defined over spatial cells, energy bins, or angular intervals. Tallies can be configured to record integrated quantities (e.g., total dose in a voxel) or differential quantities (e.g., energy spectra or angular distributions).

2.5.5 Transport of Charged Particles

In Monte Carlo simulations, the transport of charged particles such as protons and heavy ions requires an accurate modeling of both electromagnetic and nuclear interactions. Electromagnetic processes include energy loss through ionization and elastic scattering in the Coulomb field of nuclei, both of which are typically handled via a condensed history approach in which multiple small steps are aggregated into a single effective transport step. Ionization energy loss is often implemented as a continuous process along each step, governed by the Bethe-Bloch equation with corrections for density effects and atomic shell structure. For protons, specific models are used above and below 2 MeV to account for the increasing relevance of shell corrections at lower energies. Heavy ions like helium and carbon are modeled similarly but require higher stopping power and fragmentation cross sections due to their mass and charge.

Besides continuous processes, charged particles may undergo discrete events such as the emission of δ-electrons or nuclear interactions. The latter are particularly relevant in heavy-ion therapy, where inelastic collisions between primary ions and tissue nuclei result in nuclear fragmentation. This leads to the production of lighter secondary particles such as protons, neutrons, alpha particles, and residual nuclei, many of which contribute to the overall dose distribution. The fragmentation process also introduces a "tail" of dose deposition beyond the Bragg peak, which is especially pronounced in carbon-ion therapy. Therefore, to simulate treatment fields accurately, Monte Carlo codes must incorporate reliable mod-

els of both the primary particle stopping and the generation, transport, and interaction of secondaries.

Different transport models are applied depending on the projectile type and energy. For example, in the Geant4 toolkit, electromagnetic interactions are handled by standard or low-energy electromagnetic physics packages, while nuclear interactions rely on intranuclear cascade models such as the Binary Cascade, Bertini, or INCL++ depending on the energy range. The outcome of these interactions includes excited residual nuclei which are handled through de-excitation and radioactive decay modules, simulating delayed processes like gamma emission or beta decay based on evaluated nuclear data libraries.

All these transport mechanisms play a crucial role in determining the final dose distribution and radiation field, particularly in therapeutic applications. Their implementation in Monte Carlo codes must balance physical accuracy with computational efficiency, often requiring carefully tuned transport thresholds and physics lists.

Chapter 3

Materials and Methods

3.1 Description of the In-Vivo Detection System

Timepix semiconductor pixelated detectors have demonstrated remarkable capabilities in detecting secondary fragments for carbon ion radiotherapy (CIRT) monitoring [18]. Over the past decade, our research group has made significant advancements in this field, culminating in the development of a clinical monitoring system tailored for in-vivo fragment tracking in patients undergoing carbon ion therapy [20]. This system was specifically designed for integration into the clinical workflow of the horizontal beamline H2 at the Heidelberg Ion Therapy Center (HIT), where the InViMo clinical trial is currently being conducted.

3.1.1 The Heidelberg Ion-Beam Therapy Center (HIT)

The Heidelberg Ion-Beam Therapy Center (HIT) is equipped with a synchrotron for ion acceleration and treatment delivery. The facility offers treatments with protons (^{1}H), carbon ions (^{12}C), and helium ions (^{4}He) for clinical applications, while oxygen ions (^{16}O) are available for research purposes. The generation of therapeutic ion beams follows a two-step acceleration process. First, ions are extracted from an ion source (1 in Figure 3.1) and pre-accelerated in a linear accelerator (2). In the second stage, they enter the synchrotron (3), where they are further accelerated to their final treatment energies and then directed to the treatment rooms by steering magnets (4).

The HIT facility has three treatment rooms: two horizontal beamline treatment rooms (H1 and H2) (6 and 5 in Figure 3.1) and a gantry treatment room (7). The gantry, a 670-ton rotating structure, allows flexible beam delivery at different angles. In addition, an experimental room (9) is dedicated to research. The CIRT monitoring clinical trial (InViMo) is being conducted in H2, see Figure 3.3. The clinical trial workflow is described in detail later in the subsection 3.2.4.

For CIRT, at the HIT facility provides carbon ion beams with energies ranging from 88.83 to 430.10 MeV/u, corresponding to ranges in water from 20 mm to 300 mm. Beam energy increments are 1.0 mm for lower energies and 1.5 mm for higher energies to allow precise dose delivery. The full width at half maximum (FWHM) of the carbon ion beam varies between 3.4 mm and 13.4 mm depending on the beam energy [70].

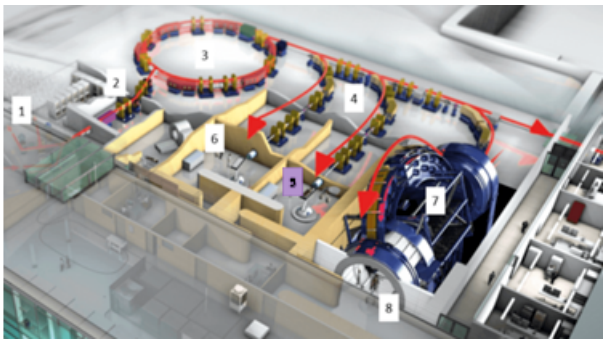

Figure 3.1. Schematic representation of the Heidelberg Ion-Beam Therapy Center (HIT) facility. The image illustrates the main components of the particle acceleration and beam delivery system, including (1) ion sources, (2) the linear accelerator, (3) the synchrotron, (4) the beam transport system, (5,6) the horizontal treatment rooms (H2 and H1), (7) the gantry, (8) the beam nozzle, and (9) the experimental research area. The red arrows indicate the ion beam path from generation to treatment. Adapted from [71].

HIT employs the active intensity-modulated raster-scanning technique [72], which enables precise dose delivery by scanning the tumor volume with narrow ion pencil beams steered by fast dipole magnets. The beam parameters, including focus size, and beam energy, are actively adjusted for each irradiation point, also referred to as a raster point. The raster scanning method can cover a maximum lateral field size at the isocenter of $20\,\text{cm} \times 20\,\text{cm}$ [70]. The tumor volume is virtually divided longitudinally into iso-energetic slices (IES), each corresponding to a specific beam energy level. Within each IES, the pencil beam is magnetically deflected to traverse the planned target volume, delivering the prescribed dose to each voxel. After completing an IES, the beam energy is adjusted to target the next slice, proceeding from the most distal to the proximal regions of the tumor. Additionally, a ripple filter in the beam nozzle broadens the Bragg Peak to homogenise the dose in the spread-out Bragg peak. This reduces the total number of required energy layers and optimizes treatment efficiency [73].

To ensure the accuracy and stability of this dynamic scanning technique, a real-time beam monitoring system is required. The Beam Application and Monitoring System (BAMS), installed within the beam nozzle in the treatment rooms (shown on the right in Figure 3.3), serves as the final checkpoint before treatment delivery. BAMS consists of two Multi-Wire Proportional Chambers (MWPCs) that measure pencil beam positions and three Ionization Chambers (ICs) that track the number of delivered ions. The distance between BAMS and the isocenter is 1.12 cm [74]. During treatment, all beam parameters, including pencil beam positions and ion counts, are recorded in the Beam Record File (BRF) for quality assurance and treatment verification.

3.1.2 Clinical CIRT monitoring system

The system comprises seven AdvaPIX TPX3 Quad modules [75], each a customized version developed by ADVACAM s.r.o. (Prague, Czech Republic). Each module consists of four Timepix3 chips, functioning as a mini-tracker with two detection layers -front and back- separated by 20.3 mm. Each layer incorporates a 300 μm-thick continuous silicon sensor,

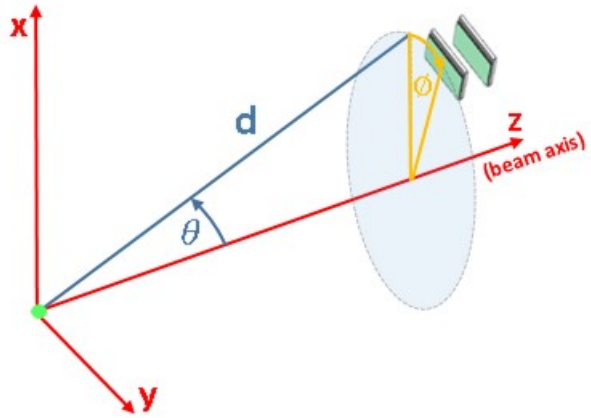

(a) Schematic representation of the mini-tracker positioning relative to the isocenter.

mini-tracker	$d\,[mm]$	$\theta\,[^\circ]$	$\phi\,[^\circ]$
1	16	36	20
2	16	36	-20
3	20	28	45
4	20	28	0
5	20	28	-45
6	24	20	20
7	24	20	-20

(b) Table summarizing the positional parameters of the mini-trackers, including distance (d), polar angle (θ), and azimuthal angle (ϕ).

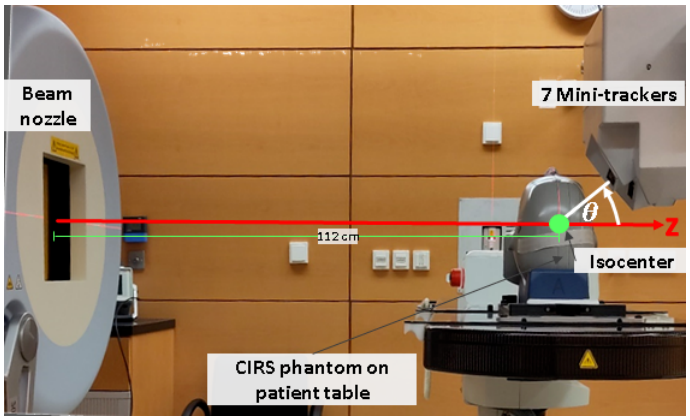

(c) Picture of a lateral view of the clinical monitoring system in the measurement position at HIT treatment room. The polar angle θ is depicted.

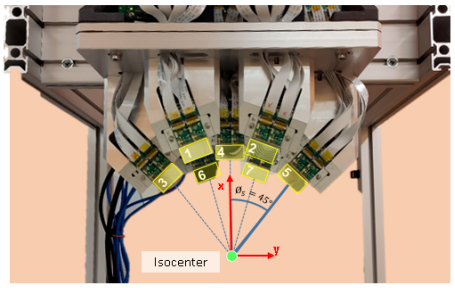

(d) Beam-eye view of the uncovered seven mini-trackers. Yellow rectangles highlight the first sensitive layer of each detector with IDs. Blue lines represent the azimuthal angle ϕ.

Figure 3.2. Mini-tracker positions and clinical monitoring system at HIT treatment room.

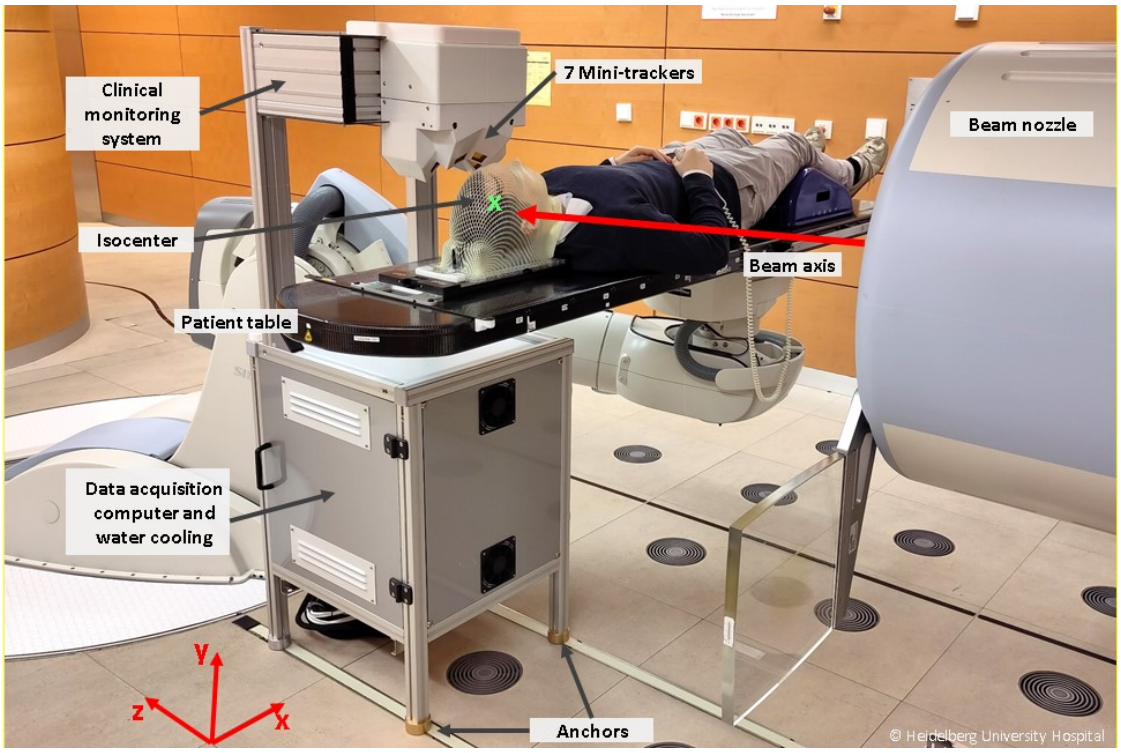

Figure 3.3. Photograph of the clinical detection system for CIRT monitoring in the measurement position at the horizontal treatment room (H1) at the Heidelberg Ion-Beam Therapy Center (HIT). An actor patient is immobilized on the treatment table using a thermoplastic mask to ensure precise positioning. The isocenter is marked (green cross). To ensure position reproducibility of the setup during measurements, the system is securely anchored to the concrete floor of the H2 treatment room, where the actual measurements take place. The coordinate system (bottom left) defines the spatial orientation within the treatment room.

covering an active detection area of 18×14 mm^2, with a 512×256 pixel matrix and a pixel pitch of 55 μm. The detectors feature a time resolution of 1.56 ns, enabling precise tracking of secondary ions using coincidence.

The seven mini-trackers are arranged symmetrically around the beam axis. The schematic in Figure 3.2a illustrates the spatial parameters defining the mini-tracker positions in relation to the beam axis and the room isocenter, which is depicted in light green. The positioning decision was based on previous studies [14], ensuring a balance between the fluence rate and the modules' angles. The distance (d) spans from 16 cm to 24 cm, the polar angles (θ) range from 20° to 36°, and the azimuthal angles (ϕ) vary from -45° to 45°, ensuring effective fragment detection. The positional parameters of each detector are listed in Table 3.2b.

The proximity of the detectors to the patient's head can be observed in Figure 3.2c, which presents a lateral view of the detector system within the treatment room. In this setup, the CIRS head phantom [76] serves as a patient surrogate, and the room isocenter along with the azimuthal angles (ϕ) are depicted. A beam-eye view of the detector system without the white cover, shown in Figure 3.2d, reveals the seven mini-tracker front sensitive layers along with their respective IDs. In this view, the polar angles (θ) are also represented.

Photograph of the clinical detection system for CIRT monitoring in the measurement

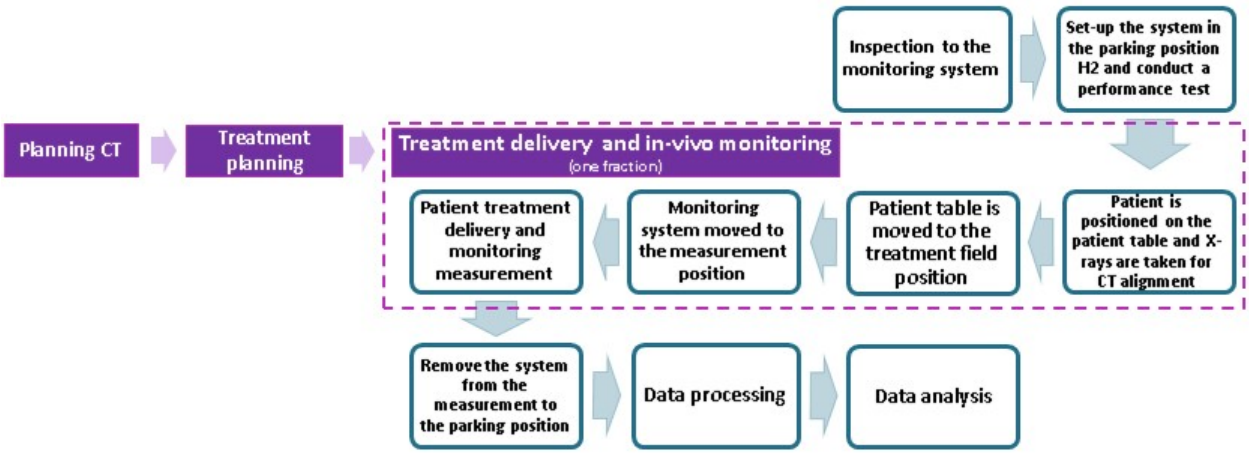

Figure 3.4. CIRT monitoring workflow at HIT.

position is depicted in Figure 3.3. The box located under the patient table houses the water cooling system and data acquisition computer. The system requires only two cables for operation: a power cable and an Ethernet cable, allowing for remote control of the detector from outside the treatment room during measurements. The system is transportable and designed to minimize interference with the clinical workflow. It is reproducibly positioned using floor-embedded anchors to the H2 treatment room at HIT, ensuring sub-millimeter precision during repeated measurements [20].

3.1.3 CIRT monitoring workflow at HIT and data processing and analysis

The integration of in-vivo monitoring into the clinical workflow was designed to minimize interference with standard radiotherapy (RT) procedures while ensuring consistent treatment monitoring. The standard CIRT clinical workflow (shown in purple in Figure 3.4) consists of a planning CT, followed by treatment planning, and subsequently, the delivery of the prescribed treatment dose per fraction.

The in-vivo monitoring workflow (depicted in blue in Figure 3.4) is partially embedded within the treatment delivery phase. Before monitoring a CIRT fraction, an inspection of the system is performed, followed by the setup of the system in the treatment room H2, along with a performance test to ensure proper operation. Once the patient is positioned on the treatment table, orthogonal X-rays are acquired to verify alignment.

The patient table is then moved along the treatment fields as treatment delivery occurs. Since only one field per patient is monitored, once the table is positioned at the monitored treatment field, the clinical monitoring system is moved to the measurement position (as shown in Figure 3.3), where it remains throughout the treatment field delivery and in-vivo monitoring measurement. After the measurement, the system is returned to its parking position, and the delivery of any remaining treatment fields, if applicable, continues. The acquired data is then processed and analyzed.

The processing of the acquired data is performed using an in-house developed data analysis framework written in MATLAB (MATLAB version 2021b or 2024b). The data

processing pipeline begins with cluster formation, where signals from neighboring pixels of each Timepix3 detector (including lateral and diagonal neighbors) are grouped. A cluster is defined as a group of pixels where the maximum timestamp difference between its constituent pixels does not exceed 500 ns. The cluster timestamp is assigned based on the earliest recorded timestamp within the cluster.

To estimate the particle impact position in the mini-tracker's sensitive layer, the energy-weighted centroid of the pixel coordinates within the cluster is calculated. After identifying clusters, those detected in the two sensitive layers of the mini-tracker must be matched to reconstruct fragment tracks. Coincidence is established if the timestamp difference between clusters in both layers is within 75 ns, allowing for synchronization and timestamp errors. If multiple clusters exist within this coincidence window, the pair with the smallest time difference is assigned to the same fragment track [19].

To reconstruct fragment trajectories within the treatment room, they are transformed into the room coordinate system, utilizing the known position of the corresponding mini-tracker. The estimated fragment creation vertex is defined as the midpoint of the shortest connecting line between the measured fragment trajectory and the pencil beam axis [14].

Data analysis in in-vivo monitoring for CIRT is an evolving field, with various methodologies under investigation to enhance the detection and localization of inter-fractional anatomical changes. In the InViMo clinical trial, typically two to six treatment fractions per patient are monitored, and data from different monitored fractions are intercompared to detect anatomical variations. The reconstructed FV distributions from two separate treatment fractions are analyzed in 3D using two primary methods. First, the absolute difference in the number of measured fragments is computed to assess variations in fragment distribution. Second, the Kolmogorov-Smirnov (KS) statistical test is applied to determine whether the distributions of detected fragments originate from the same probability distribution. The KS test evaluates the maximum difference between normalized cumulative histograms and converts this result into a p-value, providing a statistical basis for identifying significant changes in fragment distributions.

3.2 FLUKA Monte Carlo Simulation

The primary objective of this PhD project was to develop a Monte Carlo (MC) simulation framework for monitoring carbon ion radiotherapy (CIRT) by detecting charged nuclear fragments using the clinical monitoring system described above. To achieve this, we employed FLUKA [77, 78], a well-established Monte Carlo simulation package extensively used and validated in particle therapy applications [79].

The HADROTHE package, with default settings tailored for ion therapy which includes the state-of-the-art physics models, was used. The particle transport thresholds is set at 100 keV, except for low-energy neutrons, which are transported down to 10^{-5} eV. Atomic physics models handle continuous energy loss, energy loss straggling, delta-ray production (production cut at 100 keV), and the multiple Coulomb scattering of charged particles. The nuclear interaction models for hadrons, photons, muons, and neutrinos are described using the PEANUT model [80]. For ions down to 0.1 GeV/n, FLUKA implements a modified

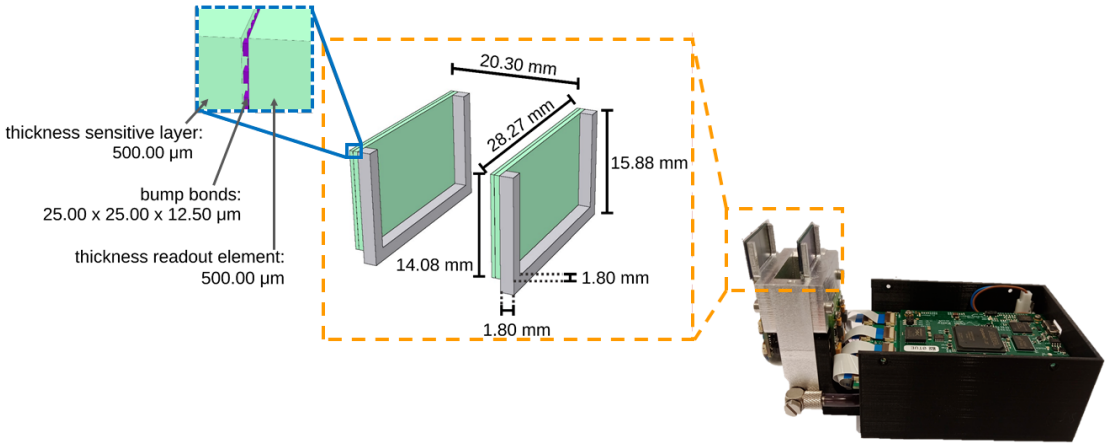

Figure 3.5. Implementation of the mini-tracker in the FLUKA Monte Carlo (MC) simulation. The bottom part of the image shows a photograph of the mini-tracker, while the upper section illustrates the sensitive region implemented in the FLUKA MC simulation (highlighted by the orange dashed box). This region includes the silicon sensitive layer, bump bonds, the readout element, and the U-shaped aluminum bars. The inset (blue dashed box) provides a zoomed-in view of the bump bonds and detector layers. Adapted from [22].

version of the relativistic quantum molecular dynamics model (RQMD-2.4) [81]. Below 150 MeV/n, nuclear reactions are handled using the Boltzmann master equation (BME) model [82], with a smooth transition between models in the overlapping energy range.

3.2.1 Implementation of the mini-tracker in FLUKA

As a first step in building the simulation framework for CIRT monitoring, the implementation of a mini-tracker (AdvaPIX TPX3 Quad module) within FLUKA was performed, including the experimental validation of secondary fragment tracking, published in [22]. For this implementation, FLUKA version 2021.2.5 was used to model the custom mini-tracker module used in the clinical detection system. The geometry included the key components within the sensitive region of the mini-tracker, as shown in Figure 3.5 (orange dashed box), including the silicon sensitive layers, the bump bonds connecting the layers to the readout chip, and the aluminum support bars that support the sensitive parts of the mini-tracker. Both the sensitive layer and the readout chip were implemented as solid silicon plates, each with a thickness of $500\ \mu$m. The bump bonds connecting the readout chip were modeled as 256×512 cuboids, each with a size of $25\ \mu$m (see Figure 3.5, blue dashed box). The material composition of the bump bonds was set to a mixture of 63% tin and 37% lead, which closely resembles the actual materials. Additionally, the U-shaped metal bars were modeled as aluminum.

Two adapted Fortran subroutines were incorporated into the FLUKA simulation. The first, *source.f*, was activated via the SOURCE card to define the particle source, delivering the entire clinical treatment plans through the simulation of multiple raster points. This included specific beam parameters such as focus size (FWHM), number of primary ions, beam energy, and beam position. The second, *mgdraw.f*, was activated via the USERDUMP

card to identify charged particles passing through the mini-tracker based on a predefined detection criterion: the particle must deposit energy above the detection threshold in both sensitive layers of the mini-tracker. In the clinical detection system, this detection threshold per pixel was set at 3 keV. When this criterion was met, several particle attributes were recorded, including: spatial entry coordinates, particle type, kinetic energy, energy loss in both sensitive layers, and the Cartesian coordinates of primary carbon-ion fragmentation (scored as true FV), among others [22].

For the experimental validation of mini-tracker geometry and the scoring mechanism into the FLUKA [22], the detected fragments within the mini-tracker were studied for 10 different pencil-beam energies within the therapeutic range (160, MeV/n to 255, MeV/n) impacting a homogeneous head-sized PMMA phantom. The performance of the mini-tracker was evaluated by comparing the simulation results with experimental data acquired at the HIT. Several aspects of the performance of the mini-tracker within FLUKA were investigated, including the angular distribution of the detected fragment tracks, the reconstructed fragment emission profiles represented by histograms along the beam axis indicating the number of reconstructed fragments, and the number of detected fragments as a function of the detector position, ranging from 0° to 40°. This includes the positioning angles of the detectors in the clinical detection system. Furthermore, our investigation showed a robust agreement between experimental and simulated data, confirming the effective integration of the mini-tracker and the scoring mechanism within our FLUKA simulation.

3.2.2 FLUKA MC-based clinical CIRT monitoring system

The clinical monitoring system was modeled by incorporating the geometry and scoring of seven 300 μm silicon thickness mini-tracker modules, which constitute the clinical detection system, into the MC simulation. These detectors were positioned according to the configuration listed in Figure 3.2. This extended implementation was integrated into the FLUKA-based MC framework FICTION (FLUKA Integrated Framework for CT-based calculations in Ion Therapy) [23,24], developed at HIT. This integration enables the simulation of CIRT monitoring for patients treated at HIT. The integration process required adding, extending, or modifying specific components within the FICTION. Figure 3.6 illustrates the general FICTION workflow, with our custom implementations highlighted in magenta.

As an overview, FICTION converts DICOM CT data into a FLUKA voxel format and DICOM RT data into a readable format for the SOURCE definition. The HU-based look-up tables, generated as described in [83,84] for protons in FLUKA and later extended for carbon ions, ensure a sub-millimeter agreement between FLUKA MC and the TPS in homogeneous materials with varying HU values. The geometry and material definitions of beamline elements, such as the ripple filter [85], are also incorporated. During code execution, the beamline elements are rotated to the defined treatment angle around the isocenter, while the voxelized CT geometry remains fixed in the MC coordinate system. Consequently, all necessary transformations are applied to the beamline elements.

After compiling the FLUKA custom executable, input files and scripts for parallel execution are generated, allowing simulations to be performed at the Scientific Computing Unit of the HIT facility. As part of our implementation into FICTION, specific physics settings were

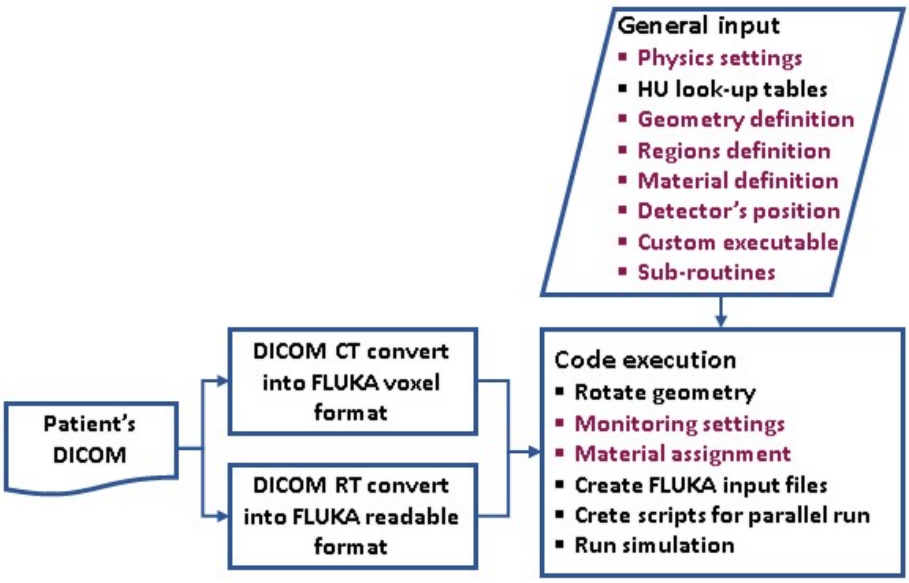

Figure 3.6. Simplified schematic representation of the FLUKA-based MC framework FICTION (FLUKA Integrated Framework for CT-based calculations in Ion Therapy), with our custom implementations highlighted in magenta.

modified to enhance the precision of light fragment generation—such as protons and alpha particles, which are critical for accurately simulating secondary fragment production [80]. To achieve this, the evaporation and coalescence models [86] were activated. Additionally, to optimize computational time efficiency, delta-ray production was deactivated, and an energy threshold of 20 MeV was set for low-energy neutron interactions. Since low-energy neutrons primarily deposit energy locally in tissue, their impact on the detection of charged nuclear fragments escaping from the irradiated patient is negligible [22]. The geometry, region, material definitions, and material assignments were extended to include the tracker modules, incorporating their positions into the FLUKA-MC pipeline, as described in Figure 3.6.

In addition to the values scored by the mgdraw.f subroutine (reconstructed and true fragment vertices, etc.) and the dose, we also activated the USRBIN FLUKA card to score the Heavy Ion Nuclear Interaction (HINI). This includes all hadronic inelastic and non-elastic interactions that encompass potential nuclear interactions along the carbon-ion beam path within the tissue.

3.2.3 In-table CIRT monitoring prototype

The clinical monitoring system was designed and tailored to monitor head and neck cancer patients as part of the prospective clinical trial at HIT. However, other pathologies treated with CIRT, such as pelvic tumors (e.g., prostate cancer), could also benefit from this monitoring approach. In these cases, bone-soft tissue interfaces and rectum-intestine filling and emptying introduce range uncertainties, affecting treatment accuracy.

To address these challenges, an in-table monitoring system was developed using seven tracking modules. The modules were positioned to ensure effective fragment detection while fitting within the hollow section of the treatment table. The treatment table (couch) used

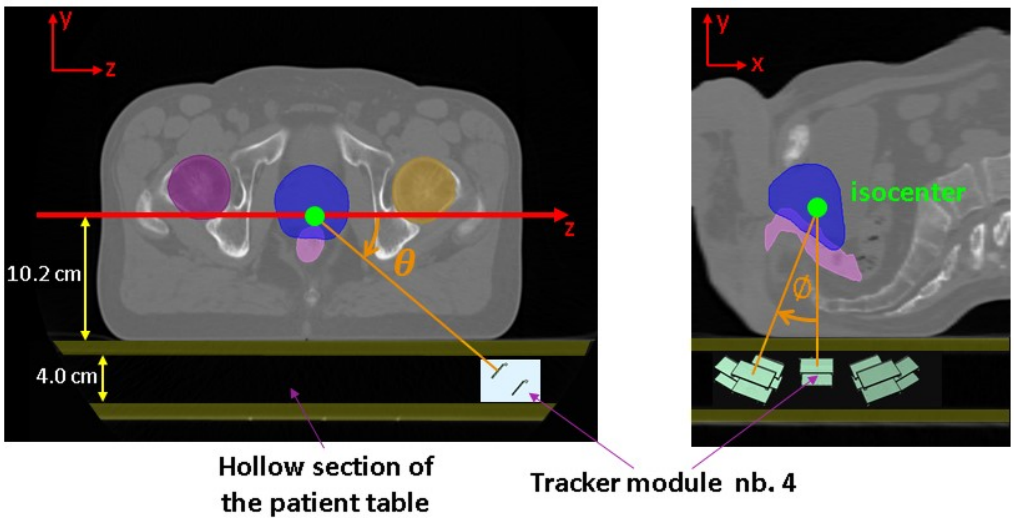

Figure 3.7. Tracker modules positions for the in-table prototype of a future monitoring system. Left: axial CT view of the prostate patient showing polar angle θ, mini-tracker nb. 4, and distances from the isocenter (neon green) to the table surface and the hollow section. Right: sagittal CT view with the seven mini-trackers inside the hollow table section and the azimuthal angles ϕ depicted.

in CIRT is radiotransparent, constructed from low-density materials such as carbon fiber, allowing minimal interference with the particle beam.

Figure 3.7 illustrates the axial (left) and sagittal (right) CT slices of a prostate cancer patient lying on the treatment table. For better visualization, the yellow shadow highlights the rigid material of the table and also delineates the 4 cm-high hollow gap within it. The left image depicts the main contours of a prostate cancer patient, including the PTV (blue), rectum (pink), and femoral heads (magenta and mustard). Additionally, mini-tracker nb. 4 is marked with a white box for better visualization.

The positioning of the trackers in the FLUKA MC simulation follows the same methodology as in the clinical monitoring system, shown in Figure 3.2a, where the detectors are positioned relative to a reference point in the treatment room with their corresponding polar angle (θ) and azimuthal angle (ϕ). In Figure 3.7, this reference point is represented in green, located 10.2 cm from the table surface. In this case, the reference point corresponds to the patient's isocenter location. The right image in Figure 3.7 shows the seven mini-trackers positioned inside the treatment table, along with the depiction of the polar angle. Table 3.1 summarizes the positional parameters used in the simulation of the mini-trackers inside the hollow gap of the treatment table. The attenuation of detected fragments by the patient table has not yet been quantified. In the prostate CIRT monitored patient presented in Section 4.3, the treatment table was not included in the simulation since the thickness of the CT table differs from that of the patient table in the H2 treatment room at HIT.

The in-table approach was conducted as an exploratory study to evaluate the performance of CIRT monitoring for tumor sites beyond the head and neck region. Technical aspects, such as cabling, cooling, and system integration, were not considered in this initial exploration, as they fall outside the scope of the simulation framework defined in this thesis. Additionally, further evaluations, such as the impact of table attenuation on detected

mini-tracker	$d\,[mm]$	$\theta\,[^\circ]$	$\phi\,[^\circ]$
1	20.5	-40	20
2	19.0	-40	-20
3	20.5	-40	45
4	21.0	-44	0
5	21.0	-44	-45
6	18.0	-48	20
7	18.0	-48	-20

Table 3.1. Table summarizing the positional parameters of the mini-trackers inside the hollow gap of the treatment table. The first column lists the mini-tracker ID, the second column shows the distance between the isocenter and the front layer of the mini-tracker module, and the third and fourth columns provide the polar angle (θ) and azimuthal angle (ϕ), respectively.

fragments, still need to be conducted.

In an ideal scenario, the in-table system for CIRT monitoring would be adjustable and mobile, allowing it to translate within the hollow region of the treatment table to align precisely with the patient's isocenter. This mobility would ensure that the system does not interfere with coplanar X-ray imaging, which is taken during the first step of treatment delivery (see Figure 3.4) to verify patient alignment with CT scans. Another potential implementation could involve a modular system that can be inserted into the treatment table specifically for monitoring measurements in horizontal beamline treatments like H2 at HIT.

3.2.4 Simulation CIRT monitoring workflow

For patient-specific simulations, CT and treatment planning (RT DICOM) data are required. To prevent geometric overlap in FLUKA caused by the proximity of the clinical monitoring system to the patient's head, the CT is cropped accordingly. In our MC-based CIRT monitoring methodology (detailed in Section 3.2.2), a dedicated patient folder is created for each treatment field to be simulated. Since one treatment field from the RT dataset is simulated per run, the field must be selected based on the specific aim of the simulation. Within the patient folder, the executable file is configured, defining parameters such as the treatment field name, cropped CT, RT dataset, and the number of processing cores. Once configured, this folder is transferred to the Scientific Computing Unit at HIT, where our FLUKA MC-based simulation of CIRT monitoring methodology is executed.

Following multicore execution, the per-core outputs are merged to generate the reconstructed FV, true FV, dose distribution, and Heavy Ion Nuclear Interaction (HINI) data. To ensure successful simulation execution, checkpoints were implemented during data processing. Once the simulation is complete, data analysis is performed. The steps described above will henceforth be referred to in this document as the CT-based *CIRT monitoring simulation workflow*.

In the scope of this thesis, to study inter-fractional anatomical changes, two simulations were conducted per patient. The first simulation utilized the planning CT, providing a baseline for the monitored treatment. In the second simulation, a subsequent follow-up CT was used. For both simulations, the initial treatment plan was simulated.

Table 3.2. Summary of treatment parameters for each simulated patient. The table includes the patient ID, where the prefix S denotes simulated patients (retrospective) and M represents measured patients monitored in the InViMo clinical trial. It lists the treatment plan fields, with simulated fields in bold, along with the number of ion energy steps (IES), the range of pencil beam (PB) energies, the number of days between the planning CT and follow-up CT, and the type of tumor treated.

Patient ID	Treatment fields (°)	No. of IES	PB energies (MeV/n)	Days between CTs	Type of tumor
S-1	**5**, 315, 265	72	[88.83 - 247.74]	12	mucosal melanoma
S-2	5, 313, 225, **175**	72	[88.83 - 247.74]	15	adenoid cystic carcinoma
S-3	**175**, 225, 280	74	[118.52 - 268.32]	46	adenoid cystic carcinoma
S-4	**175**, 240, 290	68	[88.83 - 239.45]	12	adenoid cystic carcinoma
S-5	**0**, 315, 265	64	[122.36 - 253.55]	14	squamous cell carcinoma
M-6	**175**, 215	45	[118.52 - 218.52]	27	adenoid cystic carcinoma
M-7	**5**, 175, 305	63	[153.66 - 273.88]	3	clivus chordoma
Prostate	**0**	61	[277.19 - 362.47]	N/A	squamous cell carcinoma

In the frame of this thesis, a comprehensive study was conducted involving eight patients treated with CIRT at HIT. This cohort consisted of:

- Five retrospective patients with head and neck tumors treated at HIT.
- Two patients enrolled in the InViMo clinical trial.
- One prostate cancer patient for whom an in-table monitoring simulation was explored.

For the five retrospective patients, the simulation based on the planning CT was considered as the first monitored fraction. The subsequent fraction using the follow-up was named based on the time interval between the planning CT and the follow-up CT. For patients monitored within the clinical trial, the available follow-up CTs were used, and comparisons were made with the closest monitored fractions to assess inter-fractional anatomical changes. In the prostate case, the planning CT was modified to emulate an air-filled rectal cavity. Details of the patient and treatment plan for each individual are provided in Table 3.2.

Chapter 4

Results

4.1 Retrospective Patient Cohort

The first part of the results presents the findings of Monte Carlo (MC) simulations performed using the developed FLUKA framework, as detailed in the Methods and Materials section, on a cohort of five retrospective cases treated with carbon ion radiotherapy (CIRT) at the Heidelberg Ion-Beam Therapy Center (HIT), see Table 3.2. The analysis focuses on key aspects of signal interpretation in ion treatment monitoring with charged nuclear fragments. The differences in Hounsfield Units (HU) between planning and follow-up computed tomography (CT) images of the simulated patients are analyzed and correlated with findings from the MC simulations. These findings include reconstructed fragmentation vertices, obtained by back-projecting the measured fragment paths; true fragmentation vertices (true FV) of the detected fragments, locations of all Heavy Ion Nuclear Interactions (HINIs) encompassing all hadronic inelastic and non-elastic interactions; and dose distributions. Additionally, the results of the Kolmogorov-Smirnov (KS) test are presented, which are used to compare distributions and identify statistically significant differences in fragment patterns. The global gamma index is used to to assess the impact of CT differences on the dose distribution using clinically relevant parameters: a dose difference tolerance of 3% and a spatial agreement criterion of 3 mm (distance-to-agreement).

In the presented CT slices throughout this section, the blue contour outlines the PTV, while the magenta cross represents the projection of the isocenter perpendicular to the axial plane.

4.1.1 Patient 1

Patient 1, diagnosed with mucosal melanoma, underwent CIRT using three beam angles: $5°$, $315°$, and $265°$. The selection of the beam angle for the retrospective patient cohort simulations was based on the constraints in the treatment room, where the InViMo detection system is anchored in a fixed position, as described in 3.1. The permissible table position range for monitoring was limited to either $0° \pm 15°$ or $180° \pm 15°$.

Among the three beam angles used in the treatment of Patient 1 , the $5°$ beam was chosen for simulation, as it falls within the measurable range and provides extensive coverage of

the PTV. This selection ensures a higher statistical yield in the generation and detection of charged nuclear fragments, facilitating a more robust evaluation of ion-beam treatment monitoring. The simulated beam consisted of 72 individual energy steps (IES), with energies ranging from 88.83 MeV/n to 247.74 MeV/n.

Figure 4.1 illustrates the dose distribution for the $5°$ beam, corresponding to one treatment fraction, overlaid on an axial CT slice at the isocenter. The dose distribution calculated using the HIT treatment planning system (from RTDose) is shown in Figure 4.1a. A visual comparison of the two dose distributions reveals that the simulation, performed with the FLUKA MC-based CIRT monitoring, shows good agreement with the HIT-calculated dose distribution. This confirms the reliability of the simulations in reproducing clinical dose distributions, which is essential for accurately modeling fragmentation generation and, consequently, for the performance of the monitoring method.

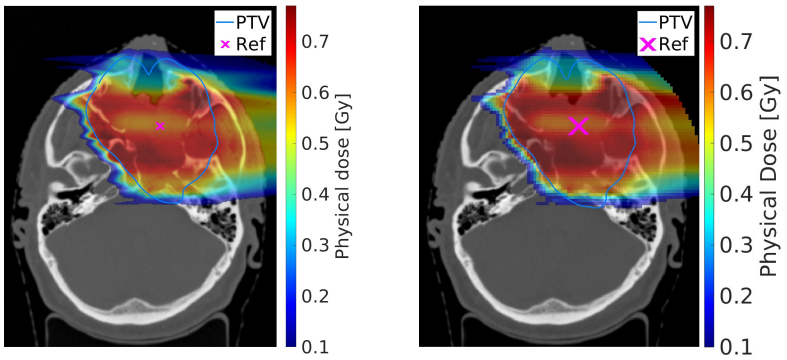

(a) Simulated dose distribution by FLUKA-MC.

(b) Planned dose distribution from RTDose.

Figure 4.1. Dose distribution of the $5°$ beam corresponds to one treatment fraction on top of an axial CT slice at the isocenter. The blue contour outlines the PTV, and the magenta cross marks the projection of the isocenter perpendicular to the axial plane.

Patient 1: CT anatomical changes

Figure 4.2 shows the HU differences, illustrating per-voxel differences between the planning CT and a follow-up CT taken 12 days apart. These differences highlight volumetric anatomical changes within a selected region of interest. Throughout this thesis, a threshold of 90 HU was chosen to account for uncertainties arising from various factors, including scanner variability influenced by noise, calibration drift, and registration uncertainties during dataset alignment. The spatial alignment between planning and control CT was performed using the DICOM registration object (REG).

The region of interest was selected based on visible anatomical changes and spans 5 mm inside the PTV, covering axial slices between -1.90 mm and -5.90 mm relative to the isocenter. Three axial CT slices from this region are displayed. The most notable differences within the PTV in this region are observed along the nasal cavity walls, highlighted in red, indicating potential filling due to tissue swelling or mucous accumulation. Additionally, alterations are visible in the skin of the left infraorbital region and along the skin border extending towards the ear, particularly evident in the amplified version of the Figure 4.2.

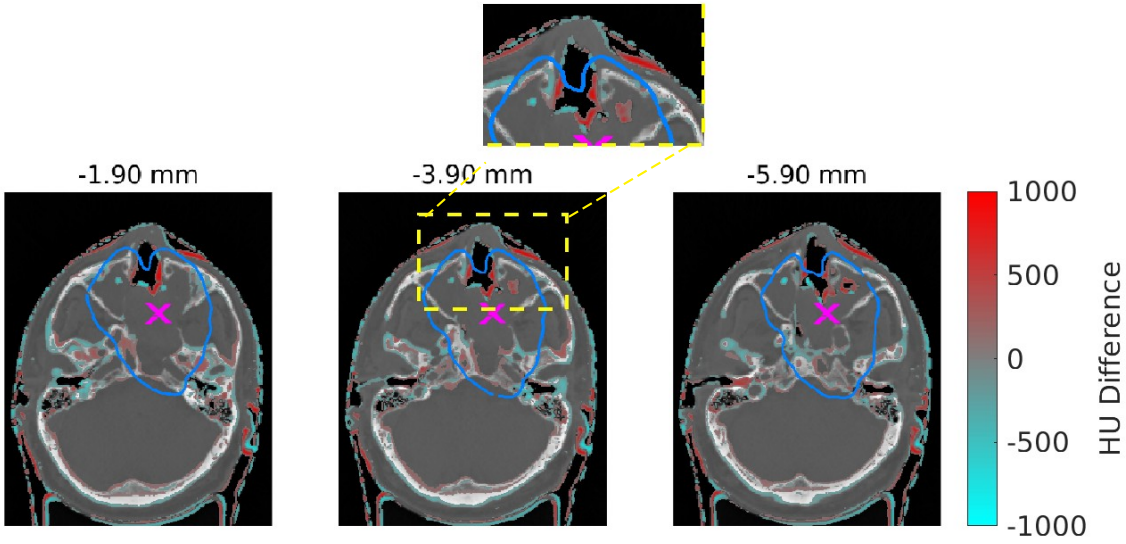

Figure 4.2. Anatomical changes between the planning and follow-up CTs, taken 12 days apart, based on HU differences. The HU differences shown represent voxel-by-voxel comparisons, with the CT voxel dimensions being $0.6 \times 0.6 \times 1.0\,\mathrm{mm}^3$. These changes are superimposed on the planning CT. The three images correspond to axial CT slices spaced 2 mm apart, representing the patient's anatomy and changes over a 5 mm span. Slice positions relative to the isocenter are indicated above each image.

The volume differences were estimated in the regions of interest to provide a quantitative assessment of volumetric-anatomical variations. To evaluate potential cavity filling or emptying, a threshold of 600 HU was considered for the calculation, enabling differentiation between air (-1000 HU), soft tissues (approximately -100 to 130 HU), such as adipose tissue, muscle, cartilage, and mucus and bones (> 150 HU). The estimated volumetric change within the PTV was $0.28\,\mathrm{cm}^3$. For the left infraorbital region, the changes were calculated in the 5 mm region encompassing axial slices from -1.90 mm to -5.90 mm relative to the isocenter, presented in Figure 4.2, with a volumetric change of $0.19\,\mathrm{cm}^3$.

Patient 1: Fragmentation vertex distributions

The interfractional CIRT monitoring of Patient 1 with a 12-day interval is presented in the first row of Figure 4.3, where the reconstructed FV from two treatment fractions is shown. For this analysis, two simulations were performed: the initial simulation utilized the planning CT to represent the treatment delivered during fraction 1, while the subsequent simulation assumed the follow-up CT, acquired 12 days later, corresponded to fraction 12 of the treatment.

Plots 1a and 1b in Figure 4.3 show an intense signal in the upper portion of the PTV (outlined in blue), where the probability of fragment production is higher due to the passage of primary carbon ions through the entrance region. The shape of the high-intensity region reflects the proximity and geometric arrangement of the detection system. The fragments follow a diagonal path influenced by the detection system's positioning, illustrating the attenuation of fragments as they traverse tissue before reaching the detectors. The magenta cross marks the isocenter projection in the axial plane, providing a reference for the relative

position between the patient and the detection system.

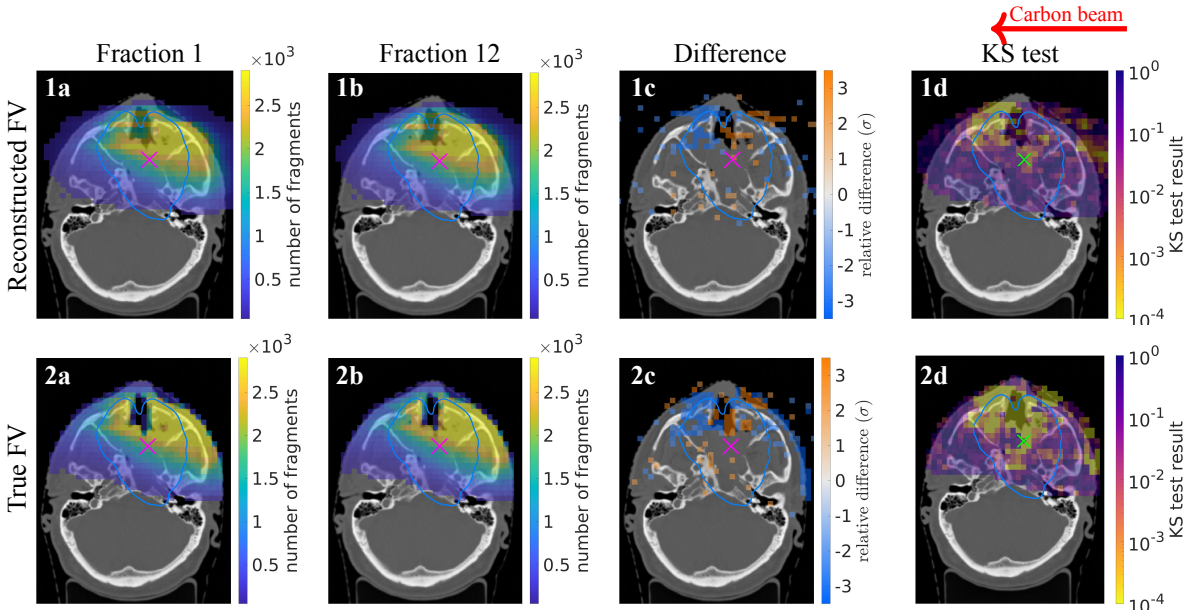

Figure 4.3. Distributions of reconstructed (row **1**) and true (row **2**) fragmentation vertices. Column **a** presents the distributions from the simulation using the planning CT (fraction 1), while column **b** shows the distributions from the simulation using the follow-up CT (fraction 12). Column **c** illustrates the differences between these two simulations. The voxel size for displaying the distributions and differences is (5.0 x 5.0 x 5.0) mm^3. In column **d** presents the p-values from the Kolmogorov-Smirnov (KS) test calculated within each 5 x 5 mm voxel region along the x-axis (perpendicular to the axial plotting slice). The data is overlaid on the planning axial CT slice at -3.90 mm relative to the isocenter, except in column **b**, where the follow-up CT slice is used.

In addition to attenuation effects, the reduced number of pencil beams in the bottom of the PTV region further decreases the likelihood of fragment rise. Furthermore, fragments originating from higher pencil beams and from further upstream require lower emission angles to reach the detectors.

To further minimize the influence of statistical fluctuations on the analysis of the signal, only differences greater than two standard deviations (2σ) are displayed in plot 1c in Figure 4.3. Plot 1c reveals a diffuse increase in signal near the upper cheek and along the left nasal wall, corresponding to an increase of tissue mass in these areas, which enhances fragment production.

The decrease in fragment signal behind the tissue increase occurs because the FVs are shifted by the thickness of the added tissue. As a result, fewer fragments are produced in the region posterior to the tissue increase.

Plot 1d in Figure 4.3 shows p-values from the Kolmogorov-Smirnov (KS) test, highlighting a large signal region posterior to the nasal cavity, as well as the skin border on the beam entry side. Based on this, the results suggest that anatomical changes in these areas significantly alter the fragment distributions.

When comparing the true FV distributions (plots 2a and 2b) with the reconstructed FV distributions (plots 1a and 1b) in Figure 4.3, the reconstructed distributions appear more

diffuse. This is expected, as Coulomb scattering of the fragmented secondary ions can alter their trajectories, thereby increasing the uncertainty in the reconstruction of their vertices. As illustrated in plots 2a and 2b, the diagonal pattern is more pronounced, reflecting the spatial relationship between the fragment generation vertices and the positioning of the detectors.

Since plots 2a and 2b exhibit similar distributions, further examination in plot 2c reveals an increase in fragment generation in the cheek region near the nose when comparing fraction 12 to fraction 1. Additionally, an increase is observed along the inner left wall of the nasal cavity, likely due to a slight increase in tissue mass in these areas (e.g., due to swelling), as shown in Figure 4.2, leading to enhanced fragment production. These anatomical changes directly impact fragment generation, resulting in a reduction of detected fragments posterior to the nasal cavity. This reduction is attributed to cavity filling, which decreases the number of primary particles passing through the nasal region. Furthermore, a reduction is evident on the left side of the face at the beam entry point, correlating with a slight alteration in the skin boundary, also observed in Figure 4.2.

In plot 2d of Figure 4.3, a prominent signal is observed throughout the region surrounding the nasal cavity, extending towards the upper edge of the cheek. Additionally, a low p-value region is identified along the skin boundary leading to the ear, indicating subtle changes in tissue density in this area.

Patient 1: Heavy Ion Nuclear Interactions (HINI)

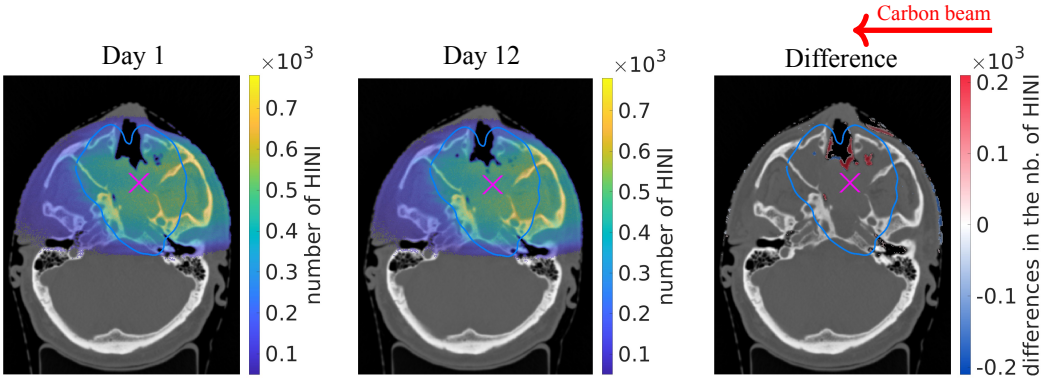

Figure 4.4. Heavy Ion Nuclear Interactions (HINI) from the simulation using the planning CT (fraction 1), the follow-up CT (fraction 12), and the absolute differences between these two simulations (difference). The data voxel size is (0.6x0.6x1.0) mm^3 and is overlaid on axial CT slices at -3.90 mm relative to the isocenter. The distribution from fraction 1 and the absolute difference are displayed on the planning CT, while the distribution from fraction 12 is overlaid on the follow-up CT.

Figure 4.4 shows the HINI distribution, which refers to all hadronic inelastic and non-elastic interactions encompassing potential nuclear interactions along the carbon-ion beam's path within the tissue, for the two simulated treatment fractions, numbers 1 and 12. Each voxel in these images represents the number of HINI events per $(0.6 \times 0.6 \times 1.0)\,mm^3$, mapped at the axial CT slice position of $-3.90\,mm$ relative to the isocenter. In both fractions, yellow

regions highlight areas of higher HINI density where the primary carbon ions encounter the densest tissue.

The distribution for fraction 12 shows notable differences in HINI density and CT values (4.2) in the nasal region compared to fraction 1. The difference plot (right) localizes and quantifies these changes, revealing an increased number of hadronic interactions in the wall of the nasal cavity inside the PTV, as well as in the upper part of the left paranasal sinus and the adjacent skin. Additionally, a slight reduction in HINI events is observed on the skin surface extending toward the left ear at the beam's entry point.

Patient 1: Simulated physical dose

Figure 4.5 shows the simulated physical dose distributions from a single fraction of the $5°$ treatment field, the absolute differences, and the results of the gamma index analysis. The values shown correspond to voxel sizes of $(0.6 \times 0.6 \times 1.0)\,\mathrm{mm}^3$. The plot visualization threshold was set to $0.1\,\mathrm{Gy}$ for dose and 5% for dose difference. The latter is a commonly used dose difference threshold at HIT for evaluating treatment plan quality.

The small volumetric anatomical changes between CTs resulted in a slight overdose in the lower part of the PTV, while changes in the nasal region led to minor dose variations before and after the PTV at this level. The fourth plot provides a gamma index analysis, yielding an overall pass rate of 99.28%, indicating a high degree of agreement between the dose distributions. In the CT slice at $-3.90\,\mathrm{mm}$ relative to the isocenter, no regions were identified where the acceptance criteria were not met.

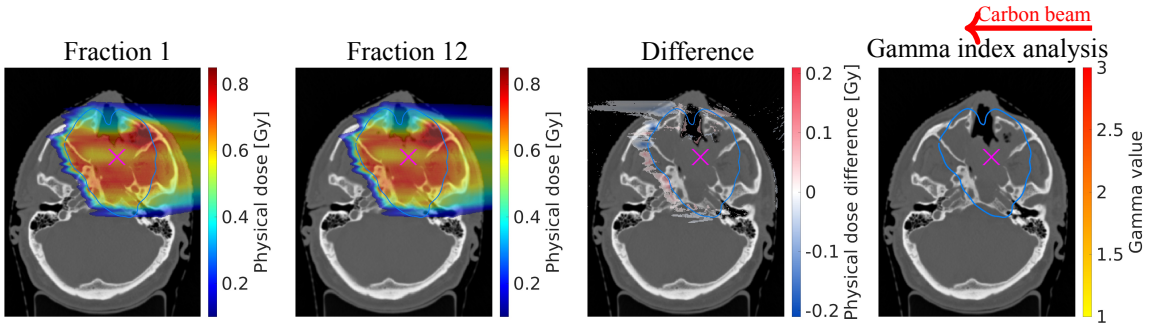

Figure 4.5. Simulated physical dose distributions corresponding to one fraction of the $5°$ treatment field from the simulation using the planning CT (fraction 1), the follow-up CT (fraction 12), and the absolute differences between these two simulations (difference). The fourth plot presents the Gamma index analysis. The data is overlaid on axial CT slices at -3.90 mm relative to the isocenter, except in the second column, where the follow-up CT is used. The CT and dose data voxel size is $(0.6\text{x}0.6\text{x}1.0)\,\mathrm{mm}^3$.

In summary, anatomical variations of $0.28\,\mathrm{cm}^3$ within the PTV were found when comparing the two CTs (Figure 4.2); however, these did not lead in to clinically relevant differences in the dose distribution (Figure 4.5). No voxels failed to meet the gamma index acceptance criteria, and the overall gamma pass rate exceeded 99%. Despite the small magnitude of these changes, the reconstructed FV distribution showed a clear signal of variation in the nasal region (Figure 4.3). The true FV distributions confirmed the correspondence

between the reconstructed FV signal and the underlying anatomical differences. The superficial location of the anatomical changes likely contributed to their detectability.

4.1.2 Patient 2

Patient 2: CT anatomical changes

For the second patient in this section, Patient 2, treated for adenoid cystic carcinoma (ACC), the analysis begins by evaluating the dose distribution between simulations performed using CTs taken 15 days apart, emulating fractions 1 and 15. The treatment plan consisted of three beam angles (see Table 3.2), with the $175°$ ipsilateral treatment field selected for simulation. Figure 4.9 shows the dose distribution per fraction for this simulated field, with a voxel size of $(0.6 \times 0.6 \times 1.0)\,\mathrm{mm}^3$ at an axial position of $15.00\,\mathrm{mm}$ relative to the isocenter.

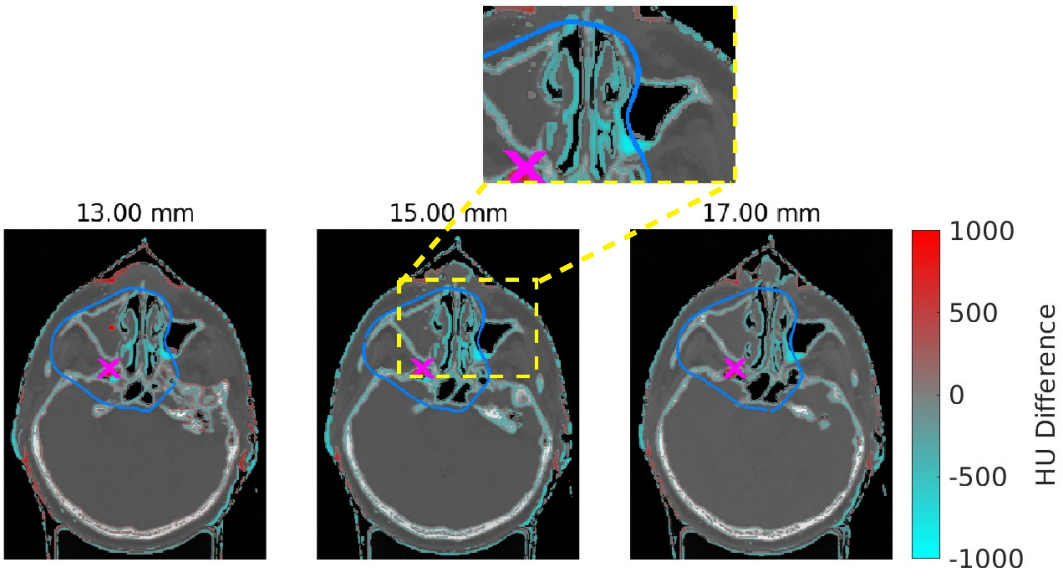

Figure 4.6. Anatomical changes between the planning and follow-up CTs, taken 15 days apart, based on HU differences. The HU differences shown represent voxel-by-voxel comparisons, with the CT voxel dimensions being $(0.6 \times 0.6 \times 1.0)\,\mathrm{mm}^3$. These changes are superimposed on the planning CT. The three images correspond to axial CT slices spaced 2 mm apart, representing the patient's anatomy and changes over a 5 mm span. Slice positions relative to the isocenter are indicated above each image.

Figure 4.6 shows anatomical differences between the planning and follow-up CTs, corresponding to Fractions 1 and 15, based on HU variations. Regions of change are visible along the walls of the turbinates, as well as a minor filling in the posterior portion of the left maxillary sinus. Additionally, alterations are observed in the cavity located below the "x" marking the projection of the isocenter.

The amplified region in Figure 4.6 enables visualization of these anatomical variations within a $5\,\mathrm{mm}$ axial stack, ranging from $13.00\,\mathrm{mm}$ to $15.00\,\mathrm{mm}$. Within this region, a volumetric change of $0.60\,\mathrm{cm}^3$ was estimated.

Patient 2: Fragmentation vertices distributions

Figure 4.7 shows the distribution of reconstructed and true fragmentation vertices (FVs) for the simulated fractions 1 and 15. An increase in concentration of fragments is observed near the upper beam entrance, as shown in plots 1a-b and 2a-b. Furthermore, a reduction in fragment concentration can be observed along a diagonal trajectory extending from the upper right to the lower left of the PTV. This diagonal reduction is caused by the detection system's relative position with respect to the patient, which defines the trackpath of the detected fragments. The reconstructed FVs in plots 1a-b appear more diffuse, in contrast to the more focused true FVs in plots 2a-b.

Column c in Figure 4.7 presents the relative difference between fractions 1 and 15. In plots 1c and 2c, the difference plot for reconstructed FV does not exhibit a clear, localized pattern, with variations dispersed across regions. More scattered signal appear within the PTV in the difference in true FV plot (2c), although no specific observations are noted.

Column (d), within the same plot, shows the results of the Kolmogorov-Smirnov (KS) test. In plot 1d, representing the reconstructed FV, a region of increased significance (in yellow) is observed in the posterior part of the left maxillary sinus. In contrast, plot 2d, corresponding to the true FVs, reveals additional changes in the skin of the right cheek, the right infraorbital area, and within the nasal cavity. A difference is also visible in the posterior region of the left maxillary sinus.

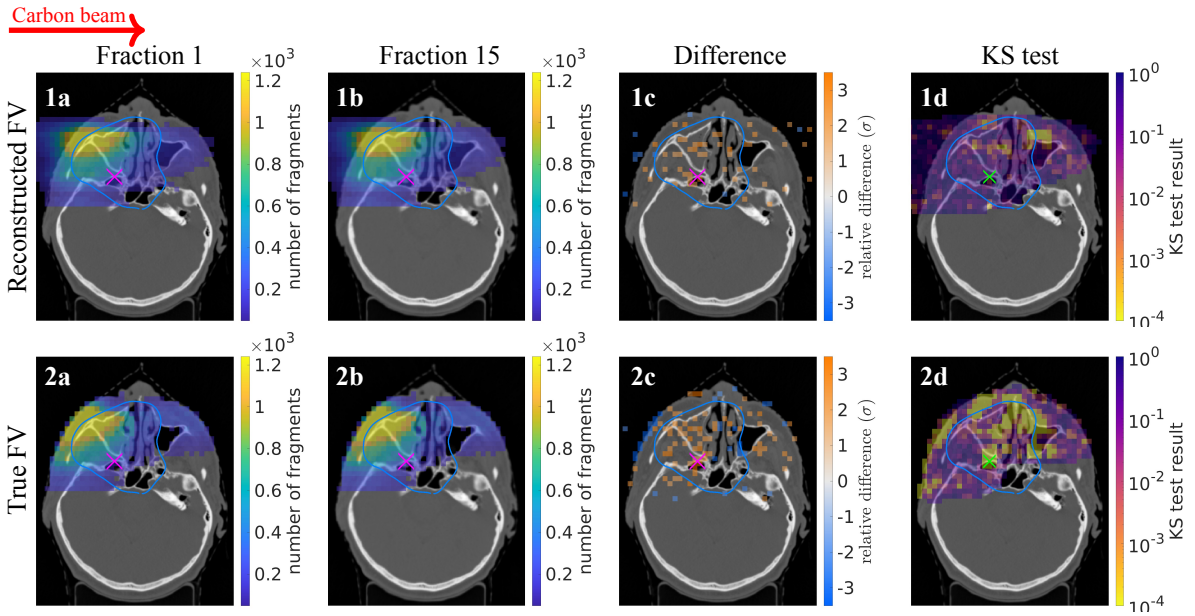

Figure 4.7. Distributions of reconstructed (**row 1**) and true fragmentation vertices (**row 2**) are shown. Column (**a**) displays the distribution using the planning CT (fraction 1), column (**b**) shows the follow-up CT (fraction 15). Column (**c**) illustrates the differences between both simulations. The voxel data size for the fragmentation distributions and differences is $(5.0 \times 5.0 \times 5.0)$ mm^3. The fourth column (**d**) presents the p-values from the Kolmogorov-Smirnov (KS) test, calculated within each 5×5 mm voxel region based on the data distribution along the x-axis (perpendicular to the axial plotting slice). The data is overlaid on the planning axial CT slice at 13.00 mm relative to the isocenter, except in the second column, where the follow-up CT is used.

Patient 2: Heavy Ion Nuclear Interactions (HINI)

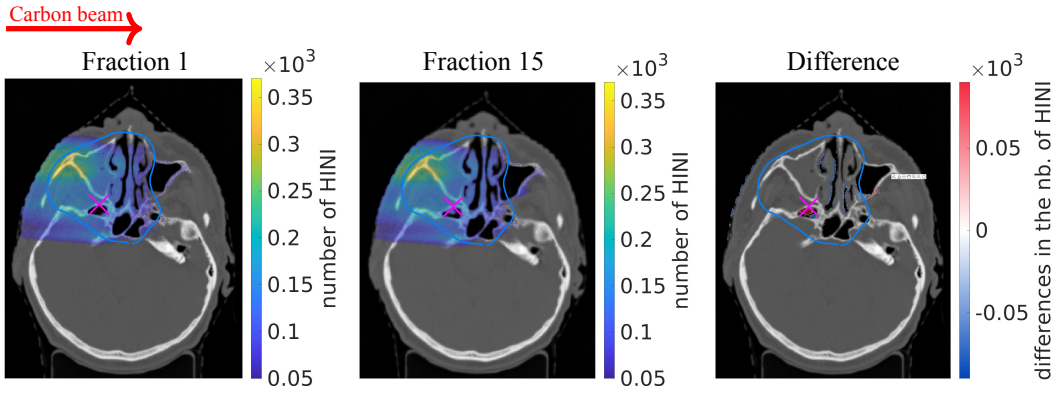

Figure 4.8. Heavy Ion Nuclear Interactions (HINI) from the simulation using the planning CT (fraction 1), the follow-up CT (fraction 15), and the absolute differences between these two simulations (difference). The data voxel size is (0.6x0.6x1.0) mm^3 and is overlaid on axial CT slices at 15 mm relative to the isocenter. The distribution from fraction 1 and the absolute difference are displayed on the planning CT, while the distribution from fraction 15 is overlaid on the follow-up CT.

Figure 4.8 displays Heavy Ion Nuclear Interactions (HINI) within each voxel of the CT scan for fractions 1 and 15, at an axial position of 15.00 mm relative to the isocenter. The distribution shows a higher number of interactions concentrated in denser tissues. This pattern correlates with the hot spot observed in the physical dose distribution in Figure 4.9, indicating a high concentration of delivered primary carbon particles in these regions. Given the sensitivity of HINI events to material composition and density, any change in tissue characteristics along the beam path strongly affects the number and spatial distribution of these interactions. In the difference plot in Figure 4.8, small differences are visible along the walls of the turbinates, as well as a minor filling in the posterior portion of the left maxillary sinus. Additionally, changes are observed in the cavity below the projection of the isocenter marked by the x.

Patient 2: Simulated physical dose distributions

In the difference plot in Figure 4.9, an overdosage is observed in the left nasal cavity and left maxillary sinus. This localized overdosage suggests that anatomical changes may have influenced the dose distribution in these specific regions. In the gamma index analysis plot, a region at the level of the left maxillary sinus did not meet the acceptance criteria, presenting a hot spot within its air-filled cavity. The gamma index analysis yielded a pass rate of 99.02%, indicating a high degree of agreement between the dose distributions for fractions 1 and 15.

In summary, the anatomical changes detected between the two CTs were primarily located in the walls of the nasal turbinates, corresponding to a distributed volumetric change of 0.60 cm^3, most likely due to mucosal swelling (Figure 4.6). These changes were relatively deep and centered in the midfacial region. The simulated dose distributions revealed regions failing the gamma index acceptance criteria, indicating a localized overdosage both inside and outside the PTV (Figure 4.9). As confirmed by the distribution of Heavy Ion

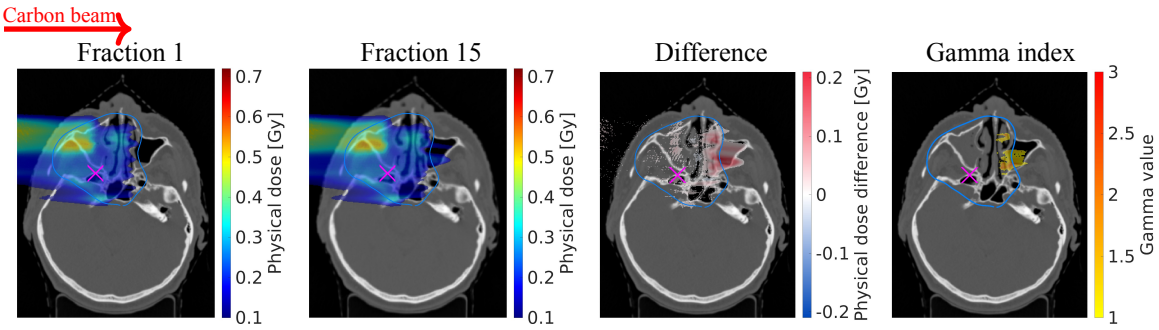

Figure 4.9. Simulated physical dose distributions corresponding to the 175° treatment field for one fraction. Column 1 shows the distribution from the simulation using the planning CT (fraction 1), column 2 shows the distribution using the follow-up CT (fraction 15), and column 3 shows the absolute differences between these two simulations. The fourth column presents the results of the Gamma index analysis. The data is overlaid on axial CT slices at 13.00 mm relative to the isocenter, except in column 2, where the follow-up CT at the same relative position to the isocenter is used. Both CT and dose data have a voxel size of (0.6x0.6x1.0) mm^3.

Nuclear Interactions (HINI) (Figure 4.8), the affected tissue volume was narrow and mainly distributed along the nasal walls.

Given the depth and limited extent of the anatomical changes, the probability of detecting these modifications using the fragment-based monitoring method was low. As seen in the differences of the reconstructed and true FV distributions (Figure 4.7), no conclusive or statistically significant signal could be identified. The true FV distribution also suggests the presence of additional superficial changes, possibly related to de-swelling, overlapping with the internal anatomical modifications along the beam's eye view. This overlap may further obscure the detectability of the deeper variations.

4.1.3 Patient 3

Patient 3: CT Anatomical changes

The patient, diagnosed with adenoid cystic carcinoma (ACC), was treated using a three-beam plan, with the 175° beam selected for simulation. Two CT scans, taken 46 days apart, were used for the analysis. In the case of Patient 3, three distinct regions along the axial anatomy were identified, each exhibiting notable anatomical alterations, as illustrated in Figure 4.10.

The axial region 1 spans from -45.00 mm to -42.00 mm. In this area, two primary anatomical modifications are observed. The first occurs in the lower jaw at the level of the dental region, and the second involves changes in the skin of the left mental region. This region contains the inferior boundary of the PTV at an axial position of -42.00 mm.

The axial region 2 spanning from -2.00 mm to 2.00 mm, also exhibits significant anatomical changes between day 1 and day 46. These include indications of possible tissue inflammation inside the PTV, as well as a tissue reduction of 1.63 cm^3 in the frontal part of the left maxillary sinus.

The axial region 3 is located between 22.00 mm and 26.00 mm, encompassing a 5 mm

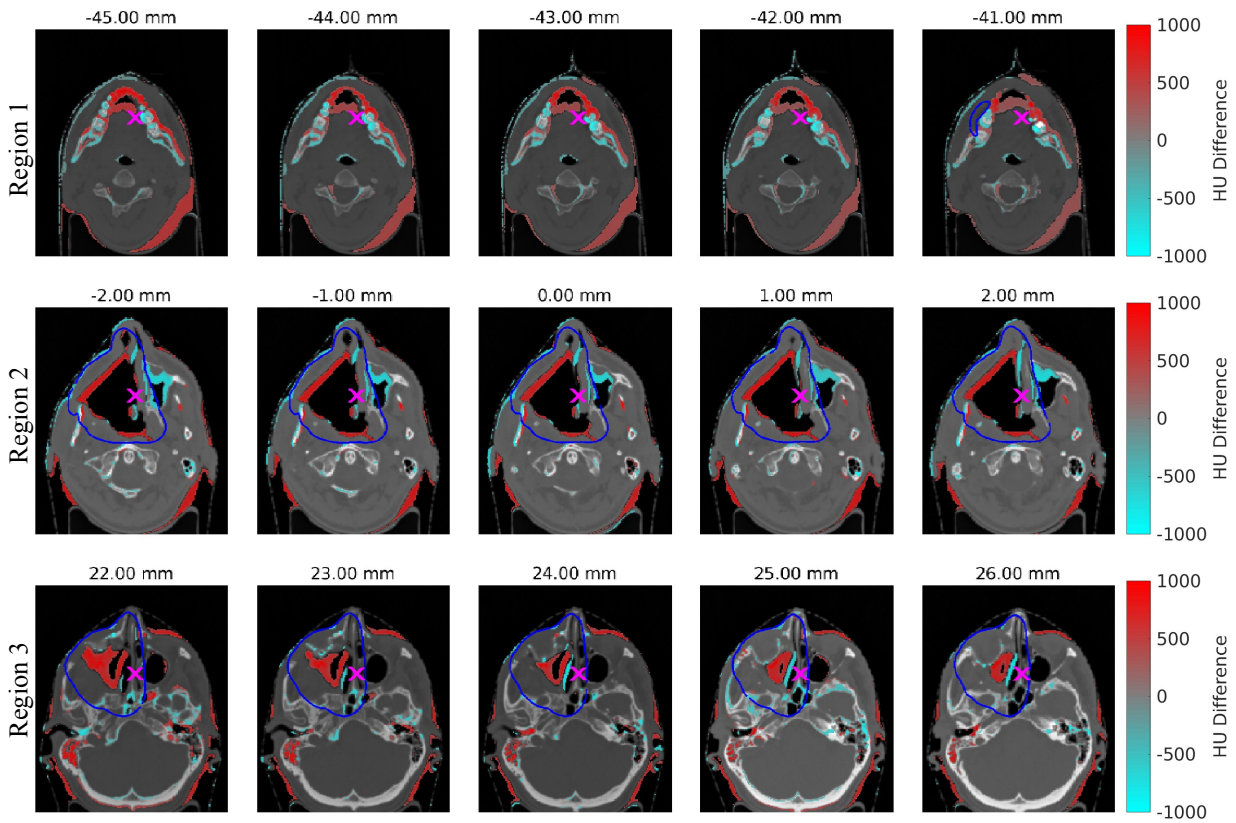

Figure 4.10. Anatomical changes between the planning and follow-up CT, taken 46 days apart, based on HU differences. Each row contains 5 axial CT images spaced 1 mm apart, covering a total of 5 mm of patient anatomy and representing an anatomical region where changes occurred. All changes are superimposed on the planning CT. Three regions are shown in total, and the slice positions, relative to the isocenter, are indicated above each image.

segment of the patient's axial anatomy. Within this region, anatomical alterations estimated at $3.46\,\mathrm{cm}^3$ are observed in the right maxillary sinus, inside the PTV (delineated in blue), as well as in the skin beneath the left infraorbital region.

Patient 3: Reconstructed fragmentation vertices distributions

Figure 4.11 illustrates the distribution of reconstructed FV for the three regions of interest in this patient. The first and second columns represent the reconstructed FV distributions for Day 1 and Day 46, respectively, while the third column shows the relative difference between these days. The data has a voxel size of $(5.0 \times 5.0 \times 5.0)\,\mathrm{mm}^3$.

Region 1, depicted in the first row, represents a $5.0\,\mathrm{mm}$-thick axial section centered at $-43.00\,\mathrm{mm}$. On Day 1 plot 1a, and Day 46 1b, the fragment distribution appears relatively uniform. This is influenced by the plot threshold, set at 60 fragments, and the potential impact of the detector system's solid angle. The relative difference plot 1c between Days 1 and 46 indicates a reduction in fragment signal from the right-side chin region. In Region 2, represented in the second row of Figure 4.11, the reconstructed fragments exhibit a more intense signal around the nasal area in the upper frontal part of the PTV. On Day 46 2b, the concentration of fragments in this area increases, leading to an enhanced proba-

bility of fragment generation. The relative difference plot 2c demonstrates a characteristic "cavity-filling" effect, which is corroborated by observations in Figure 4.10. The reduced fragment signal in the region preceding the filled cavity suggests that the new tissue absorbs fragments. Conversely, within the area of possible inflammation or tissue infiltration, the fragment signal increases, while in the posterior region, fewer fragments are detected. This pattern indicates a reduction in the number of primary carbon particles reaching this area, thereby decreasing secondary fragment production.

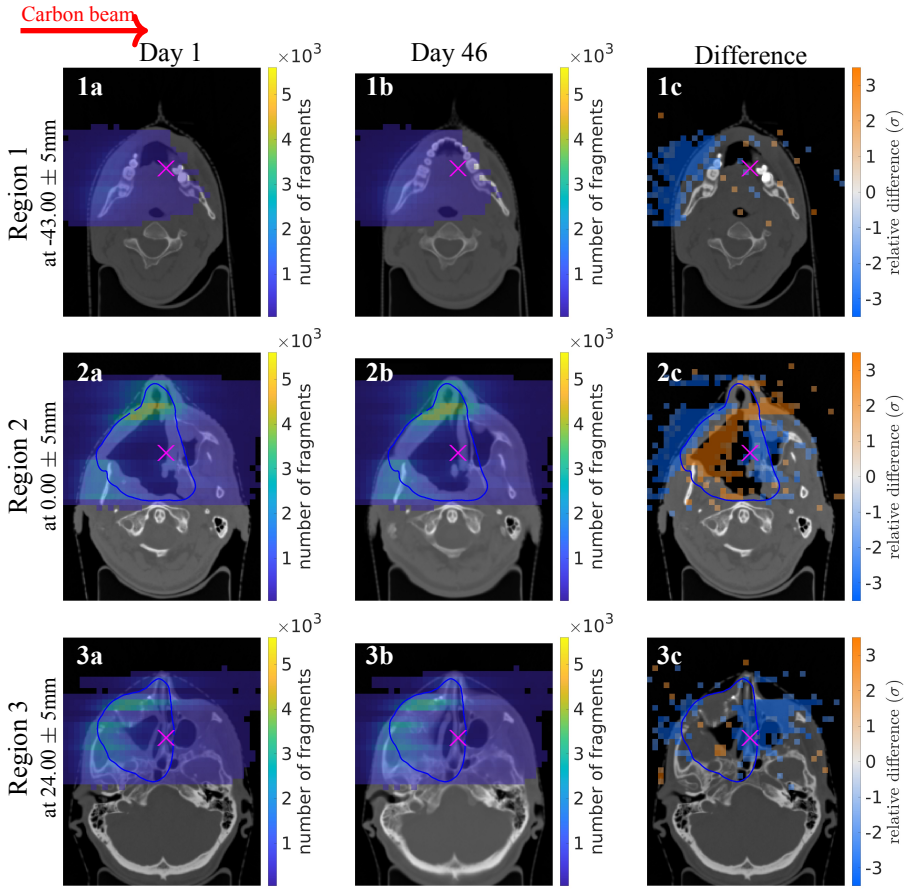

Figure 4.11. Distributions of reconstructed fragmentation vertices by regions (**1, 2, 3**) in each row. The first column (**a**) shows the distribution from the simulation using the planning CT (day 1), while the second column (**b**) presents the distribution from the simulation using the follow-up CT (day 46). The third column (**c**) illustrates the differences between these two simulations. The data is overlaid on axial planning CT slices, except in the second column, where the follow-up CT is used. The voxel size in all plots is (5.0x5.0x5.0) mm^3.

Region 3, situated at a distance of 26.00 mm along the axial plane, does not exhibit significant changes in a visual comparison of the distributions on Day 1 (plot 3a) and Day 46 (plot 3b). However, the relative difference in plot 3c indicates a notable reduction in fragment signal in the posterior portion of the PTV and along its left side. Minor alterations are also visible on the skin surface, particularly in the right cheek region, corresponding to the beam's entry point.

Patient 3: True fragmentation vertices distributions

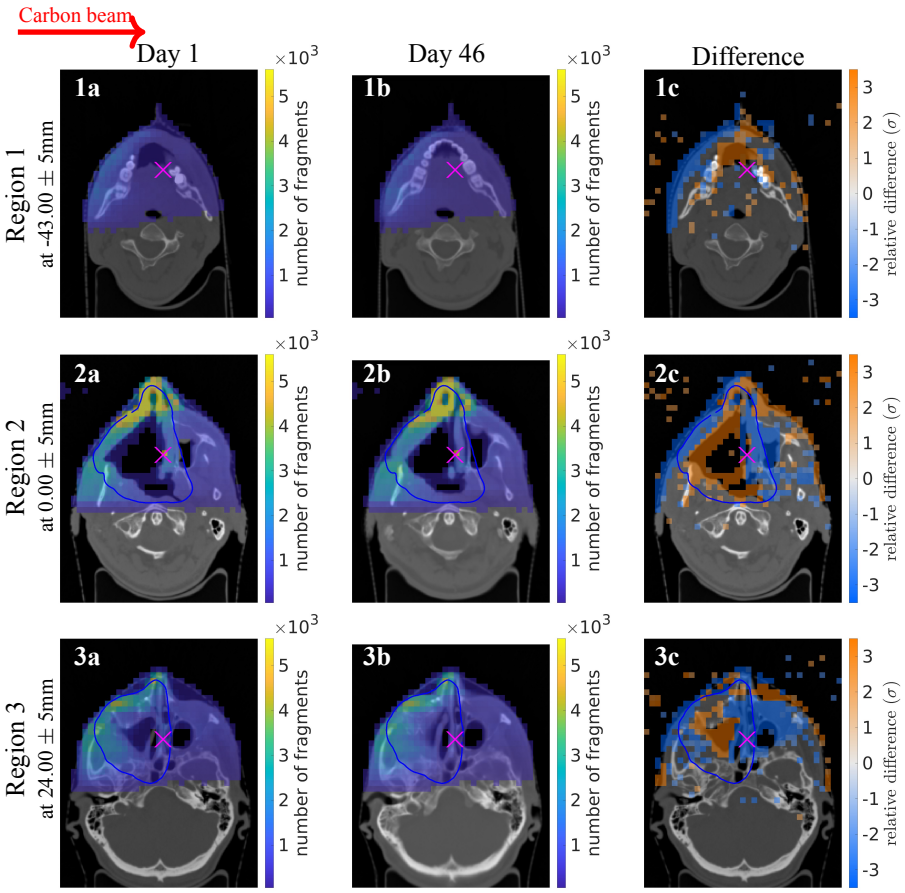

Figure 4.12. Distributions of true fragmentation vertices by regions (**1, 2, 3**) are displayed in each row. The first column (**a**) represents the distribution from the simulation based on the planning CT (day 1), while the second column (**b**) shows the distribution using the follow-up CT (day 46). Column three (**c**) depicts the differences between the two simulations. The data is overlaid on axial planning CT slices, except for column two, where the follow-up CT is utilized. The voxel size in all plots is (5.0x5.0x5.0) mm^3.

In Region 1, illustrated in Figure 4.12, plots 1a and 1b display the true FV distributions for Day 1 and Day 46, respectively. On Day 1 (plot 1a), an even distribution of fragments is observed, with a slight increase in concentration near the beam's entry point. By Day 46 (plot 1b), a reduction in fragment signal is noticeable, particularly at the beam entry point, while an increase in fragment intensity is observed in the upper left region near the chin area.

The relative difference (plot 1c) illustrates a reduction in fragment signal along the right border of the head in the skin region. This decrease may indicate denser oral cavity tissue absorbing fragments, thereby preventing them from reaching the posterior areas. Additionally, this reduction may be attributed to subtle changes or shifts in the skin around the right cheek. Conversely, an increase in fragment production is observed within the oral cavity, extending to the left mentonian region.

Region 2, illustrated in Figure 4.12, is centered around the isocenter and depicted in plots 2a and 2b, which show the true fragmentation vertex distributions for Day 1 and Day

46, respectively. A higher concentration of fragments is observed in the upper frontal area near the nose, where fragments have a shorter travel distance to the detection system and encounter less intervening tissue. The relative difference (plot 2c) demonstrates a notable reduction of fragments within the area immediately preceding the filled cavity. Subsequently, an increase in fragment counts is observed in the region of possible inflamed or infiltrated tissue. Beyond this cavity, fragment production decreases, as fewer primary carbon particles penetrate into the posterior portion of the left maxillary sinus. In Region 3, the distributions of true FV are found to be very similar between the days of the simulated CTs, as illustrated in plots 3a and 3b. The relative difference plot 3c reveals similar differences when compared to plot 2c, where the cavity-filling effect was described, along with variations observed at the left skull border of the patient's head.

Patient 3: Heavy Ion Nuclear Interactions (HINI)

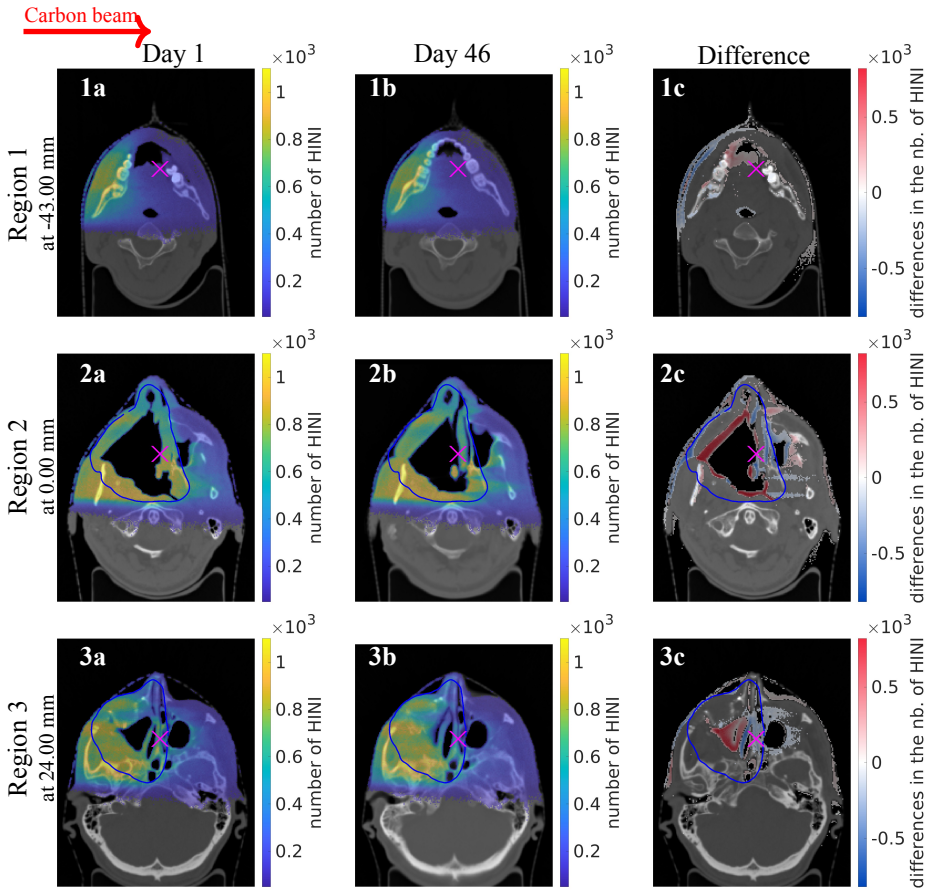

Figure 4.13. Heavy Ion Nuclear Interactions (HINI) by region (rows **1, 2, 3**) from the simulation using the planning CT (Day 1 in column **a**), the follow-up CT (Day 46 in column **b**), and the absolute differences between these two simulations (differences in column **c**). The data voxel size corresponds to the CT voxel size, which is (0.6x0.6x1.0) mm^3.

As illustrated in Figure 4.13, the distribution of Heavy Ion Nuclear Interactions (HINI) across three regions of interest in Patient 3 corresponds to distinct anatomical changes identified in HU differences between the 2 CTs in Figure 4.10. Region 1, located in the posterior

portion of the PTV near the beam entry, shows a slight reduction in HINI counts near the beam entry and along the left side of the region, as indicated by the difference plot 1c. Additionally, a slight increase in HINI interactions is observed in the buccal region.

Region 2, centered around the isocenter and including part of the nasal cavity, shows similar trends. The difference plot 2c indicates an increase in HINI interactions along the inner border of the cavity in the PTV, as well as small differences in the left maxillary sinus and other scattered regions.

The region 3, corresponding to the lower boundary of the PTV and including the maxillary sinuses, shows an increase in the number of HINIs in the filled right maxillary sinus cavity and a decrease in HINI counts in the posterior part of this region, as indicated by the difference plot 3c. All observed changes in the number of HINIs are consistent with the anatomical modifications seen in Figure 4.10.

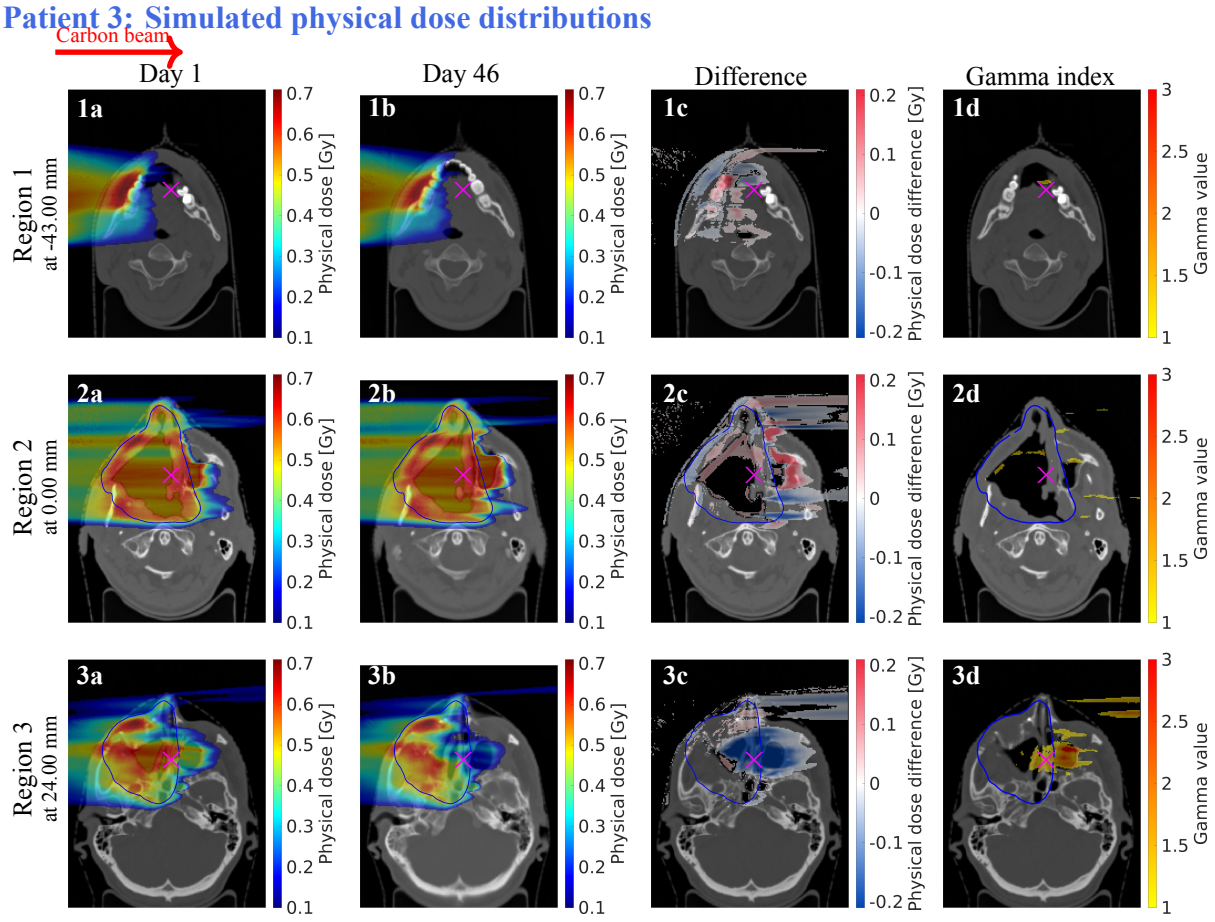

Figure 4.14. Simulated physical dose distributions by regions (rows **1, 2, 3**) corresponding to the 175,° treatment field for one fraction. The distributions from the simulation using the planning CT (Day 1) are shown in column **a**, from the follow-up CT (Day 46) in column **b**, and the absolute differences between these two simulations in column **c**. The fourth column (**d**) presents the results of the Gamma index analysis. The data is overlaid on axial planning CT slices, except in column **b**, where the follow-up CT is used. Both CT and dose data have a voxel size of (0.6x0.6x1.0) mm^3.

Figure 4.14 shows the simulated physical dose distributions at the central axial slice of three regions of interest (rows 1, 2, and 3) within a CT resolution of (0.6x0.6x1.0) mm^3 for a single

fraction of the 175° treatment field. The gamma index pass rate results for this patient were 93.87%.

Dose differences are visible across all three regions. In Region 1 (first row), plot 1c presents various small dose differences in the overall dose distribution, but none were identified by the gamma analysis. In plot 1d, particularly in the presented axial slice at -4.30, only a small area within the oral cavity shows any signal. In Region 2 (second row), difference plot 2c displays variations throughout the irradiated region, with a notable increase in dose in the left maxillary sinus. However, only minor indications in plot 2d suggest significant dose differences based on the gamma analysis. In Region 3 (third row), the area around the midfacial region in plot 3c shows an underdose. The nose and its tip contribute to this dose difference detected in the air in the upper left part of the plot. These two previously mentioned dose differences are also reflected in plot 3d, where the gamma index highlights these discrepancies.

In summary, Patient 3 presented substantial anatomical changes in three distinct axial regions, with volumetric changes up to $3.46\,\mathrm{cm}^3$ within the right maxillary sinus, along with smaller alterations observed in the lower jaw and nasal cavity areas (Figure 4.10). These changes were of greater magnitude compared to the other patients in the cohort. The gamma index pass rate for this patient was lower (93.87%) compared to the other cases presented in this thesis.

The reconstructed FV distributions (Figure 4.11) captured some of these anatomical variations in Region 2, where a characteristic "cavity-filling" effect was observed. However, in Regions 1 and 3, which are located farther from the isocenter, detecting localized changes proved more challenging, likely due to deeper fragment generation and longer path lengths, which increase the probability of fragment stopping in tissue. Nonetheless, in all three regions, most of the observed dose differences were located outside the PTV, in non-clinically relevant areas such as air cavities.

4.1.4 Patient 4

Patient 4: CT Anatomical changes

The following patient was treated with CIRT for an adenoid cystic carcinoma. Figure 4.15 shows anatomical changes between the planning CT and the follow-up CT, taken 12 days apart. The series captures a range of anatomical differences within a 5 mm span, from -2.50 mm to 1.50 mm axially relative to the isocenter. Red areas indicating the presence of additional tissue in the follow-up CT are predominantly observed across the CT slices in the region of the sphenoidal sinus at the posterior part of the PTV, with an estimated volume of $0.97, \mathrm{cm}^3$, as well as in the left infraorbital skin area, with a volume change of $0.51, \mathrm{cm}^3$. Small turquoise areas are primarily located around the periphery of the nasal cavity and extend slightly toward the upper nasal passages. The total volume change within the PTV was $7.52\,\mathrm{cm}^3$.

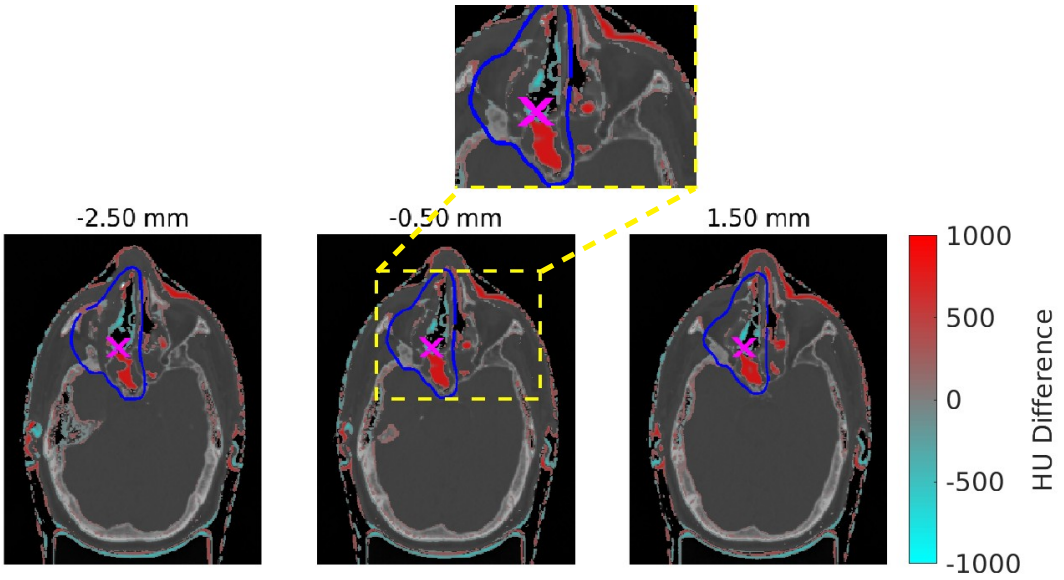

Figure 4.15. Anatomical changes between the planning and follow-up CTs, taken 12 days apart, are shown based on HU differences and superimposed on the planning CT. The three images represent 1 mm-thick axial CT slices spaced 2 mm apart, capturing the patient's anatomy and changes over a 5 mm span. Slice positions relative to the isocenter are indicated above each image.

Patient 4: Reconstructed fragmentation vertices distributions

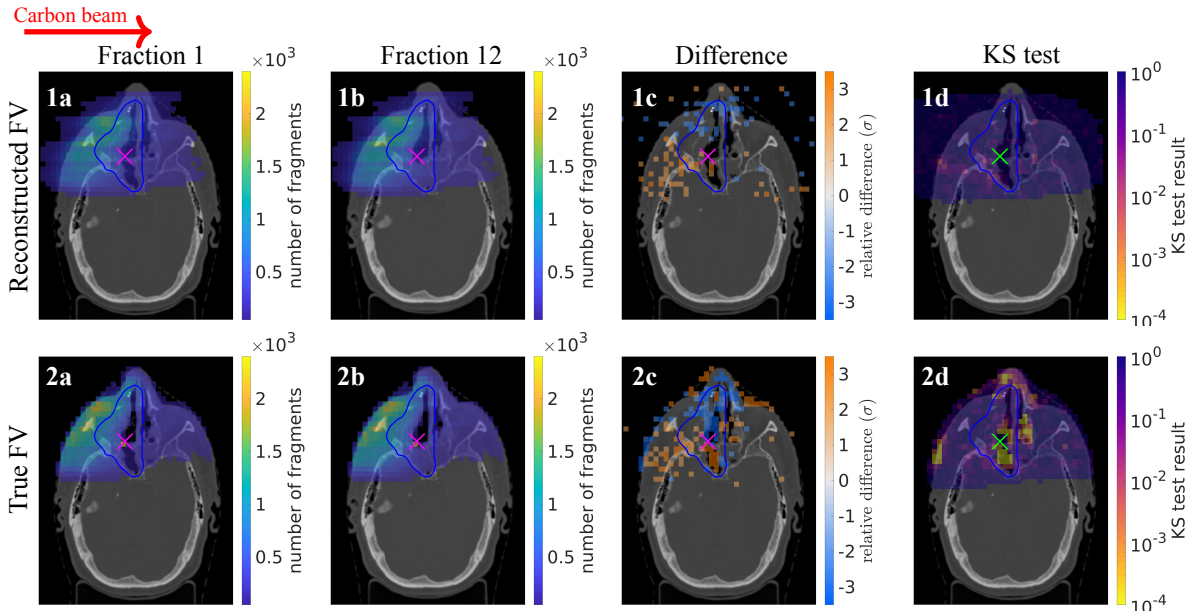

Figure 4.16. Distributions of reconstructed and true fragmentation vertices. The first column (**a**) displays the distribution from the simulation using the planning CT (day 1), while the second column (**b**) shows the distribution from the follow-up CT (day 12). Column **c** illustrates the differences between these two simulations, and column **d** presents the Kolmogorov-Smirnov test results comparing both distributions. The data is overlaid on axial planning CT slices, except for column **b**, where the follow-up CT is used. The voxel size in all plots is (5.0x5.0x5.0) mm^3.

The first row in Figure 4.16 depicts the distributions of reconstructed FV. The distributions for Day 1 and Day 12 are strikingly similar. In the difference plot 1c, a slight increase in fragment counts is observed in the lower region of the beam entry, while a decrease is visible in the upper area around the nose. However, these differences are distributed in a scattered manner and are not particularly localized, suggesting that the two distributions exhibit only subtle changes. The KS test plot reveals no specific regions exhibiting pronounced differences, indicating that statistically significant variations between Day 1 and Day 12 are minimal.

The true FVs are shown in the second row in Figure 4.16. The distributions for Day 1 and Day 12 appear to be similar overall, with fragmentation vertices concentrated along the beam entry path, particularly around the left zygomatic bone. However, the difference (plot 2c) demonstrates more substantial alterations. A reduction in fragment production is evident in the nasal area and the skin in the vicinity of the left ear. The reduction in the nasal cavity indicated a "cavity-emptiness" effect. An increase in the skin region in the left infraorbital area. Moreover, an increase in the sphenoid sinus is visible. In the KS test (plot 2d), signals are concentrated in the nasal region, extending into the left infraorbital area, as well as in portions of the skin on the left side of the head. Additional significant signals are observed within the sphenoid sinus and the left nasal cavity, indicating regions where statistically significant differences between the Day 1 and Day 12 distributions are present.

Patient 4: Heavy Ion Nuclear Interactions (HINI)

Figure 4.17 illustrates Heavy Ion Nuclear Interactions (HINI) from the simulation, using the planning CT on Day 1 and the follow-up CT on Day 12. In all three images, the presence of a cavity is apparent in the right sphenoid sinus, as observed in the HU differences shown in Figure 4.15. This is indicated by the strong signal in the difference plot, reflecting an increase in interactions within the cavity's region. Furthermore, minor changes are noticeable in the left nasal cavity, possibly due to the presence of mucus. Additionally, subtle variations along the edge of the right cheek are observable, which may result from the immobilization mask.

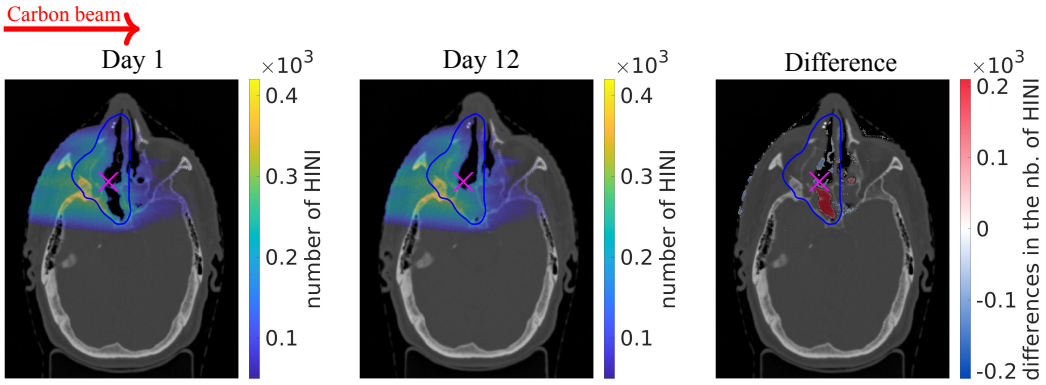

Figure 4.17. Heavy Ion Nuclear Interactions (HINI) from the simulation using the planning CT (Day 1 in column **a**), the follow-up CT (Day 12 in column **b**), and the absolute differences between these two simulations (differences in column **c**). The data voxel size corresponds to the CT voxel size, which is (0.6x0.6x1.0) mm^3.

Patient 4: Simulated physical dose distributions

A comparison of the simulated physical dose distributions resulting from a single fraction of the 175° treatment field is presented in Figure 4.18, revealing variations along the PTV boundary toward the left side at the isocenter axial slice volume. Specifically, there is a dose increase in the middle of the nasal cavity and a slight underdose along the lower left edge of the PTV. The gamma index result identifies these areas of significant change, emphasizing the regions with the most notable differences in dose occurred. The gamma pass rate was 98.83%.

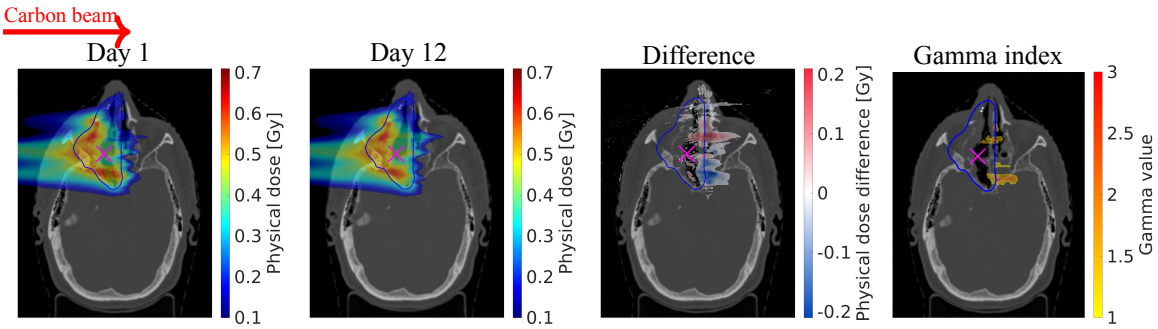

Figure 4.18. Simulated physical dose distributions corresponding to the 175° treatment field for one fraction. The simulation results using the planning CT (Day 1) are shown in column **a**, with the follow-up CT (Day 12) data in column **b**. Column **c** illustrates the absolute differences between the two simulations, and column **d** presents the results of the Gamma index analysis. The data is overlaid on axial planning CT slices, with the follow-up CT used in column **b**. CTs and dose data have a voxel size of (0.6x0.6x1.0) mm^3.

In summary, in Patient 4, complex clinically relevant anatomical changes were detected within the PTV, specifically a de-swelling in the nasal cavity and mucosal filling in the sphenoidal sinus (Figure 4.15). These anatomical changes led to localized regions of both overdose and underdose, occurring inside and outside the PTV. In these areas, the gamma index acceptance criteria were not met (Figure 4.18).

While the reconstructed FV distributions suggested a "cavity-emptying" effect, evidenced by increased signal before the nasal cavity and a reduction afterward, the deeper anatomical change in the sphenoidal sinus was not clearly visible. The reconstructed FV differences in the beam-eye-view correctly indicated the regions and direction of the changes. However, in the axial projection, the signal appeared more scattered, making it difficult to localize changes in depth. The true FV difference plot revealed the cavity-emptying effect and the sphenoidal sinus filling more distinctly, although the signal remained diffuse over the complex irradiation area. This demonstrates the challenge of accurately capturing deep-seated anatomical changes.

4.1.5 Patient 5

Patient 5: Anatomical changes CT

For this patient, anatomical changes represented in HU differences between the planning CT and the follow-up CT, taken 14 days apart, are depicted in Figure 4.19. In the region encompassing axial positions from $24.00\,\text{mm}$ to $28.00\,\text{mm}$ relative to the isocenter, at the level of the maxillary sinuses, both sinus cavities differ in filling. In this axial region, the left sinus, which is within the PTV, had an estimated volumetric change of $1.55\,\text{cm}^3$, while the contralateral maxillary sinus had a change of $0.77\,\text{cm}^3$. Another change can be observed in the zoomed image of Figure 4.19 at the level of the right nasal fold in the infraorbital region, where the volumetric change was estimated to be $0.35\,\text{cm}^3$. Within the entire PTV, a volumetric change of $6.21\,\text{cm}^3$ was observed, which represents only 2% of the voxels in the PTV volume.

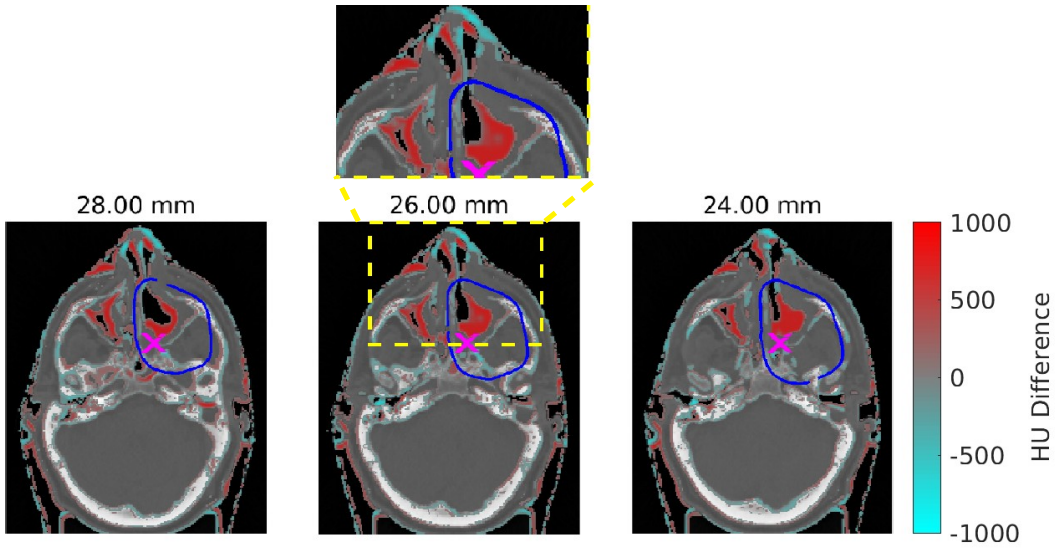

Figure 4.19. Anatomical changes between the planning and follow-up CTs, taken 14 days apart, based on HU differences. The HU differences represent voxel-by-voxel comparisons, with the CT voxel dimensions being $(0.6 \times 0.6 \times 1.0)\,\text{mm}^3$. These changes are superimposed on the planning CT. The three images correspond to axial CT slices spaced 2 mm apart, representing the patient's anatomy and changes over a 5 mm span. Slice positions relative to the isocenter are indicated above each image.

Patient 5: Fragmentation vertices distributions

In the first row of Figure 4.20, plots 1a and 1b depict the reconstructed FV detected, in the simulation, within the system for CTs equivalent days of fractions 1 and 15, respectively. In the difference plot 1c, an increase in the reconstructed FV signal is observed in the entry region of the PTV. However, no statistically significant differences are detected in the p-value map shown in plot 1d, as calculated by the KS test.

In the second row, plots 2a and 2b show the true FV for fractions 1 and 15, respectively. The differential plot 2c reveals the characteristic footprint of a cavity filling. Specifically, there is an increase in fragment production upstream and in the denser tissue of the left

sinus, followed by a reduction in the immediate posterior region. The p-value map in plot 2d highlights a region of intense signal in the medial section of the nasal cavity.

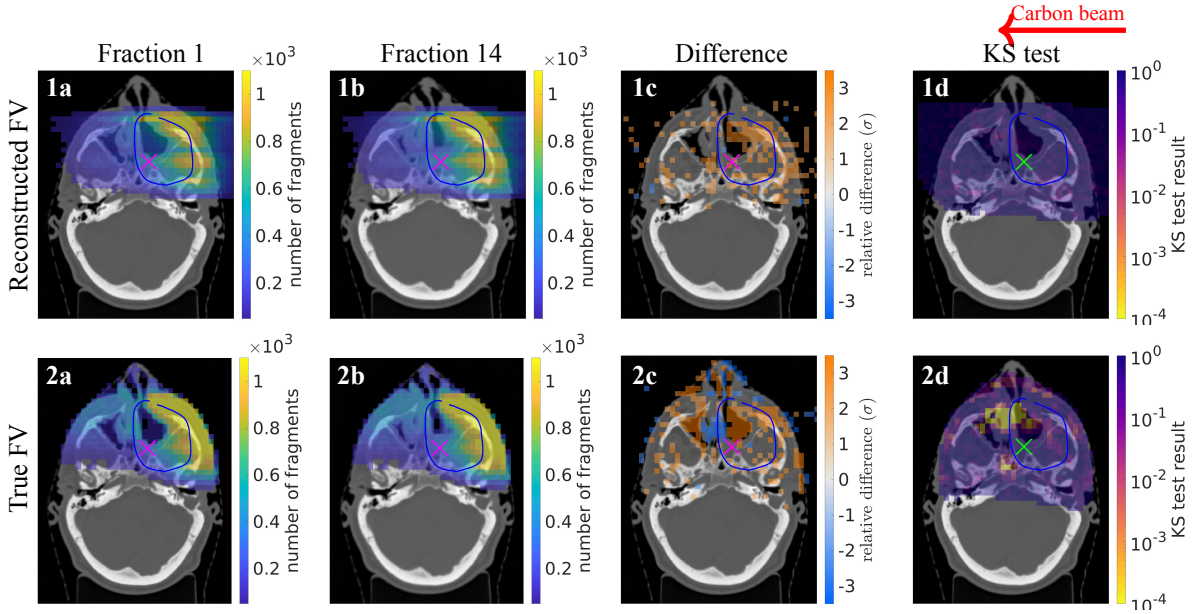

Figure 4.20. Distributions of reconstructed (**row 1**) and true (**row 2**) fragmentation vertices are shown. Columns (**a**) and (**b**) present results from simulations using the planning CT (fraction 1) and follow-up CT (fraction 15), respectively. Column (**c**) shows voxel-by-voxel differences, and column (**d**) displays p-values from the Kolmogorov-Smirnov (KS) test along the x-axis. A voxel size of $(5.0 \times 5.0 \times 5.0)\,\mathrm{mm}^3$ is used, and data are overlaid on axial CT slices at 26.00 mm relative to the isocenter.

Patient 5: Heavy Ion Nuclear Interactions (HINI)

Compared with the HU differences between the patient CTs (Figure 4.19), the areas of observed signal change are consistent, as can be seen in Figure 4.21. The border of the infraorbital region in the right shows an increase in tissue density and the plot highlights the magnitude of density changes in the left maxillary sinus within the PTV volume.

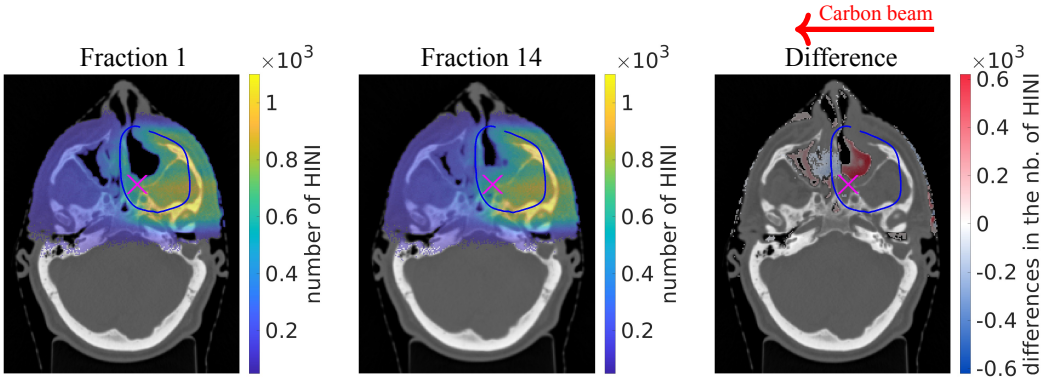

Figure 4.21. Heavy Ion Nuclear Interactions (HINI) from the simulation using the planning CT (Fraction 1 in column **a**), the follow-up CT (Fraction 14 in column **b**), and the absolute differences between these two simulations (column **c**). The voxel size of the data corresponds to the CT voxel size, which is (0.6x0.6x1.0) mm^3.

Patient 5: Simulated physical dose distributions

As illustrated in Figure 4.22, the physical dose distribution for a single fraction of the 0^o simulated treatment field shows the impact of a filled left maxillary sinus on the range of the primary carbon ions. This results in a slight underdosage in the central part of the face, within the rightmost section of the PTV. The gamma analysis demonstrates that the region within the PTV remains largely unaffected, with the most significant differences occurring in the air-filled cavity on the right side. The gamma index passing rate is 98.85%.

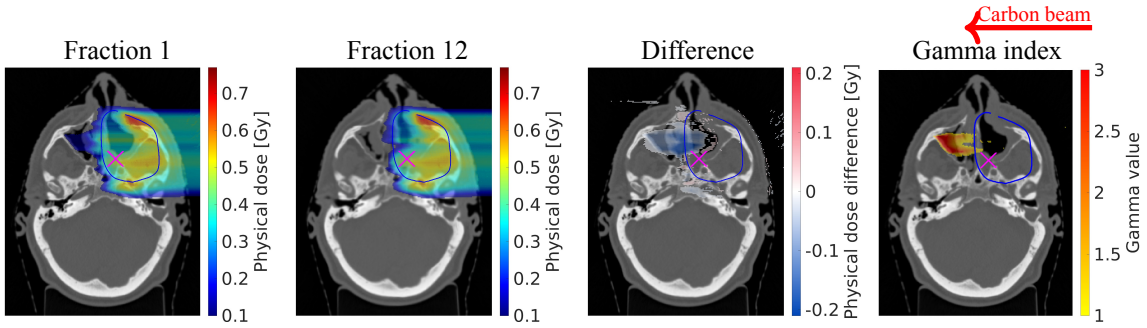

Figure 4.22. Simulated physical dose distributions corresponding to one fraction of the 0° treatment field from the simulation using the planning CT (fraction 1), the follow-up CT (fraction 14), and the absolute differences between these two simulations (difference). The fourth plot presents the Gamma index analysis. The data is overlaid on axial CT slices at 26.00 mm relative to the isocenter, except in the second column, where the follow-up CT is used. The CT and dose data voxel size is (0.6x0.6x1.0) mm^3.

In summary, a significant anatomical change was observed due to the filling of the maxillary sinus cavities, resulting in an increase of approximately $1.55\,cm^3$ in the PTV volume within the studied 5 mm axial region (Figure 4.19). The filling in the left maxillary sinus extended toward the distal end of the PTV, placing the change in a deep-seated location from the perspective of the detectors. This anatomical modification led to a slight underdosage in the distal PTV region, as shown in the simulated dose distribution (Figure 4.22). The gamma index pass rate was 98.85%, with the largest discrepancy observed in a hotspot outside the PTV.

Although an increased signal was visible in the reconstructed FV distribution at the site of the cavity filling, the signal was not conclusive, despite the anatomical change being well-localized and relatively large. Comparison with the true FV distribution (Figure 4.20) underscores the inherent limitations of detecting changes at the distal edge of the PTV. This is due to both the reduced production and lower energy of secondary fragments in deeper regions, which diminishes their likelihood of reaching the detector.

4.2 Clinical Trial Patients from the InViMo Monitoring Study

The second part of the results chapter presents data from two patients enrolled in the InViMo clinical trial. This is unique, as it represents the first comprehensive documentation combining anatomical changes based on HU differences from CT images (considered the ground truth), measured data acquired during patient monitoring, and corresponding simulation results. A comparison between measurements and simulations is provided for the reconstructed fragmentation vertices (FV), obtained by back-projecting fragment crossing points in the detectors toward the patient. Simulations were performed using follow-up CTs and compared with measurements acquired on the closest possible days. The measured data were obtained with the clinical detection system, while the simulated data were generated using the developed FLUKA CIRT monitoring workflow (Section 3.2.4) in this work, as described in the Materials and Methods.

True FV from the simulations are also included to aid in interpreting key signals in ion treatment monitoring with charged nuclear fragments. Additionally, the results of the Kolmogorov-Smirnov (KS) test, which compares distributions and identifies statistically significant differences in fragment distributions, are presented. For the FV data, the analysis was performed within (5×5) mm regions along the x-axis (perpendicular to the axial plotting slice). The blue contour in the CT slices outlines the PTV, and the cross marker represents the projection of the isocenter onto the axial plane (perpendicular to the axial plane).

4.2.1 Patient 6

The following patient, diagnosed with adenoid cystic carcinoma, was treated with CIRT using a two-beam treatment plan at HIT and was part of the InViMo clinical trial. The monitored treatment angle was $180°$, and the monitored fractions were 8, 9, and 15. The simulations were performed using a follow-up CT acquired on the day of 7 days before the first monitored fraction (fraction 8) and a second follow-up CT obtained 2 days before the last monitored fraction (fraction 15).

Patient 6: CT anatomical changes

Figure 4.23 illustrates the HU differences, with a plotting threshold of 600 HU, representing anatomical differences between two follow-up CT taken 13 days apart. For this patient, three anatomical regions of interest were identified. Region 1, located at the nasal cavity level, spans axial positions from 28.39 mm to 38.39 mm, extending toward the distal end of the PTV. This region highlights nasal sinus-filling or swelling, with an estimated volume of 3.91 cm^3. In the second region, a skin fold observed at the level of the right infraorbital region (under-eye area) is depicted across 3 mm, covering slices from 13.39 mm to 15.39 mm axially. In region 3, changes observed mainly due to metal artifacts in the mandibular (lower jaw) region caused by dental implants, and differences in the tongue, are depicted within three slices spanning a 15 mm axial region from -0.61 mm to 9.39 mm.The total voxel-by-voxel differences within the contoured PTV, shown as the blue contour in Figure 4.23,

amounted to $1.09\,\mathrm{cm}^3$.

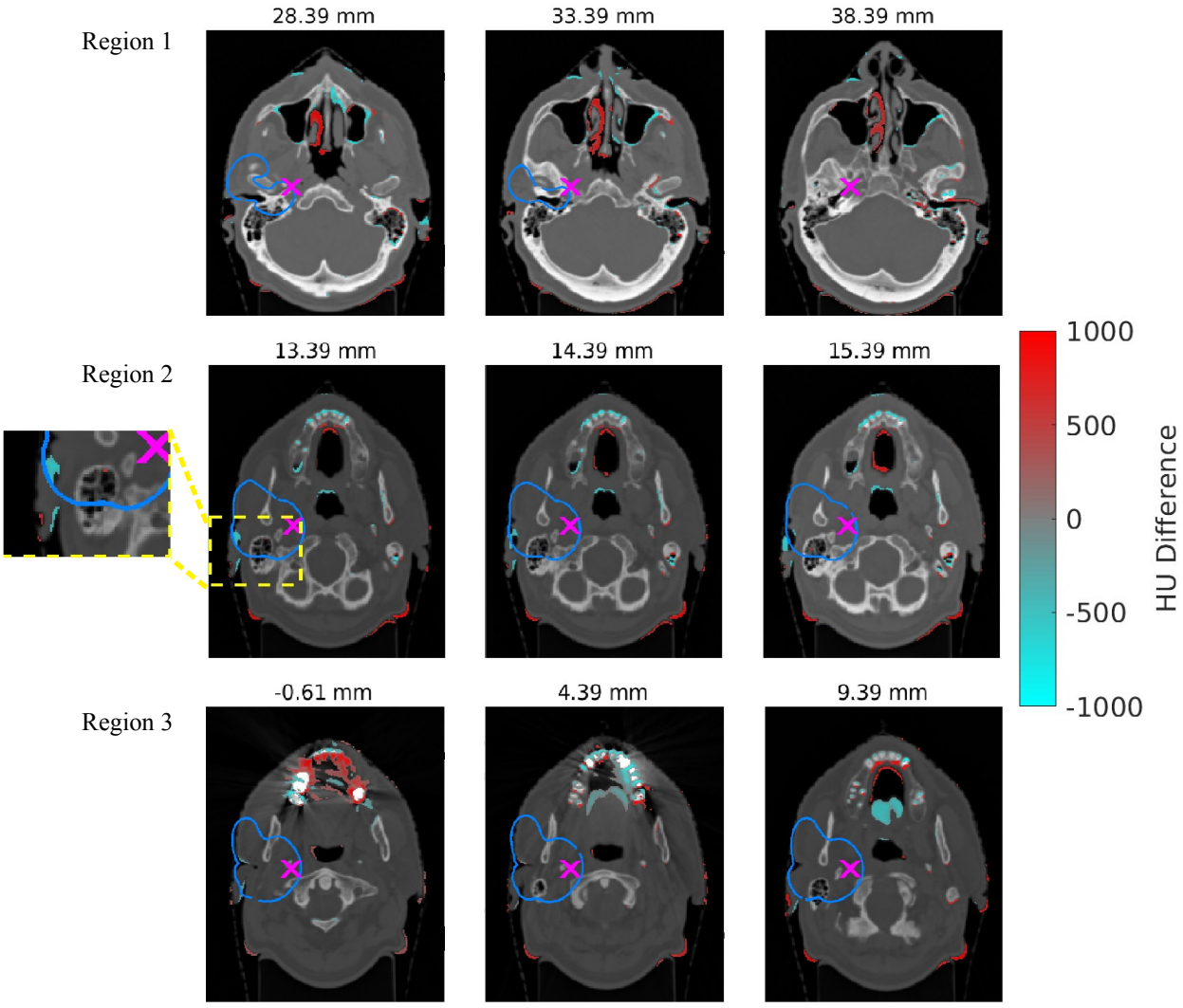

Figure 4.23. Anatomical changes between two follow-up CTs, taken 13 days apart, based on HU differences. The HU differences represent voxel-by-voxel comparisons, with the CT voxel dimensions being $(0.6 \times 0.6 \times 1.0)\,\mathrm{mm}^3$. These changes are superimposed on the first follow-up CT. Three regions are shown in total, and the slice positions, relative to the isocenter, are indicated above each image. Per region three images correspond to axial CT slices spaced 5 mm apart, representing the patient's anatomy and changes over a 10 mm span. Slice positions relative to the isocenter are indicated above each image.

Patient 6: Measured reconstructed FV and simulated reconstructed and true FV

Figure 4.24 presents a comparison of measured and simulated FVs. The distribution of reconstructed fragment vertices was obtained from clinical patient monitoring measurements during fractions 8 and 15, and the distribution of reconstructed fragments from simulations was performed using the same treatment plan. The relative differences between the measurements are considered not significant and are dispersed throughout the CT. However, the statistical significance test indicates a relatively strong signature around the right ear. The simulation shows a significant pattern, which is consistent with the measured data, although

it appears stronger in the simulation. Interestingly, the simulation yields a higher number of reconstructed fragmentation vertices compared to the measurements.

In the third row of Figure 4.24, the results of the true FV of the detected fragments are displayed. The fragments are primarily concentrated at the beam entry region within the PTV while the signal is stronger than for the reconstructed FV. The difference plot highlights various zones of change, including near the skin fold along the beam path, the oral cavity, and the skin on the left cheek. The KS statistical test confirms the three distinct regions of change: the first within the PTV, the second in the central part of the head near the nasal cavity, and the third between the oral cavity and the left cheek. The last two are not directly relevant to the monitored field, but might be relevant for the other treatment field of the patient ($215°$).

In summary, the superficial location of the PTV relative to the beam entrance, around the ear region, places it at a considerable depth from the perspective of the detector (Figure 4.23). A pronounced anatomical change was observed in the right nasal cavity, which lies outside the PTV and is therefore not directly targeted by the treatment beam.

The measured reconstructed FV distribution showed a slight increase in signal, though this alone was insufficient for a conclusive interpretation. However, the KS statistical test identified a significant signal in the region of the ear canal. The simulated, reconstructed and true FV distributions showed good agreement with each other, particularly within the PTV. Furthermore, the measured signal increase aligned with the expected region, especially near the ear canal (Figure 4.24).

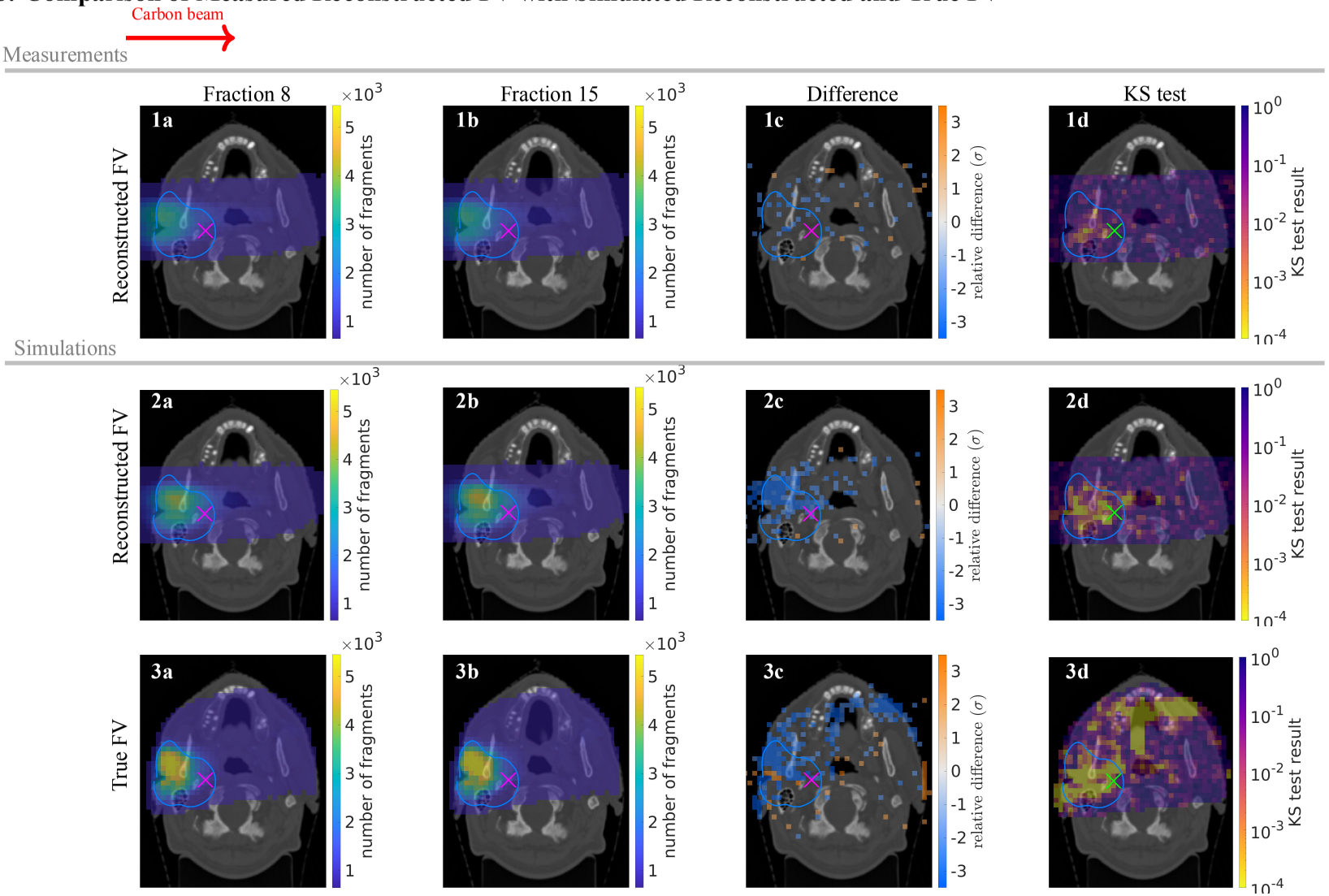

Figure 4.24. Measured and simulated reconstructed FV are shown in the first and second rows, while the true FV of the detected fragments is presented in the third row. The distributions are overlaid on the isocenter axial slice of forts follow-up CT, except for fraction 15, which is overlaid onto the second follow-up CT in column (b). Column (c) shows the differences between the two distributions. The voxel data size for the fragmentation distributions and differences is $(5.0 \times 5.0 \times 5.0)\,\mathrm{mm}^3$. The fourth column (**d**) presents the p-values from the Kolmogorov-Smirnov (KS) test, calculated within each 5×5 mm voxel region based on the data distribution along the x-axis (perpendicular to the axial plotting slice).

4.2.2 Patient 7

The patient, treated at HIT for a clivus chordoma, was monitored during fractions 6, 10, 13, and 15 as part of the prospective InViMo clinical trial. Two follow-up CTs were acquired for this patient, coinciding with the measurement days corresponding to fractions 10 and 13. These CTs were subsequently used in the simulations. The monitored treatment angle was $5°$.

Patient 7: CT anatomical changes

Figure 4.25 highlights HU differences by comparing the two follow-up CTs. A plotting threshold of 600 HU was applied to emphasize anatomical variations between the two scans. Small differences are observed outside the PTV, particularly in the tissue near the tip of the nose and around the right zygomatic bone. Inside the PTV, differences were detected within the nasal cavity and the nasopharynx region. The volumetric change within the PTV was estimated to be $1.76\,\mathrm{cm}^3$, with the total PTV volume being $78.88\,\mathrm{cm}^3$. The zoomed region in the axial slice in $-17\,\mathrm{mm}$, a mucus or swelling is observed in the border of the PTV.

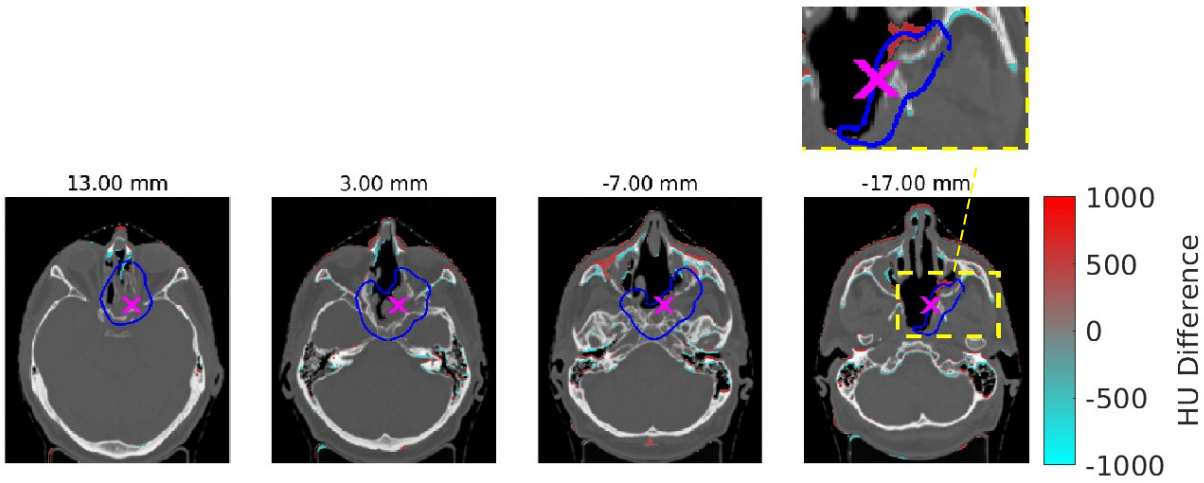

Figure 4.25. Anatomical changes between the two follow-up CTs, taken 2 days apart, are visualized based on HU differences. These changes are overlaid on the first follow-up CT. The four images correspond to axial CT slices, depicting anatomical variations over a 30 mm span. Slice positions relative to the isocenter are indicated above each image.

Patient 7: Measured reconstructed FV and simulated reconstructed and true FV

In the case of Figure 4.26, the reconstructed FV distributions from simulations using the follow-up CTs taken on the same day as the measurements are presented. The reconstructed FV distributions exhibit a similar pattern having more recostructed FV detected in the simulation. In the differential plots for the reconstructed FV (plots 1c and 2c), the signal appears dispersed, particularly in the simulation. In the measurement, a reduction in the relative differences is visible in the beam entrance region, whereas in the simulation some activity is also present in this area.

The p-values from the Kolmogorov-Smirnov (KS) test for the measured reconstructed FV (plot 1d) are not conclusive within the PTV, although some areas show localized significance. Outside the PTV, an intense signal (highlighted in yellow) is observed at the crest between the left zygomatic bone and the lower maxillary bone, which is absent in the simulation (plot 2d). In the KS test for the simulated reconstructed FV (plot 2d), the most significant signal originates from the nasal region.

The signals observed in the difference plots at the beam entrance and the highlighted regions in the p-values for the measured reconstructed FV could suggest patient misalignments between the monitored fractions.

For the true FV in Figure 4.26, an increase in fragments is observed in the difference plot (plot 3c) in the left cheek and along the nasal cavity walls. The signal observed in the right cheek, corresponding to the beam entrance, suggests that the signal seen at the same location in the measurement difference plot (plot 1c) cannot be conclusively attributed to a patient shift. Since no patient shift was included in the simulation, the signal observed in the difference plot (plot 3c) is more plausibly attributed to skin deformation due to the patient mask or to anatomical changes in the skin, such as swelling of the patient tissue.

The KS test, calculated within each 5×5 mm voxel region based on the data distribution along the x-axis (perpendicular to the axial plotting slice), is presented in plot 3d. In this plot, the bottom region of the nasal cavity at the PTV border exhibits a significant signal, corroborating the observations from the difference plot (plot 3c). Additionally, in the KS test for the true FV (plot 3d), a highlighted significant signal is visible in the left cheek at the level of the zygomatic bone. This could be correlated with the signal observed in the KS test of the measured reconstructed FV (plot 1d), with the slight differences in localization likely due to multiple Coulomb scattering (MCS) and uncertainties inherent to the backprojection method.

In summary, although only minor anatomical changes were visible in single CT slices, these changes extended over approximately 18 mm along the axial direction (Figure 4.25). In the measured reconstructed FV distributions, the KS test did not reveal significant signals inside the PTV, but did indicate notable changes originating from outside the PTV.

In the simulated reconstructed FV, the KS test showed only a minor signal in the anatomical region at the bottom of the nasal cavity. In contrast, the true fragmentation vertex distribution from the simulation was the only one that showed statistically significant differences in the same anatomical region as the HU-based changes, confirming the measurement observations (Figure 4.26).

Patient 7: Comparison of Measured Reconstructed FV with Simulated Reconstructed and True FV

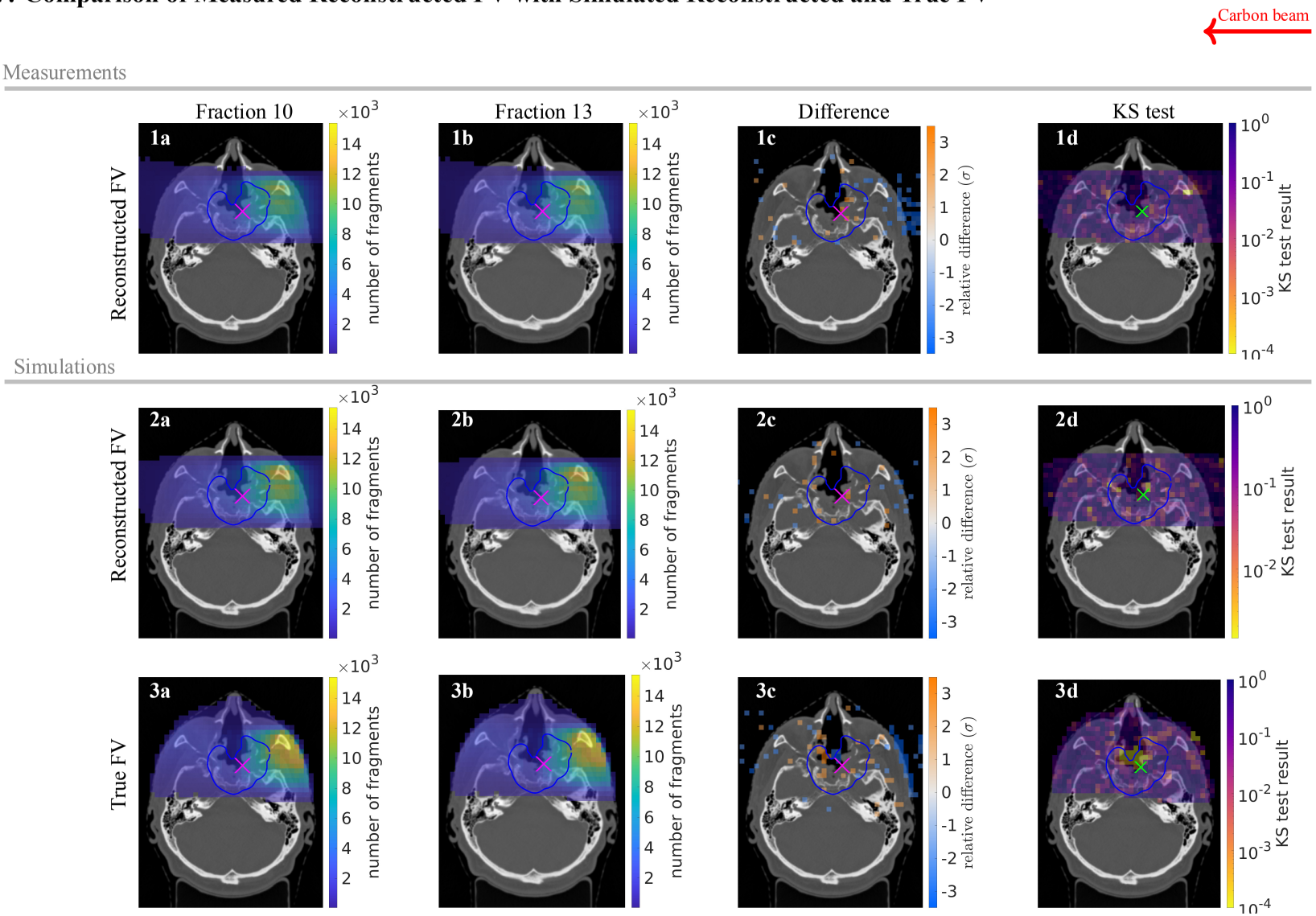

Figure 4.26. In the first and second rows, the measured and simulated reconstructed FV distributions are presented, while the third row displays the true FV of the detected fragments. The distributions are overlaid on the isocenter axial slice of the first follow-up CT, except for fraction 13, which is overlaid onto the second follow-up CT in column (b). Column (c) illustrates the differences between the two distributions, with a voxel data size of $(5.0 \times 5.0 \times 5.0)\,\mathrm{mm}^3$. Column (d) presents the p-values from the Kolmogorov-Smirnov (KS) test, calculated within each 5×5 mm voxel region based on the data distribution along the x-axis, perpendicular to the axial plotting slice.

4.3 Prostate Cancer Case Study and Design of a New Detector Configuration

The InViMo clinical system was designed and tailored to monitor head and neck patients as part of the prospective clinical trial at HIT. However, other pathologies, such as prostate cancer, could also benefit from this monitoring.

Prostate patient: CT Anatomical differences

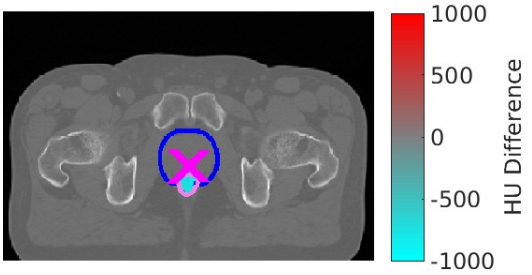

Figure 4.27. Anatomical differences in the rectum represented as HU differences overlaid on an isocentric axial slice of the CT. The HU differences correspond to voxel-by-voxel comparisons, with CT voxel dimensions of $(0.9 \times 0.9 \times 3.0)\,\mathrm{mm}^3$. The PTV is outlined in blue, while the rectum is contoured in pink. The isocenter is marked with an "x".

To monitor a CIRT treatment in a prostate patient, a planning CT was modified to emulate rectal emptying. For this, a volume of $14.0\,\mathrm{cm}^3$ was altered by changing the HU values in the rectal cavity to air-equivalent HU. Figure 4.27 shows the HU differences between the planning CT and the modified CT. The volumetric change in the PTV region was estimated to be $6.05\,\mathrm{cm}^3$.

Prostate patient: Simulated physical dose

The prostate patient was treated at HIT with protons, and for this thesis, a CIRT treatment plan was created. One fraction with the $0°$ treatment field of CIRT was simulated. Figure 4.28 shows the physical dose, the absolute differences, and the results of the gamma index analysis. The values correspond to voxel sizes of $(0.9 \times 0.9 \times 3.0)\,\mathrm{mm}^3$ in the isocenter axial plane on the planning CT slice, except for the modified CT, where the data are superimposed on the HU-modified planning CT. The plot visualization threshold is $0.1\,\mathrm{Gy}$ for dose and 5% for dose difference. The latter is a commonly used dose difference threshold at HIT for evaluating treatment plan quality. Differences of approximately $0.2\,\mathrm{Gy}$ are observed in the right pelvic floor. The fourth plot provides a gamma index analysis to evaluate the agreement between the dose distributions of the planning and modified CT. The gamma index analysis in this study was performed using a 3%/3 mm criterion with global dose normalization, as described in 3. The overall pass rate was 99.38%.

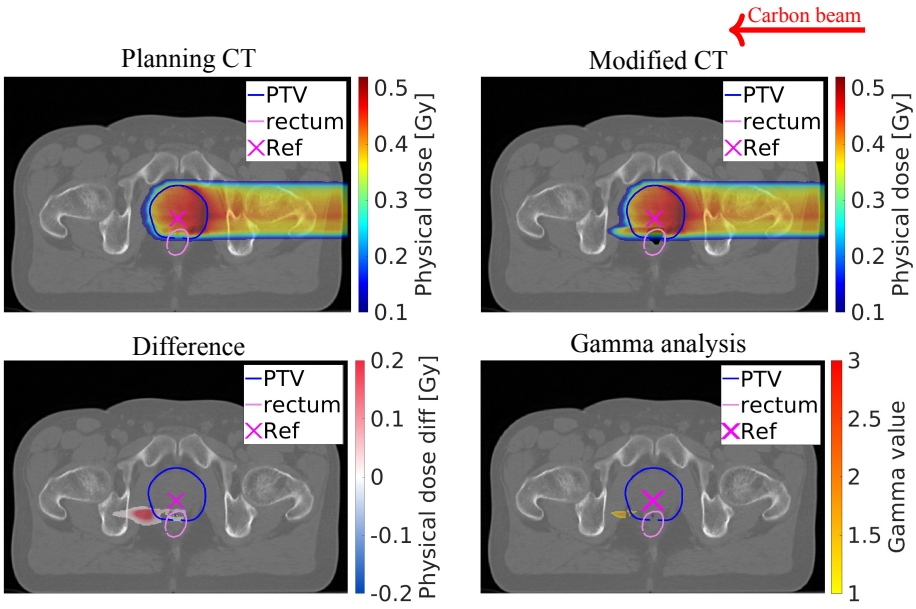

Figure 4.28. Simulated physical dose distributions corresponding to the $0°$ treatment field for one fraction. The simulation results using the planning CT and a modified CT are shown. The third plot illustrates the absolute differences between the two simulations, and the fourth presents the results of the Gamma index analysis. The data is overlaid on the axial isocenter planning CT slices, except for the modified CT. Both CT and dose data have a voxel size of $(0.9 \times 0.9 \times 3.0)\,\mathrm{mm}^3$.

Prostate patient 5: Heavy Ion Nuclear Interactions (HINI)

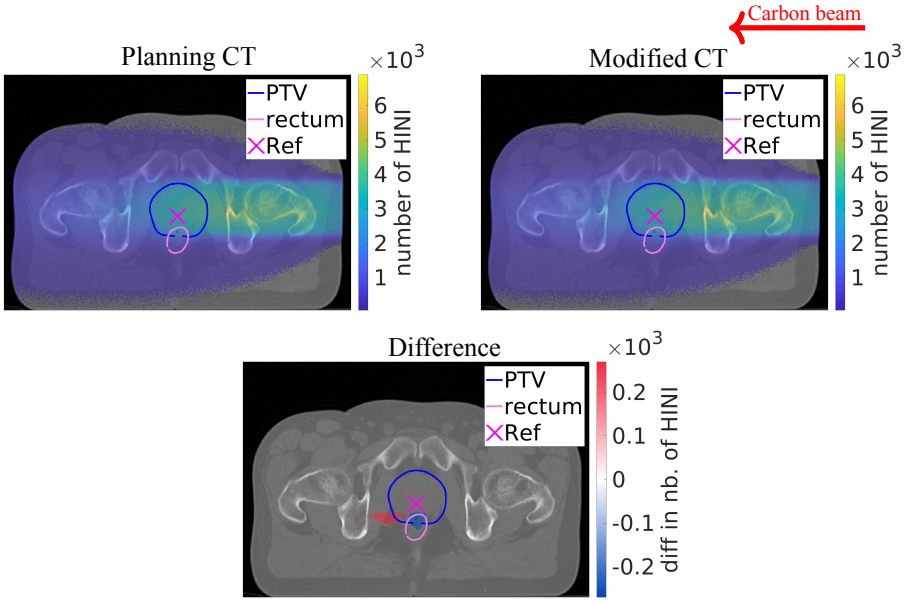

Figure 4.29. Heavy Ion Nuclear Interactions (HINIs) from the simulation using the planning and modified CT. The data voxel size is $(0.9\text{x}0.9\text{x}3.0)\,\mathrm{mm}^3$ and is overlaid on axial CT slices at the isocenter.

Prostate patient: Fragmentation vertices

Figure 4.30, rows **1** and **2**, present the reconstructed and true FV, respectively, for the fragments detected by the InViMo monitoring system. The isocenter of this treatment plan was shifted 8 cm superior to the original isocenter to keep a safe distance between the patient and the detectors. As described in the Materials and Methods section, this shift was estimated to enable CIRT monitoring for an average-sized adult male. In plot 1c, the differences in the number of reconstructed FV are not significant or conclusive to establish the mimicked anatomical changes in the patient. Also, the KS analysis along the $(5\times5\times200)$ mm^3 stickxel distribution does not show evidence of anatomical changes.

When evaluating differences using a threshold plot at 2σ, as shown in plot 2c, the true FV appears widely dispersed, with a small cluster around the rectal-emptying region. Since the same CT was used for both simulations and the only change was made in the rectal region, this image demonstrated the localized impact of the rectal-emptying simulation. The KS analysis for the true FV in plot 2d confirms visible anatomical changes. Plot 1a shows the long path fragments generated in the rectum must travel. This increases the likelihood of stopping and scattering along their path. This led to a weaker and more diffuse signal.

To overcome these challenges, an in-table detection system was designed within this thesis using the developed FLUKA Monte Carlo framework, as described in the Materials and Methods section 3.2.3. The reconstructed and true FV for this system are depicted in rows **3** and **4** in Figure 4.30, respectively. The isocenter was preserved inside the PTV as established in the treatment plan. While more fragments were detected in the entrance region of the beam with the Invimo system, a higher number of fragments in the rectal region are detected with the new in-table system, as observed in columns **a** and **b**. The reconstructed FV differences in plot 3c show a reduction in fragment production in the rectal region, consistent with the modification made to the CT to emulate rectal emptying. The statistical test, in plot 3d, shows a high signal in the modified rectum filling.

In the true FV depicted in row **4**, the paths of the detected fragments toward the table are illustrated. Differences in terms of σ reveal a reduction in detected fragments in the anterior part of the PTV and rectum. This result aligns with the KS signal, highlighting the anatomical change in the rectal region, which is prominently reflected in the p-values of this statistical test.

In Summary, changes in intestinal filling or emptying are a common challenge when treating tumors in the lower abdomen and pelvis, particularly in prostate cancer treatments. The newly designed in-table detection system outperforms the InViMo system for this tumor location, as anticipated. The standard InViMo configuration, optimized for skull-based tumors, shows limited sensitivity to anatomical changes occurring deeper in the body, such as rectal filling variations. By contrast, the in-table configuration, preserving the isocenter inside the PTV and detecting fragments along shorter paths, enabled better localization and detection of rectal changes. The promise of optimizing detector positioning for future clinical studies beyond InViMo, expanding monitoring capabilities to other tumor sites in the body.

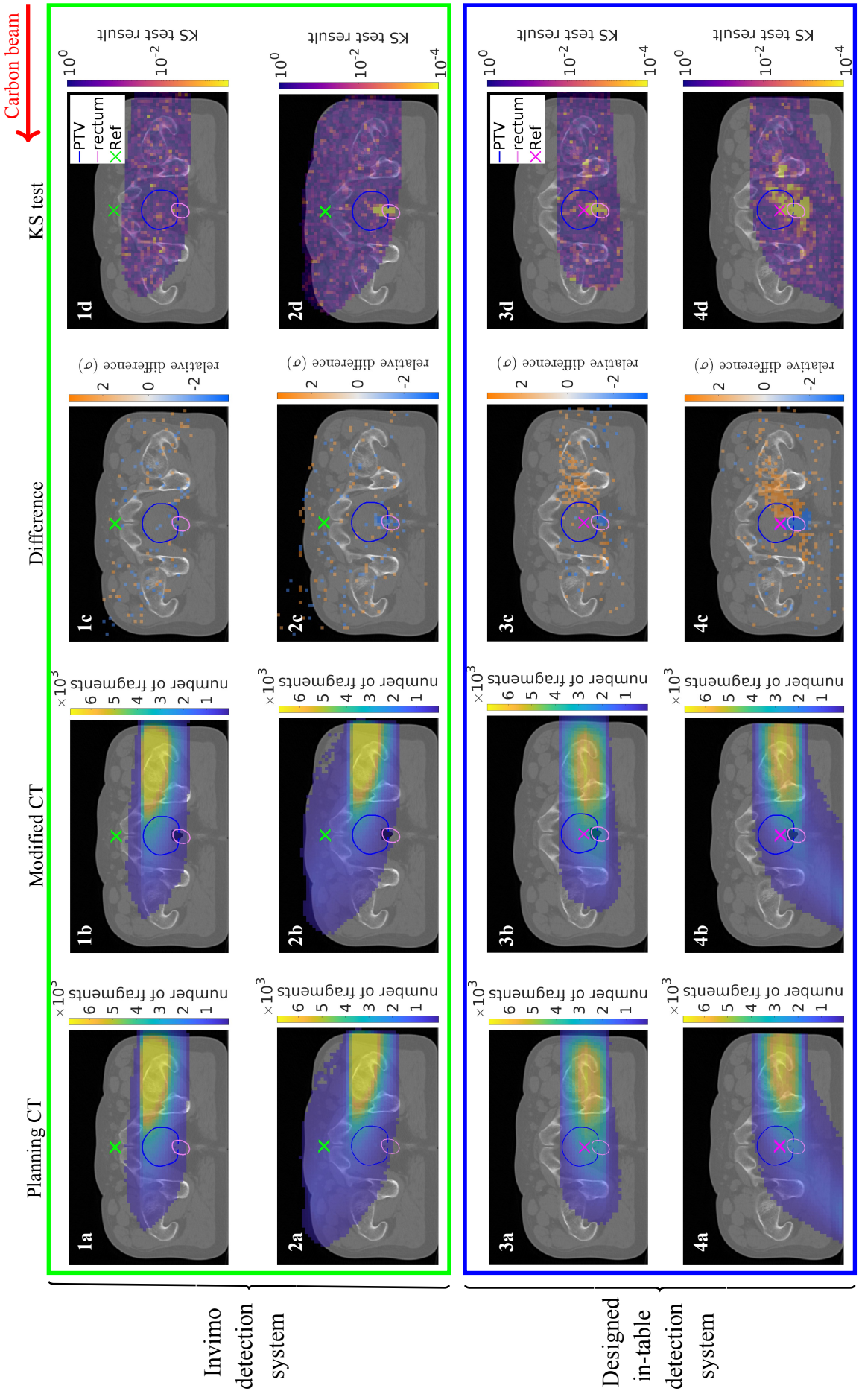

Figure 4.30. Distributions of reconstructed (row **1**) and true fragmentation vertices (row **2**) for the Invimo detection system (green box), and reconstructed (row **3**) and true vertices (row **4**) for the in-table detection system (blue box). Column (**a**) presents the simulation using the planning CT, column (**b**) the modified CT, and column (**c**) shows the differences. The voxel size for fragmentation distributions and differences is $(5.0 \times 5.0 \times 5.0)$ mm^3. Column (**d**) presents p-values from the Kolmogorov-Smirnov (KS) test, calculated within each 5×5 mm voxel region along the x-axis. Data is overlaid on axial CT slices at the isocenter, except for column (**b**), where the modified CT slice is used.

Chapter 5

Discussion

The primary objective of this PhD project was to develop a Monte Carlo (MC) simulation framework for the monitoring of carbon ion radiotherapy (CIRT) through the detection of charged nuclear fragments using AdvaPIX TPX3 Quad detectors.

As a first step, this framework was established by integrating the detector's geometry and scoring mechanisms into FLUKA MC. Subsequently, it was coupled with the FLUKA-based Heidelberg Ion-Beam Therapy Center (HIT) beamline model for dose calculation. The framework was benchmarked and validated against experimental data using a single mini-tracker. Although the FLUKA Monte Carlo code is widely validated for carbon ion radiotherapy applications, and the HIT beamline model implemented in FLUKA has been extensively benchmarked, inherent uncertainties persist in Monte Carlo-based modeling. These uncertainties primarily arise from limitations in hadronic interaction models, inaccuracies in nuclear cross-section data, and the modeling of secondary fragment production, all of which introduce systematic uncertainties. These limitations are partly due to the phenomenological nature of nuclear fragmentation models, which rely on empirical fits to experimental data rather than fundamental theoretical principles. Statistical fluctuations inherent to particle interactions, such as scattering and stopping, are regarded as accurately modeled given their direct impact on the dose distribution. The result of the validation demonstrated a residual difference between the simulation and the experimental measurements of less than 4% in the number of detected fragments [22]. This excellent agreement confirms the reliability of the framework developed.

Building on this foundation, an extended version of the framework was developed, incorporating seven mini-trackers that constitute the clinical detection system designed by my research group. This extended framework was integrated with the FLUKA-based MC framework FICTION (FLUKA Integrated Framework for CT-based calculations in Ion Therapy), developed at HIT. This integration enables simulations of CIRT monitoring for patients treated at HIT.

Previous studies using homogeneous and anthropomorphic phantoms have provided valuable insights into the interpretation of fragment distributions and their signatures. However, given the inherent complexity of these distributions, this thesis discussion will focus on describing and interpreting signals based on the output of CIRT monitoring simulations of patients treated at HIT. The signature analysis of the reconstructed fragmentation vertices

(FV) was performed by tracing secondary fragments and subsequently back-projecting their trajectories onto the patient anatomy. A major advantage of the MC simulation is the access to more fundamental quantities, including true fragmentation vertices (true FV), hadronic inelastic and non-elastic interactions (HINI), and dose distributions. To correlate the reconstructed FV distributions with ground truth, anatomical differences between two CT scans, representing two treatment days for each patient, were compared. This approach aims to provide a deeper understanding of what is observed in CIRT monitoring and how interfractional anatomical changes influence the FV distribution formation and characteristics.

However, it is important to note that this is not a systematic study on detectability limits or sensitivity thresholds. Instead, the analysis is based solely on patient simulation results presented in this thesis and two detection system configurations, one being the clinically used detection system in the InViMo clinical trial and the other an in-table-based configuration developed within the scope of this thesis.

How close are we to the true vertex? Spatial and geometric considerations in FV reconstruction

The reconstructed FV represents an approximation of the true FV. The reconstructed FV is subject to energy-dependent scattering effects (MCS), fragment loss due to stopping in the patient, and the spatial configuration of the detection system, all of which contribute to a broader spatial distribution of the reconstructed FV compared to the true FV.

The impact of fragmentation depth and fragment scattering on FV reconstruction

The effects and dependencies of these factors manifest in distinct patterns. When comparing the true FV distributions with the reconstructed FV distributions, a blurring effect becomes evident as seen, for instance, in the first patient (Patient 1 in Figures 4.3). Due to the angular cross-section dependency on the energy, this effect is particularly pronounced for lower-energy fragments, which experience significant angular spread while propagating through tissue, leading to a broader detected track distribution. An example of this can be observed in Region 2 of Patient 3, where the back-projected FV (Figure 4.11) shows a more diffuse distribution compared to the true FV origin (Figure 4.12). However, it is important to note that this blurring is not solely attributable to the energy dependency of the fragments. Other contributing factors, such as the generation of higher-order (tertiary) fragments and the limitations of the track reconstruction algorithm, can also lead to signal broadening.

Fragments generated in deeper tissue layers (in the direction of the beam) are more likely to be higher-generation fragments, resulting from multiple sequential nuclear interactions. As a consequence, these fragments tend to have a reduced mass, making them more susceptible to scattering. This can be observed when comparing the back-projected and true FV (Figure 4.20) with the HINIs (Figure 4.21) in Patient 5, particularly in the medial facial region beneath the left infiltrated cavity. Additionally, as shown in Patient 4 on the right side of the nasal cavity in Figure 4.16, the deeper the fragmentation origin, the more pronounced the scattering effect, further broadening the reconstructed FV distributions.

Moreover, the more tissue the fragment has to cross on its way to the detector, the higher

the scatter and probability of absorption, which poses challenges in detecting anatomical changes, particularly in deeper regions, as seen in FV distribution on Patient 4 in Figure 4.16. This results in an overall reduction in the number of detected fragments, as evidenced in the FV distributions of Patient 6, Figure 4.24, where there is an approximate 25% decrease in detected fragments compared to their true origins.

Detector configuration and its influence on signal detection

The shape and spatial resolution of the distribution of reconstructed FV are also influenced by the relative position of the detection system to the patient isocenter, as well as the placement of each individual mini-tracker within the detection system. The fragments have a strongly forward-peaked angular track distribution, meaning that signal intensity decreases exponentially with the observation angle relative to the pencil beam position [87].

This phenomenon is also evident in the simulated prostate patient. In Figure 4.30, the distributions of reconstructed FV (rows 1 and 3) and true FV (rows 2 and 4) for simulations performed with both the clinical detection system and the suggested in-table detection system are presented. The reconstructed FV distributions differ depending on the detector position, as seen in plots 1b and 3b. The track paths toward the detector are more evident in the true FV (plots 2b and 4b). Plots in columns c and d illustrate how detectability changes with detector positioning.

Considerations for in-table detection

Configuring detection systems specifically tailored to the anatomical region of interest is crucial for effective treatment monitoring. Our research group addressed this need by developing a clinical detection system optimized for the InViMo clinical trial, as reported in [14,20]. This system, designed for CIRT monitoring in the head and neck region, utilizes seven tracking modules. Monitoring other tumor locations motivated the exploration of the in-table detection system, particularly for irradiation in regions closer to the treatment table in the torso and pelvis.

Considering that CIRT facilities, such as those in Japan [88, 89], treat a wide range of tumor locations and types with carbon ions, including head and neck malignancies, lung cancers, gastrointestinal tumors, prostate and genitourinary cancers, sarcomas, and pediatric cancers, there is a clear need for flexible and adaptable monitoring solutions. Due to the more frequent treatment of tumors located in the lower abdomen and pelvis, as exemplified by the prostate patient studied in this thesis, the relevance of adapting the detection system configuration becomes evident.

As mentioned in the in-table CIRT monitoring prototype (Section 3.2.3), the in-table approach designed in this thesis was conducted as an exploratory study to find out if other geometries can improve the sensitivity of the reconstructed FV distribution to realistic anatomical change. Systematic studies, such as the impact of table attenuation on detected fragments and the detector's performance, still need to be conducted to gain a more comprehensive rationale for an in-table system. Subsequently, technical aspects, such as cabling, cooling, data collection, and system integration, have to be engineered.

One key aspect before treatment delivery is coplanar X-ray imaging to secure the patient's position on the treatment table (see Figure 3.4). An in-table system must not interfere with this process. Therefore, a modular or retractable detection system that can be inserted into the treatment table between X-ray verification and treatment delivery would be a viable solution.

Spatial resolution and uncertainty in FV reconstruction

Among the effects previously described, spatial resolution also plays a role in broadening the reconstructed signals, particularly depending on the depth at which the fragments are generated. At greater depths, it might happen that signal overlap increases to the extent that individual contributions from more geometrical changes within a patient become indistinguishable. For example, in Patient 2, at the beam entrance near the zygomatic bone, a signal is observed in the air region in the reconstructed FV, while it is not visible in the true FV, as depicted in the fragmentation vertices distributions in Figure 4.7. This discrepancy demonstrated the influence of resolution on signal interpretation, where limited spatial resolution can lead to misattributions of fragment origins.

Regarding the spatial configuration of the detectors, the position of each mini-tracker also affects the spatial resolution of the reconstructed FV. In the publication regarding the development and evaluation of the in-vivo treatment monitoring system [20], we found that mini-trackers (see detector configuration in Figure 3.2) positioned at wider angles (e.g., $36°$) achieve better spatial resolution along the z-axis (approximately 3 mm) compared to smaller angles (e.g., $20°$), which result in lower spatial resolutions of approximately 5 mm. As a result, the average spatial resolution of 4 mm along the beam axis is achieved for the entered detection system, considering all mini-trackers collectively without discretizing their individual signals. It should be noted that these spatial resolution values refer to the geometric reconstruction precision for this particular detector spatial configuration. It excludes the effect of the MCS-related contributions, which were minimized by using a thin PMMA plane as a target.

Optimization strategies for FV reconstruction

One source of uncertainty in fragmentation vertex reconstruction is the back-projection method of the measured fragment tracks itself. While it has been shown to be a suitable approach [90], particularly for longitudinal accuracy along the beam axis, it remains a potential room to further improvements. The closest-distance back-projection method assumes that the detected fragment originates along the nominal pencil beam axis, which is a first approximation but does not fully account for the lateral dispersion of the primary ions around the actual pencil beam in the actual fragmentation depth and multiple Coulomb scattering (MCS) effects.

To address these limitations, optimization studies have been conducted to enhance reconstruction accuracy using a homogeneous PMMA phantom with the detector positioned at $z = 30°$ [91]. The optimized position of the reconstructed fragmentation vertex along the connecting line between the pencil beam and the detected fragment track was determined. A median optimized factor of 0.24 was found (instead of the current 0.5), improving the

reconstruction precision of the x-coordinate by $(19 \pm 3)\%$. However, the ideal factor varies significantly across different spatial regions and is dependent on both detector positioning and the lateral pencil beam position and energy. For this reason, a fixed factor of 0.5 was retained throughout this work for consistency. The developed MC framework is ideally suited to optimize this parameter, as it provides access to the fragmentation point information.

How to see the unseen? Signal interpretation in anatomical changes

Among all the possible internal changes in patients treated, cavity filling or emptying is one of the most clinically relevant, as it might have a significant impact on dose distribution. In head and neck treatments, mucosal swelling or sinus cavity filling variations can significantly alter the stopping power landscape, potentially impacting the dose delivery to the target and organs at risk. Similarly, the well-documented phenomenon of rectal emptying or filling in prostate treatments [92, 93] is an example of anatomical modifications that are highly probable during RT treatment, reinforcing their importance in FV signal interpretation.

The characteristic signature of cavity filling or emptying has been previously investigated using homogeneous [16, 17] and anthropomorphic head phantoms (CIRS 731-HN) in a realistic clinical scenario [18]. In the anthropomorphic head phantom study, a silicone insert was placed in the nasopharynx region to mimic tissue swelling. The findings from both simulation and measurement showed that a filling of the nasopharynx led to a significant reduction in detected FVs in the upstream of the filled-region due to the absorption of secondary fragments in the silicon insert and a reduction in fragment production beyond the modified region, caused by the range reduction of the primary carbon ions. These results demonstrate that FV imaging has the potential to detect clinically relevant under- or over-dosage. Additionally, the study highlighted that the observed fragmentation signal signature is highly dependent on the anatomical location of the density change, with shallower modifications being more easily detected than deeper ones.

Some of the patients studied and reported in this thesis also exhibit volumetric changes in cavity regions, as observed through anatomical differences from the CTs. An example is Patient 1, where the CT difference map (Figure 4.2) revealed changes within the nasal cavity, specifically an increase in tissue thickness along the nasal walls within the PTV.

In the reconstructed FV difference shown in Figure 4.3, plot 1c displays the expected signal cavity effect, with an increased signal near the left nasal wall corresponding to tissue increases in these areas, which enhance fragment production. This increase in tissue leads to a reduction in fragment detection posterior to the nasal region. This is due to both a reduced number of primary carbon ions reaching the posterior region, and to the absorption of fragments generated upstream, which may be attenuated by the swelling or filling and thus fail to reach the detector.

While the FV difference plots provide an idea of the type of anatomical change (such as a local increase or decrease in tissue density), the Kolmogorov-Smirnov (KS) test evaluates whether the observed differences are statistically significant. Although the KS test does not offer a definitive anatomical interpretation, it highlights regions with a higher probability of

change. In particular, plot 2d in Figure 4.3 reveals a statistically significant pattern extending across the nasal cavity, including the left infraorbital region and the beam entrance area, which will be discussed later.

As established in the earlier discussion, detector configuration influences signal detection and reconstructed signatures. A clear example of this is the prostate patient, which motivated the development of the in-table detection system. In this case, a clinically realistic cavity emptying event (rectal emptying) with a volume change of $14.0\,\mathrm{cm}^3$ was introduced in silico, as shown in Figure 4.27, with an impact on the PTV volumetric change estimated at $6.05\,\mathrm{cm}^3$. When comparing the reconstructed FV signal differences from the prostate patient using the clinical detection system (plot 1b) and the in-table system (plot 3c) in Figure 4.30, the cavity emptying signature is not visible in the clinical system but is clearly observed in the in-table system.

Apart from detector configuration, the origin fragments also influence the detectability of filled or empty cavities. This is evident when comparing anatomical changes in Figure 4.10 across all three axial regions in the same patient (Patient 3). The cavity filling effect is only visible in the reconstructed FV distributions in Figure 4.11, specifically in plot 2c, for the central axial region (Region 2, ranging from -2.00 to 2.00 mm). In contrast, in Region 3 (22.00 to 26.00 mm) at the level of the maxillary sinus, the reconstructed FV only shows a notable reduction in fragment signal in the posterior portion of the PTV and along its left side. However, when comparing with the HINI distribution in Figure 4.13, there is a slight reduction in production at the center of the infiltrated right maxillary sinus in Region 3 (plot 3c) compared to the cavity border in plot 2c. Interestingly, the true FV distribution in Figure 4.12 shows the cavity filling effect in all three regions, including the most caudal one at approximately $43.00 \pm 5\,\mathrm{mm}$.

Another example is visible in Patient 5, where an anatomical change in the left maxillary sinus, within the PTV, resulted in an estimated volumetric change of $1.55\,\mathrm{cm}^3$ (Figure 4.19). Neither the differences in the reconstructed FV nor the KS test indicate the cavity filling effect. In contrast, the observed anatomical alterations in Region 3 of Patient 3 are more pronounced, with an estimated volumetric change of $3.46\,\mathrm{cm}^3$ in the right maxillary sinus.

Beyond cavity filling, other anatomical modifications, such as patient shifts, skin deformations, and skin swelling, can also influence fragmentation signals. These variations, although not always directly associated with volumetric changes and neither in the PTV, may still impact the treatment outcome by altering the beam range. For the simulated patients, no deliberate shift in the CT position in FLUKA was induced. However, based on our experience, small skin deformations on the beam entrance, caused, for instance, by the fixation mask, could resemble patient mispositioning. Since the beam entrance is the farthest point from the detectors and generates high fragment production, fragments created there must traverse a significant amount of tissue before reaching the detectors. Consequently, the small skin deformations observed in Figures 4.2 and 4.6 for Patient 1 and Patient 2, respectively, are not detected in the reconstructed FV (Plots 1c in Figures 4.3 and 4.7).

To verify fragment generation within these small skin deformations seen in the CTs, as observed in the anatomical changes based on HU differences for Patient 1 in Figure 4.2 and for Patient 2 in Figure 4.6, we examined the HINIs for Patient 1 in Figure 4.4. A small region along the skin surface, toward the left ear, is visible, matching the findings in the true

FV in Figure 4.3, where the KS test in plot 2d highlights a significant change at the beam entrance, also appearing in the difference distribution in plot 2c. A similar effect is observed for Patient 2 in Figure 4.7, though with lower intensity.

Another skin deformation effect can sometimes be seen in the infraorbital region of patients. When this occurs contralateral to the beam entrance, it may interfere with fragment detection by causing fragment stopping or scattering. As this is a superficial anatomical change, it is more easily detectable. An example is a volumetric change of $0.19\,\mathrm{cm}^3$ in the left cheek of Patient 1, highlighted in the magnified inset in Figure 4.2. This patient also exhibited a cavity-filling event, which, despite being superficial, was not as easily concluded as discussed earlier in this section. However, the left cheek deformation produced signals in the reconstructed FV that would not have been conclusive without the supporting evidence from the CT, HINIs, and true FV in Figure 4.3.

For the monitored Patient 6, a possible skin fold is observed in Region 2, amplified in Figure 4.23, located near the right ear in the PTV. The measurement and simulation results align, showing a difference in the FV produced near this region, as evidenced by the p-values in the KS test in column d.

In parallel, we are developing a method to estimate patient shifts along the beam axis during treatment by aligning the rising slopes of the fragment emission profiles recorded across different fractions. These emission profiles represent histograms of the reconstructed FV along the beam axis, where the rising edge corresponds to the beam entrance region inside the patient. This feature serves as a reference point to evaluate positional consistency over multiple treatment sessions. However, this approach must be applied cautiously, as superficial anatomical changes, such as skin deformations, can mimic the effects of beam-axis shifts, potentially leading to misinterpretation.

Anatomical changes and their influence on fragmentation evaluation and delivered dose

Previous studies have investigated the localization and detectability of controlled anatomical changes, such as cylindrical air cavities in head-sized homogeneous phantoms using statistical metrics, including a custom-developed statistical measure called the D-value [16,17] and the KS test. While the limits of detectability have been crucial for evaluating the sensitivity of the method, a clinical perspective on dose effects had not been considered yet.

For the first time, we published a dosimetric assessment in a CIRT-monitored anthropomorphic head phantom (CIRS 731-HN) [76] with controlled anatomical modifications. A silicone insert of 6 g (approximately 6 mL) was introduced into the spherical PTV, which had a volume of 50 mL in the nasopharynx. This modification resulted in a clinically significant underdosage in the PTV, with 90% of the PTV receiving only 90% of the prescribed dose. The evaluation was performed in a clinically standard manner, based on the dose-volume histogram (DVH) computed for the entire 30-fraction, two-field treatment plan using RayStation [18].

A key question in the context of developing CIRT-adaptive methods based on secondary fragmentation monitoring: *Are the FV differences between fractions clinically relevant?*

Examining dose discrepancies between simulated fractions, the differences in dose dis-

tribution, and the regions where the gamma analysis criteria are not met, we observe notable findings in the axial regions studied. In Patient 2, an overdose is detected in the posterior part of the PTV, which is also indicated by the gamma analysis (Figure 4.9). However, the reconstructed FV signal does not clearly reflect the anatomical change of $0.60\,\mathrm{cm}^3$, likely due to its origin in a relatively deep or laterally located region—the nasal wall and mucus accumulation in the left maxillary sinus—which may lie beyond the detection sensitivity of the system.

Patient 4 also presents evidence of dose distribution discrepancies, as seen in Figure 4.18. The anatomical change in Patient 4 occurred in a deep tissue region, where fragments experience significant scattering and absorption before reaching the detector. Additionally, the angular geometry at such depths reduces the method's sensitivity, making these changes less detectable. Consequently, this change is not visible in the back-projected signal (Figure 4.16). In Patient 5, dose discrepancies are observed in the right maxillary sinus, where an underdosage is also reflected in the gamma index analysis. While a recognizable signal appears in the reconstructed FV, it does not provide a definitive conclusion regarding the anatomical change.

It is important to note that this analysis solely reports dosimetric discrepancies without discussing the potential clinical consequences of these changes. Based on the gamma analysis, no significant discrepancies in dose distribution were observed for Patient 1, as shown in Figure 4.5. In all other patients except Patient 2, the discrepancies were attributed to underdosage: for Patient 3 in Region 3 (Figure 4.14, plots 3c and 3d) within the PTV, for Patient 4 in the temporal lobe (Figure 4.18), and for Patient 5 in a air cavities (Figure 4.22). In contrast, Patient 2 exhibited a local overdosage within a cavity, as presented in Figure 4.9.

Moreover, carbon ion therapy delivers more precise dose distributions with sharper dose gradients. In such high-gradient regions, applying stricter gamma index criteria—such as $2\%/1\,\mathrm{mm}$-may be more appropriate for capturing clinically meaningful deviations.

Therefore, the final assessment of the clinical significance of these dosimetric findings lies with the expert judgment of clinicians and radiation oncologists, who are supported by dose-volume histogram (DVH) analyses and treatment planning tools. Furthermore, radiation oncologists consider various factors, including regions of over- or underdosage and their impact on critical structures. For example, in head and neck treatments, anatomical changes that reduce dose coverage to the target volume may necessitate intervention, especially if a radiosensitive organ, such as the optic nerve, is at risk of exceeding tolerance thresholds. The decision to adapt a treatment plan also depends on the number of remaining fractions; significant deviations early in the treatment course may prompt modifications, whereas minor changes later may not require adjustments.

Perspectives

The results presented in this thesis demonstrate the potential of the developed MC framework for charged fragment tracking to monitor anatomical changes in carbon ion radiotherapy. Further investigation is required to advance the framework toward clinical translation, with the goal of enabling simulation-based single-fraction monitoring using the planning

CT as the baseline for FV distribution analysis.

Every day, we are gaining more expertise in FV signal interpretation thanks to the growing number of patients enrolled in the InViMo clinical trial. Each new patient case, simulated with our developed Monte Carlo framework, provides valuable insights and allows us to refine our understanding of fragmentation signatures in real clinical scenarios. Moreover, the flexibility of the developed simulation framework enables a more systematic evaluation of the detectability limits and the robustness of signal interpretation across a wide range of anatomical sites, tumor types, and treatment plans.

The in-table detection system showed promising sensitivity in prostate cases, but its technical implementation in the treatment environment remains a challenge. Future work should address issues such as compatibility with patient positioning systems, interference with X-ray imaging workflows, and detector modularity. Experimental validation of its performance under realistic clinical conditions is a necessary step before integration into clinical practice.

Furthermore, improvements in reconstruction algorithms are crucial to enhance spatial resolution and reduce signal uncertainty. Optimization methods and machine learning techniques trained on MC simulations may offer avenues to improve FV reconstruction accuracy beyond the current closest-distance back-projection method. Techniques such as deconvolution of FV distributions can help resolve signal smearing caused by MCS, making deep-seated anatomical changes more distinguishable.

While this work incorporated gamma index analysis to explore the correlation between fragmentation signals and dose distribution changes, defining clear, clinically actionable thresholds remains an open question. Future studies should aim to integrate DVH-based evaluations to determine which anatomical changes justify treatment adaptation.

Taken together, and considering the demonstrated ability of Monte Carlo simulations to reproduce clinical scenarios in CIRT monitoring, including the possibility of conducting systematic studies without requiring multiple time-consuming in-beam experiments, these elements point to a promising path toward more comprehensive FV signal interpretation. This, in turn, could establish the monitoring method as a robust indicator of clinically relevant anatomical changes. Such progress could ultimately support the integration of fragmentation-based monitoring into adaptive radiotherapy workflows, either as a complementary or even primary tool for in-treatment decision-making.

Chapter 6

Summary and Conclusion

The primary goal of this thesis work was to develop and validate a Monte Carlo (MC)-based simulation framework for in-vivo monitoring in carbon-ion radiotherapy (CIRT), which was successfully achieved. The first milestone was the validation of the simulation against experimental data using a single mini-tracker and a homogeneous head-sized patient model. The results showed good agreement in terms of yield of fragments emerging from the head model, their angular distributions, and emission profiles. A residual difference of less than 4% in the number of fragments was achieved, confirming the precision and reliability of the simulation framework [22].

The framework was subsequently extended to model the full clinical detection system used in the ongoing InViMo clinical trial at the Heidelberg Ion Therapy Center (HIT). The system consists of seven mini-trackers that were further integrated with the FICTION framework, a CT-based Monte Carlo environment developed at HIT, enabling accurate patient-specific beam delivery, dose calculation, and fragment tracking simulations under realistic clinical conditions.

Given the complexity of the signals from detected fragment emissions, their interpretation remains a significant challenge. As discussed in the previous chapters, reconstructed fragmentation vertex (FV) distributions are affected by multiple factors, including the fragment energy, generation depth, multiple Coulomb scattering, the spatial configuration of the detection system, and the geometry of the mini-trackers. To better understand the observed signals, access to physical quantities that cannot be measured experimentally, such as the true locations of fragmentation vertices and nuclear interactions, is essential. A key strength of the developed MC framework is precisely this capability: it provides access to otherwise unobservable variables and enables a realistic simulation of the full CIRT monitoring process at HIT.

To assess the framework's applicability under clinical conditions and to gain a more comprehensive understanding of fragmentation signals, simulations were successfully performed for five retrospective patients, two patients monitored within the InViMo trial, and one prostate case. These simulations demonstrated that shallow regions, including mucosal swelling and nasal cavity filling, were successfully detected and localized using reconstructed fragmentation vertices. Deeper anatomical variations or changes located distant from the detector, including those near the end of range or far from the detection system,

were more difficult to detect using the standard clinical InViMo setup. Additional challenges arose when anatomical changes were either subtle or distributed across larger volumes. By simulating an in-table detector configuration, it was shown that reducing the fragment travel path significantly improves the detectability of deep-seated changes. This adaptation allowed clear identification of rectal filling differences in a prostate patient that were otherwise unresolved.

Furthermore, the robust performance of the method, along with growing interest from both clinical and industrial stakeholders, makes routine clinical integration increasingly plausible. The modular capabilities of the detector system, based on individual mini-trackers, allow for flexible adaptation to different treatment geometries and support integration into the treatment room through various configurations, such as couch-mounted, in-wall storage systems, and/or with rail-based portability, or robotic-arm-mounted systems. Moreover, machine learning or adaptive weighting strategies are promising candidates for a better exploration of the signals in order to increase the sensitivity and robustness of the monitoring method and the specificity of the signal.

In conclusion, the MC-based simulation framework developed in this thesis lays the groundwork for future investigations into secondary-fragment-based treatment verification. It offers a powerful platform to explore potential and fundamental limitations of the method, optimize detector designs and data analysis strategies, and ultimately boost the clinical adoption of in-vivo monitoring of CIRT into clinical routine.

Scientific Contributions

Peer-Reviewed Articles

- **P. Ochoa-Parra**, L. Schweins, R. Kirchgässner, M. Winter, S. Harrabi, A. Mairani, O. Jäkel, J. Debus, M. Martišíková, L. Kelleter.
  Experimental validation of a FLUKA Monte Carlo simulation for carbon-ion radiotherapy monitoring via secondary ion tracking. Medical Physics, 2024.

- L. Schweins, R. Kirchgässner, **P. Ochoa-Parra**, M. Winter, S. Harrabi, A. Mairani, O. Jäkel, J. Debus, M. Martišíková, L. Kelleter. *Detection of an internal density change in an anthropomorphic head phantom via tracking of charged nuclear fragments in carbon-ion radiotherapy*. Medical Physics, December 2024.

- L. Kelleter, L. Marek, G. Echner, **P. Ochoa-Parra**, M. Winter, S. Harrabi, J. Jakubek, O. Jäkel, J. Debus, M. Martišíková. *An in-vivo treatment monitoring system for ion-beam radiotherapy based on 28 Timepix3 detectors*. Scientific Reports, 2024.

- R. Félix-Bautista, L. Ghesquière-Diérickx, **P. Ochoa-Parra**, L. Kelleter, G. Echner, J. Debus, O. Jäkel, M. Martišíková, T. Gehrke. *Inhomogeneity detection within a head-sized phantom using tracking of charged nuclear fragments in ion beam therapy*.Physics in Medicine & Biology, 2024.

Proceedings

- **P. Ochoa-Parra**, L. Schweins, L. Marek, J. Jakubek, A. Mairani, G. Echner, M. Winter, O. Jäkel, J. Debus, M. Martišíková, and L. Kelleter. *Monte Carlo simulations of in-vivo carbon-ion treatment monitoring with charged nuclear fragments*. IEEE Nuclear Science Symposium, Medical Imaging Conference and International Symposium on Room-Temperature Semiconductor Detectors (NSS MIC RTSD), 2023.

Conferences

- **P. Ochoa-Parra**, L. Schweins, P. Schlegel, R. Kirchgässner, J. Jakubek, A. Mairani, M. Winter, S. Harrabi, O. Jäkel, J. Debus, M. Martišíková, L. Kelleter. *FLUKA Simulation for in-vivo monitoring of carbon-ion radiotherapy*. Poster presentation, Europian Congress of Medical Physics (ECMP), 2024.

- **P. Ochoa-Parra**, L. Schweins, P. Schlegel, R. Kirchgässner, L. Marek, J. Jakubek, A. Mairani, F. Dinkel, G. Echner, M. Winter, O. Jäkel, J. Debus, M. Martišíková, L. Kelleter. *FLUKA Simulation in Carbon-Ion in-vivo monitoring*. Poster presentation, 62nd Particle Therapy Co-Operative Group Conference (PTCOG), 2024.

- **P. Ochoa-Parra**, L. Schweins, L. Marek, J. Jakubek, A. Mairani, G. Echner, M. Winter, O. Jäkel, J. Debus, M. Martišíková, L. Kelleter. *Monte Carlo simulations of in-vivo carbon-ion treatment monitoring with charged nuclear fragments*. Oral presentation, IEEE Nuclear Science Symposium, Medical Imaging Conference and International Symposium on Room-Temperature Semiconductor Detectors (NSS MIC RTSD), 2023.

- **P. Ochoa-Parra**, L. Schweins, G. Echner, M. Winter, A. Mairani, O. Jäkel, J. Debus, L. Kelleter, M. Martišíková. *Monte Carlo simulations of in-vivo carbon-ion treatment monitoring with charged nuclear fragments*. Poster presentation, National Center for Radiation Research in Oncology (NCRO), 2023.

- **P. Ochoa-Parra**, L. Schweins, L. Kelleter, L. Ghesquière-Diérickx, N. Abbani, J. Debus, O. Jäkel, M. Martišíková. *Sensitivity to detector misalignment in carbon-ion treatment monitoring with charged nuclear fragments*. Poster presentation, 61st Particle Therapy Co-Operative Group Conference (PTCOG), 2023.

- **P. Ochoa-Parra**, L. Kelleter, L. Schweins, R. Félix-Bautista, J. Debus, O. Jäkel, G. Echner, T. Gehrke, M. Martišíková. *Sensitivity of Carbon-Ion Radiotherapy monitoring using charged nuclear fragments to detector positioning*. Poster presentation, 60th Particle Therapy Co-Operative Group Conference (PTCOG), 2022.

List of Figures

List of Tables

Bibliography

[1] Oliver Jäkel. Physical advantages of particles: protons and light ions. *The British Journal of Radiology*, 93(1107):20190428, March 2020.

[2] Marco Durante and Jürgen Debus. Heavy charged particles: Does improved precision and higher biological effectiveness translate to better outcome in patients? *Seminars in Radiation Oncology*, 28(2):160–167, 2018. Proton Radiation Therapy.

[3] Michael Moyers, Thomas Toth, Ramaswamy Sadagopan, Alexei Chvetsov, Jan Unkelbach, Radhe Mohan, David Lesyna, Liyong Lin, Zuofeng Li, Falk Poenisch, Wayne Newhauser, Stanislav Vatnitsky, and Jonathan Farr. *Physical Uncertainties in the Planning and Delivery of Light Ion Beam Treatments*. March 2020.

[4] Giovanni Fattori, Marco Riboldi, Emanuele Scifoni, Michael Krämer, Andrea Pella, Marco Durante, Sara Ronchi, Maria Bonora, Roberto Orecchia, and Guido Baroni. Dosimetric effects of residual uncertainties in carbon ion treatment of head chordoma. *Radiotherapy and Oncology*, 113(1):66–71, October 2014.

[5] Francesca Albertini, Michael Matter, Lena Nenoff, Ye Zhang, and Antony Lomax. Online daily adaptive proton therapy. *The British Journal of Radiology*, 93(1107), November 2019.

[6] Aafke Christine Kraan. Range verification methods in particle therapy: Underlying physics and monte carlo modeling. *Frontiers in Oncology*, 5, July 2015.

[7] Katia Parodi and Jerimy C. Polf. In vivo range verification in particle therapy. *Medical Physics*, 45(11), November 2018.

[8] Francesco Pennazio, G. Battistoni, Giuseppe Battistoni, Maria Giuseppina Bisogni, Niccolò Camarlinghi, Alfredo Ferrari, Alfredo Ferrari, Andrea C. Ferrari, Veronica Ferrero, Elisa Fiorina, Matteo Morrocchi, Paola Sala, Paola Sala, Giancarlo Sportelli, Richard Wheadon, Piergiorgio Cerello, Piergiorgio Cerello, Piergiorgio Cerello, Piergiorgio Cerello, Piergiorgio Cerello, Piergiorgio Cerello, and P. Cerello. Carbon ions beam therapy monitoring with the inside in-beam pet. *Physics in Medicine and Biology*, 2018.

[9] Akram Mohammadi, Hideaki Tashima, Yuma Iwao, Sodai Takyu, Go Akamatsu, Han Gyu Kang, Fumihiko Nishikido, Eiji Yoshida, Andrew Chacon, Mitra Safavi-Naeini, Katia Parodi, and Taiga Yamaya. Influence of momentum acceptance on range

monitoring of 11c and 15o ion beams using in-beam pet. *Physics in Medicine amp; Biology*, 65(12):125006, June 2020.

[10] Akram Hamato, Hideaki Tashima, Yuma Iwao, Sodai Takyu, Go Akamatsu, Han Gyu Kang, Fumihiko Nishikido, Katia Parodi, and Taiga Yamaya. Dose estimation using in-beam positron emission tomography: Demonstration for 11c and 15o ion beams. *Nuclear Instruments and Methods in Physics Research Section A: Accelerators, Spectrometers, Detectors and Associated Equipment*, 1066:169643, September 2024.

[11] J. Krimmer, D. Dauvergne, J.M. Létang, and É. Testa. Prompt-gamma monitoring in hadrontherapy: A review. *Nuclear Instruments and Methods in Physics Research Section A: Accelerators, Spectrometers, Detectors and Associated Equipment*, 878:58–73, January 2018.

[12] P Henriquet, E Testa, M Chevallier, D Dauvergne, G Dedes, N Freud, J Krimmer, J M Létang, C Ray, M-H Richard, and F Sauli. Interaction vertex imaging (ivi) for carbon ion therapy monitoring: a feasibility study. *Physics in Medicine Biology*, 57(14):4655, jul 2012.

[13] K Gwosch, B Hartmann, J Jakubek, C Granja, P Soukup, O Jäkel, and M Martišíková. Non-invasive monitoring of therapeutic carbon ion beams in a homogeneous phantom by tracking of secondary ions. *Physics in Medicine Biology*, 58(11):3755, may 2013.

[14] Laura Ghesquière-Diérickx, Annika Schlechter, Renato Félix-Bautista, Tim Gehrke, Gernot Echner, Laurent Kelleter, and M. Martisikova. Investigation of suitable detection angles for carbon-ion radiotherapy monitoring in depth by means of secondary-ion tracking. *Frontiers in Oncology*, 2021.

[15] Renato Félix-Bautista, Laura Ghesquière-Diérickx, Lukáš Marek, Carlos Granja, Pavel Soukup, Daniel Turecek, Laurent Kelleter, Stephan Brons, Malte Ellerbrock, Oliver Jäkel, Tim Gehrke, and Mária Martišíková. Quality assurance method for monitoring of lateral pencil beam positions in scanned carbon-ion radiotherapy using tracking of secondary ions. *Medical Physics*, 48(8):4411–4424, 2021.

[16] Laura Ghesquière-Diérickx, Renato Félix-Bautista, Annika Schlechter, Laurent Kelleter, Marvin Reimold, Gernot Echner, Pavel Soukup, Oliver Jäkel, Tim Gehrke, and Maria Martišíková. Detecting perturbations of a radiation field inside a head-sized phantom exposed to therapeutic carbon-ion beams through charged-fragment tracking. *Med. Phys.*, 49(3):1776–1792, March 2022.

[17] Renato Félix-Bautista, Laura Ghesquière-Diérickx, Pamela Ochoa-Parra, Laurent Kelleter, Gernot Echner, Jürgen Debus, Oliver Jäkel, Mária Martišíková, and Tim Gehrke. Inhomogeneity detection within a head-sized phantom using tracking of charged nuclear fragments in ion beam therapy. *Physics in Medicine amp; Biology*, 69(22):225003, November 2024.

[18] Luisa Schweins, Rebekka Kirchgässner, Pamela Ochoa-Parra, Marcus Winter, Semi Harrabi, Andrea Mairani, Oliver Jäkel, Jürgen Debus, Mária Martišíková, and Laurent

Kelleter. Detection of an internal density change in an anthropomorphic head phantom via tracking of charged nuclear fragments in carbon-ion radiotherapy. *Medical Physics*, December 2024.

[19] L. Kelleter, S. Schmidt, M. Subramanian, L. Marek, C. Granja, J. Jakubek, O. Jäkel, J. Debus, and M. Martisikova. Characterisation of a customised 4-chip timepix3 module for charged-particle tracking. *Radiation Measurements*, 173:107086, 2024.

[20] Laurent Kelleter, Lukas Marek, Gernot Echner, Pamela Ochoa-Parra, Marcus Winter, Semi Harrabi, Jan Jakubek, Oliver Jäkel, Jürgen Debus, and Maria Martisikova. An in-vivo treatment monitoring system for ion-beam radiotherapy based on 28 timepix3 detectors. *Scientific Reports*, 14(1), July 2024.

[21] R L Workman, V D Burkert, V Crede, E Klempt, U Thoma, L Tiator, K Agashe, G Aielli, B C Allanach, C Amsler, M Antonelli, E C Aschenauer, D M Asner, H Baer, Sw Banerjee, R M Barnett, L Baudis, C W Bauer, J J Beatty, V I Belousov, J Beringer, A Bettini, O Biebel, K M Black, E Blucher, R Bonventre, V V Bryzgalov, O Buchmuller, M A Bychkov, R N Cahn, M Carena, A Ceccucci, A Cerri, R Sekhar Chivukula, G Cowan, K Cranmer, O Cremonesi, G D'Ambrosio, T Damour, D de Florian, A de Gouvêa, T DeGrand, P de Jong, S Demers, B A Dobrescu, M D'Onofrio, M Doser, H K Dreiner, P Eerola, U Egede, S Eidelman, A X El-Khadra, J Ellis, S C Eno, J Erler, V V Ezhela, W Fetscher, B D Fields, A Freitas, H Gallagher, Y Gershtein, T Gherghetta, M C Gonzalez-Garcia, M Goodman, C Grab, A V Gritsan, C Grojean, D E Groom, M Grünewald, A Gurtu, T Gutsche, H E Haber, Matthieu Hamel, C Hanhart, S Hashimoto, Y Hayato, A Hebecker, S Heinemeyer, J J Hernández-Rey, K Hikasa, J Hisano, A Höcker, J Holder, L Hsu, J Huston, T Hyodo, Al Ianni, M Kado, M Karliner, U F Katz, M Kenzie, V A Khoze, S R Klein, F Krauss, M Kreps, P Križan, B Krusche, Y Kwon, O Lahav, J Laiho, L P Lellouch, J Lesgourgues, A R Liddle, Z Ligeti, C-J Lin, C Lippmann, T M Liss, L Littenberg, C Lourenço, K S Lugovsky, S B Lugovsky, A Lusiani, Y Makida, F Maltoni, T Mannel, A V Manohar, W J Marciano, A Masoni, J Matthews, U-G Meißner, I-A Melzer-Pellmann, M Mikhasenko, D J Miller, D Milstead, R E Mitchell, K Mönig, P Molaro, F Moortgat, M Moskovic, K Nakamura, M Narain, P Nason, S Navas, A Nelles, M Neubert, P Nevski, Y Nir, K A Olive, C Patrignani, J A Peacock, V A Petrov, E Pianori, A Pich, A Piepke, F Pietropaolo, A Pomarol, S Pordes, S Profumo, A Quadt, K Rabbertz, J Rademacker, G Raffelt, M Ramsey-Musolf, B N Ratcliff, P Richardson, A Ringwald, D J Robinson, S Roesler, S Rolli, A Romaniouk, L J Rosenberg, J L Rosner, G Rybka, M G Ryskin, R A Ryutin, Y Sakai, S Sarkar, F Sauli, O Schneider, S Schönert, K Scholberg, A J Schwartz, J Schwiening, D Scott, F Sefkow, U Seljak, V Sharma, S R Sharpe, V Shiltsev, G Signorelli, M Silari, F Simon, T Sjöstrand, P Skands, T Skwarnicki, G F Smoot, A Soffer, M S Sozzi, S Spanier, C Spiering, A Stahl, S L Stone, Y Sumino, M J Syphers, F Takahashi, M Tanabashi, J Tanaka, M Taševský, K Terao, K Terashi, J Terning, R S Thorne, M Titov, N P Tkachenko, D R Tovey, K Trabelsi, P Urquijo, G Valencia, R Van de Water, N Varelas, G Venanzoni, L Verde, I Vivarelli, P Vogel, W Vogelsang, V Vorobyev, S P Wakely, W Walkowiak, C W Walter, D Wands, D H

Weinberg, E J Weinberg, N Wermes, M White, L R Wiencke, S Willocq, C G Wohl, C L Woody, W-M Yao, M Yokoyama, R Yoshida, G Zanderighi, G P Zeller, O V Zenin, R-Y Zhu, Shi-Lin Zhu, F Zimmermann, and P A Zyla. Review of particle physics. *Progress of Theoretical and Experimental Physics*, 2022(8), August 2022.

[22] Pamela Ochoa-Parra, Luisa Schweins, Nelly Abbani, Laura Ghesquière-Diérickx, Tim Gehrke, Jan Jakubek, Lukas Marek, Carlos Granja, Fabian Dinkel, Gernot Echner, Marcus Winter, Andrea Mairani, Semi Harrabi, Oliver Jäkel, Jürgen Debus, Mária Martišíková, and Laurent Kelleter. Experimental validation of a fluka monte carlo simulation for carbon-ion radiotherapy monitoring via secondary ion tracking. *Medical Physics*, 51(12):9217–9229, September 2024.

[23] F Sommerer, D Unholtz, and S Brons. An easy-to-use monte carlo framework for ion therapy at heidelberg ion-beam therapy centre. 29th annual meeting of the european society for therapeutic. volume 96, page S481, 2010.

[24] Julia Bauer, Florian Sommerer, F Sommerer, Andrea Mairani, Andrea Mairani, D Unholtz, R Farook, J. Handrack, K Frey, T. Marcelos, Thomas Tessonnier, Swantje Ecker, Benjamin Ackermann, Benjamin Ackermann, M Ellerbrock, Jürgen Debus, Juergen Debus, and Katia Parodi. Integration and evaluation of automated monte carlo simulations in the clinical practice of scanned proton and carbon ion beam therapy. *Physics in Medicine and Biology*, 2014.

[25] Key data for ionizing-radiation dosimetry: Measurement standards and applications. Technical Report Report 90, International Commission on Radiation Units and Measurements (ICRU), Bethesda, MD, 2016.

[26] Stopping of ions heavier than helium. Technical Report Report 73, International Commission on Radiation Units and Measurements (ICRU), Bethesda, MD, 2005.

[27] Osama Mohamad, Brock Sishc, Janapriya Saha, Arnold Pompos, Asal Rahimi, Michael Story, Anthony Davis, and D W Kim. Carbon ion radiotherapy: A review of clinical experiences and preclinical research, with an emphasis on DNA damage/repair. *Cancers (Basel)*, 9(6):66, June 2017.

[28] Uli Weber and Gerhard Kraft. Comparison of carbon ions versus protons. *The Cancer Journal*, 15(4):325–332, July 2009.

[29] Matthias Uhl, Klaus Herfarth, and Jürgen Debus. Comparing the use of protons and carbon ions for treatment. *The Cancer Journal*, 20(6):433–439, November 2014.

[30] William T. Chu. Overview of light-ion beam therapy. 2006. Retrieved from eScholarship repository.

[31] Christian P Karger and Peter Peschke. Rbe and related modeling in carbon-ion therapy. *Physics in Medicine amp; Biology*, 63(1):01TR02, December 2017.

[32] O. Jäkel, G. H. Hartmann, C. P. Karger, P. Heeg, and J. Rassow. Quality assurance for a treatment planning system in scanned ion beam therapy. *Medical Physics*, 27(7):1588–1600, July 2000.

[33] O. Jäkel, C. Jacob, D. Schardt, C. P. Karger, and G. H. Hartmann. Relation between carbon ion ranges and x□ray ct numbers. *Medical Physics*, 28(4):701–703, April 2001.

[34] International Commission on Radiation Units and Measurements. *Prescribing, Recording, and Reporting Light Ion Beam Therapy*. ICRU 93 report. 2016.

[35] Piero Fossati, Silvia Molinelli, Naruhiru Matsufuji, Mario Ciocca, Alfredo Mirandola, Andrea Mairani, Junetsu Mizoe, Azusa Hasegawa, Reiko Imai, Tadashi Kamada, Roberto Orecchia, and Hirohiko Tsujii. Dose prescription in carbon ion radiotherapy: a planning study to compare nirs and lem approaches with a clinically-oriented strategy. *Physics in Medicine and Biology*, 57(22):7543–7554, October 2012.

[36] Stewart Mein, Carmen Klein, Benedikt Kopp, Giuseppe Magro, Semi Harrabi, Christian P. Karger, Thomas Haberer, Jürgen Debus, Amir Abdollahi, Ivana Dokic, and Andrea Mairani. Assessment of rbe-weighted dose models for carbon ion therapy toward modernization of clinical practice at hit: In vitro, in vivo, and in patients. *International Journal of Radiation Oncology - Biology - Physics*, 108(3):779–791, November 2020.

[37] Alexandra D Jensen, Marcus Winter, Sabine P Kuhn, Jürgen Debus, Olaf Nairz, and Marc W Münter. Robotic-based carbon ion therapy and patient positioning in 6 degrees of freedom: setup accuracy of two standard immobilization devices used in carbon ion therapy and imrt. *Radiation Oncology*, 7(1), March 2012.

[38] Veronica Ferrero, Elisa Fiorina, Matteo Morrocchi, Francesco Pennazio, Guido Baroni, G. Battistoni, Giuseppe Battistoni, Nicola Belcari, Niccolò Camarlinghi, Mario Ciocca, A. Del Guerra, Alberto Del Guerra, M. Donetti, Marco Donetti, Simona Giordanengo, Giuseppe Giraudo, Vincenzo Patera, Cristiana Peroni, Angelo Rivetti, Angelo Rivetti, M. Rolo, M. Rolo, Sandro Rossi, Valeria Rosso, Giancarlo Sportelli, Sara Tampellini, Francesca Valvo, Richard Wheadon, Piergiorgio Cerello, Piergiorgio Cerello, Piergiorgio Cerello, Piergiorgio Cerello, Piergiorgio Cerello, Piergiorgio Cerello, P. Cerello, and Maria Giuseppina Bisogni. Online proton therapy monitoring: clinical test of a silicon-photodetector-based in-beam pet. *Scientific Reports*, 2018.

[39] A.C. Kraan, G. Battistoni, N. Belcari, N. Camarlinghi, G.A.P. Cirrone, G. Cuttone, S. Ferretti, A. Ferrari, G. Pirrone, F. Romano, P. Sala, G. Sportelli, K. Straub, A. Tramontana, A. Del Guerra, and V. Rosso. Proton range monitoring with in-beam pet: Monte carlo activity predictions and comparison with cyclotron data. *Physica Medica*, 30(5):559–569, July 2014.

[40] W Enghardt, P Crespo, F Fiedler, R Hinz, K Parodi, J Pawelke, and F Pönisch. Charged hadron tumour therapy monitoring by means of pet. *Nuclear Instruments and Methods in Physics Research Section A: Accelerators, Spectrometers, Detectors and Associated Equipment*, 525(1):284–288, 2004. Proceedings of the International Conference

on Imaging Techniques in Subatomic Physics, Astrophysics, Medicine, Biology and Industry.

[41] Teiji Nishio, Takashi Ogino, Kazuhiro Nomura, and Hiroshi Uchida. Dose□volume delivery guided proton therapy using beam on□line pet system. *Medical Physics*, 33(11):4190–4197, October 2006.

[42] Katia Parodi, Harald Paganetti, Helen A. Shih, Susan Michaud, Jay S. Loeffler, Thomas F. DeLaney, Norbert J. Liebsch, John E. Munzenrider, Alan J. Fischman, Antje Knopf, and Thomas Bortfeld. Patient study of in vivo verification of beam delivery and range, using positron emission tomography and computed tomography imaging after proton therapy. *International Journal of Radiation Oncology - Biology - Physics*, 68(3):920–934, July 2007.

[43] T Hofmann, A. Fochi, Katia Parodi, and Marco Pinto. Prediction of positron emitter distributions for range monitoring in carbon ion therapy: an analytical approach. *Physics in Medicine and Biology*, 2019.

[44] K. Parodi. Pet monitoring of hadrontherapy. *Nuclear Medicine Review*, 15:C37–C42, 01 2012.

[45] Georgy Shakirin, Henning Braess, Fine Fiedler, Daniela Kunath, Kristin Laube, Katia Parodi, Marlen Priegnitz, and Wolfgang Enghardt. Implementation and workflow for pet monitoring of therapeutic ion irradiation: a comparison of in-beam, in-room, and off-line techniques. *Physics in Medicine and Biology*, 56(5):1281–1298, February 2011.

[46] Hyun Joon Choi, Ji Won Jang, Wook-Geun Shin, Hyojun Park, Sebastien Incerti, and Chul Hee Min. Development of integrated prompt gamma imaging and positron emission tomography system for in vivo 3-d dose verification: a monte carlo study. *Physics in Medicine amp; Biology*, 65(10):105005, May 2020.

[47] Javier Balibrea-Correa, Jorge Lerendegui-Marco, Ion Ladarescu, Carlos Guerrero, Teresa Rodríguez-González, Maria del Carmen Jiménez-Ramos, Begoña Fernández-Martínez, and César Domingo-Pardo. Hybrid in-beam pet- and compton prompt-gamma imaging aimed at enhanced proton-range verification, 2022.

[48] M. Bisogni. The inside bimodal system for range monitoring in particle therapy toward clinical validation. *Nuclear Instruments and Methods in Physics Research Section A: Accelerators, Spectrometers, Detectors and Associated Equipment*, 936:73–74, 2019. Frontier Detectors for Frontier Physics: 14th Pisa Meeting on Advanced Detectors.

[49] M. Pinto, M. De Rydt, D. Dauvergne, G. Dedes, N. Freud, J. Krimmer, J. M. Létang, C. Ray, E. Testa, and M. Testa. Technical note: Experimental carbon ion range verification in inhomogeneous phantoms using prompt gammas. *Medical Physics*, 42(5):2342–2346, May 2015.

[50] Christian Golnik, Fernando Hueso-González, Andreas Müller, Peter Dendooven, Wolfgang Enghardt, Fine Fiedler, Thomas Kormoll, Katja Roemer, Johannes Petzoldt, Andreas Wagner, and Guntram Pausch. Range assessment in particle therapy based on promptγ-ray timing measurements. *Physics in Medicine and Biology*, 59(18):5399–5422, August 2014.

[51] J. Krimmer, G. Angellier, L. Balleyguier, D. Dauvergne, N. Freud, J. Hérault, J. M. Létang, H. Mathez, M. Pinto, E. Testa, and Y. Zoccarato. A cost-effective monitoring technique in particle therapy via uncollimated prompt gamma peak integration. *Applied Physics Letters*, 110(15), April 2017.

[52] Riccardo Dal Bello, Paulo Magalhaes Martins, Stephan Brons, German Hermann, Thomas Kihm, Michael Seimetz, and Joao Seco. Prompt gamma spectroscopy for absolute range verification of 12c ions at synchrotron-based facilities. *Physics in Medicine amp; Biology*, 65(9):095010, May 2020.

[53] Fernando Hueso-González, Fine Fiedler, Christian Golnik, Thomas Kormoll, Guntram Pausch, Johannes Petzoldt, Katja E. Römer, and Wolfgang Enghardt. Compton camera and prompt gamma ray timing: Two methods for in vivo range assessment in proton therapy. *Frontiers in Oncology*, 6, April 2016.

[54] Andrea Missaglia, Aicha Bourkadi-Idrissi, Francesco Casamichiela, Davide Mazzucconi, Marco Carminati, Stefano Agosteo, and Carlo Fiorini. Prompt-gamma fall-off estimation with c-ion irradiation at clinical energies, using a knife-edge slit camera: A monte carlo study. *Physica Medica*, 107:102554, March 2023.

[55] Aicha Bourkadi Idrissi, Giacomo Borghi, Anita Caracciolo, Christian Riboldi, Marco Carminati, Marco Donetti, Marco Pullia, Simone Savazzi, Franco Camera, and Carlo Fiorini. First experimental verification of prompt gamma imaging with carbon ion irradiation. *Scientific Reports*, 14(1), October 2024.

[56] Luca Piersanti, F. Bellini, F. Bellini, F. Bini, Fabiano Bini, Francesco Collamati, Francesco Collamati, E. De Lucia, Marco Durante, Marco Durante, R. Faccini, R. Faccini, F. Ferroni, S. Fiore, E. Iarocci, E. Iarocci, C. La Tessa, C. La Tessa, M. Marafini, Michela Marafini, Ilaria Mattei, I. Mattei, V. Patera, Pablo G. Ortega, Alessio Sarti, Alessio Sarti, C. Schuy, C. Schuy, Adalberto Sciubba, M. Vanstalle, C. Voena, and C. Voena. Measurement of charged particle yields from pmma irradiated by a 220 mev/u (12)c beam. *Physics in Medicine and Biology*, 2014.

[57] Giacomo Traini, Giacomo Traini, Giacomo Traini, G. Battistoni, Giuseppe Battistoni, Angela Bollella, Francesco Collamati, Francesco Collamati, Erika De Lucia, R. Faccini, Riccardo Faccini, F. Ferroni, Fernando Ferroni, P.M. Frallicciardi, C. Mancini-Terracciano, Carlo Mancini-Terracciano, Michela Marafini, M. Marafini, Michela Marafini, Ilaria Mattei, Ilaria Mattei, Federico Miraglia, Silvia Muraro, S. Muraro, S. Muraro, Riccardo Paramatti, Riccardo Paramatti, Riccardo Paramatti, Luca Piersanti, L. Piersanti, D. Pinci, Davide Pinci, Davide Pinci, Davide Pinci, A. Rucinski,

A. Russomando, Alessio Sarti, Alessio Sarti, Adalberto Sciubba, A. Sciubba, M. Senzacqua, Elena Solfaroli Camillocci, Elena Solfaroli-Camillocci, M. Toppi, C. Voena, C. Voena, and Vincenzo Patera. Design of a new tracking device for on-line beam range monitor in carbon therapy. *Physica Medica*, 2017.

[58] M. Fischetti, G. Baroni, G. Battistoni, G. Bisogni, P. Cerello, M. Ciocca, P. De Maria, M. De Simoni, B. Di Lullo, M. Donetti, Y. Dong, A. Embriaco, V. Ferrero, E. Fiorina, G. Franciosini, F. Galante, A. Kraan, C. Luongo, M. Magi, C. Mancini-Terracciano, M. Marafini, E. Malekzadeh, I. Mattei, E. Mazzoni, R. Mirabelli, A. Mirandola, M. Morrocchi, S. Muraro, V. Patera, F. Pennazio, A. Schiavi, A. Sciubba, E. Solfaroli Camillocci, G. Sportelli, S. Tampellini, M. Toppi, G. Traini, S. M. Valle, B. Vischioni, V. Vitolo, and A. Sarti. Inter-fractional monitoring of 12C ions treatments: results from a clinical trial at the cnao facility. *Scientific Reports*, 10(1), November 2020.

[59] Marco Toppi, Guido Baroni, Giuseppe Battistoni, Maria Giuseppina Bisogni, Piergiorgio Cerello, Mario Ciocca, Patrizia De Maria, Micol De Simoni, Marco Donetti, Yunsheng Dong, Alessia Embriaco, Veronica Ferrero, Elisa Fiorina, Marta Fischetti, Gaia Franciosini, Aafke Christine Kraan, Carmela Luongo, Etesam Malekzadeh, Marco Magi, Carlo Mancini-Terracciano, Michela Marafini, Ilaria Mattei, Enrico Mazzoni, Riccardo Mirabelli, Alfredo Mirandola, Matteo Morrocchi, Silvia Muraro, Vincenzo Patera, Francesco Pennazio, Angelo Schiavi, Adalberto Sciubba, Elena Solfaroli-Camillocci, Giancarlo Sportelli, Sara Tampellini, Giacomo Traini, Serena Marta Valle, Barbara Vischioni, Viviana Vitolo, and Alessio Sarti. Monitoring carbon ion beams transverse position detecting charged secondary fragments: Results from patient treatment performed at cnao. *Frontiers in Oncology*, 11, June 2021.

[60] Claire-Anne Reidel, Enrico Pierobon, Felix Horst, Lévana Gesson, Athena Paz, Christian Graeff, Timo Steinsberger, Klemens Zink, Matthias Witt, Yannick Senger, Christian Finck, Marie Vanstalle, Chiara La Tessa, Marco Durante, Uli Weber, and Christoph Schuy. Feasibility study of 4d-online monitoring of density gradients induced by lung cancer treatment using carbon ions. *Frontiers in Oncology*, 15, February 2025.

[61] Glenn F Knoll. *Radiation detection and measurement; 4th ed.* Wiley, New York, NY, 2010.

[62] J Jakůbek. Semiconductor pixel detectors and their applications in life sciences. *Journal of Instrumentation*, 4(03):P03013–P03013, March 2009.

[63] Joao Seco and Frank Verhaegen, editors. *Monte Carlo Techniques in Radiation Therapy*. CRC Press, Boca Raton, 2013.

[64] Alireza Haghighat. *Monte Carlo Methods for Particle Transport*. CRC Press, 2020.

[65] Nicholas A. Gentile. Monte carlo particle transport: Algorithm and performance overview. *Proceedings of the 5th International Conference on Transport Phenomena in Multiphase Systems*, 2005.

[66] William H. Press, Saul A. Teukolsky, William T. Vetterling, and Brian P. Flannery. *Numerical Recipes: The Art of Scientific Computing*. Cambridge University Press, 3rd edition, 2007.

[67] Donald E. Knuth. *The Art of Computer Programming, Volume 2: Seminumerical Algorithms*. Addison-Wesley, 3rd edition, 1997.

[68] Thomas E. Booth. Monte carlo variance reduction for radiation transport in medical physics. *Physics in Medicine and Biology*, 52(15):R93–R112, 2007.

[69] R. A. Forster and A. Haghighat. A review of variance reduction techniques for monte carlo simulation. *Progress in Nuclear Energy*, 51(4):360–379, 2009.

[70] Andreas Peters. *The accelerator facility of the Heidelberg Ion-Beam Therapy Centre (HIT)*, page 801–812. World Scientific, February 2016.

[71] Heidelberger Ionenstrahl-Therapiezentrum (HIT), Universitätklinikum Heidelberg. `https://www.klinikum.uni-heidelberg.de/interdisziplinaere-zentren/heidelberger-ionenstrahl-therapiezentrum-hit`. [Accessed 24-01-2025].

[72] Th. Haberer, W. Becher, D. Schardt, and G. Kraft. Magnetic scanning system for heavy ion therapy. *Nuclear Instruments and Methods in Physics Research Section A: Accelerators, Spectrometers, Detectors and Associated Equipment*, 330(1):296–305, 1993.

[73] Uli Weber and Gerhard Kraft. Design and construction of a ripple filter for a smoothed depth dose distribution in conformal particle therapy. *Physics in Medicine and Biology*, 44(11):2765–2775, October 1999.

[74] K Parodi, A Mairani, S Brons, B G Hasch, F Sommerer, J Naumann, O Jäkel, T Haberer, and J Debus. Monte carlo simulations to support start-up and treatment planning of scanned proton and carbon ion therapy at a synchrotron-based facility. *Physics in Medicine Biology*, 57(12):3759, may 2012.

[75] ADVACAM s.r.o. *Preliminary AdvaPIX TPX3 Quad Datasheet*, August 2022.

[76] Computerized Imaging Reference Systems Inc. *Proton Therapy Dosimetry Head Model 731HN* . Computerized Imaging Reference Systems Inc. (CIRS), Norfolk, VA, USA, 2013. Publication: 731HN DS 072220.

[77] Sala P Ferrari A, Fasso A, and Ranft J. Fluka: a multi-particle transport code Technical Report CERN-2005-10, INFN/tc 05/11, SLAC-R-773 CERN, INFN, SLAC, Menlo Park. 2005.

[78] T.T. Böhlen, F. Cerutti, M.P.W. Chin, A. Fassò, A. Ferrari, P.G. Ortega, A. Mairani, P.R. Sala, G. Smirnov, and V. Vlachoudis. The fluka code: Developments and challenges for high energy and medical applications. *Nuclear Data Sheets*, 120:211–214, 2014.

[79] Wioletta Kozlowska, , T.T. Böhlen, Caterina Cuccagna, Alfredo Ferrari, Andrea C. Ferrari, F. Fracchiolla, Giuseppe Magro, Andrea Mairani, Marco Schwarz, Vasilis Vlachoudis, and Dietmar Georg. Fluka particle therapy tool for monte carlo independent calculation of scanned proton and carbon ion beam therapy. *Physics in Medicine and Biology*, 2019.

[80] Giuseppe Battistoni, Julia Bauer, Till T. Boehlen, Francesco Cerutti, Mary P. W. Chin, Ricardo Dos Santos Augusto, Alfredo Ferrari, Pablo G. Ortega, Wioletta Kozłowska, Giuseppe Magro, Andrea Mairani, Katia Parodi, Paola R. Sala, Philippe Schoofs, Thomas Tessonnier, and Vasilis Vlachoudis. The fluka code: An accurate simulation tool for particle therapy. *Frontiers in Oncology*, 6, 2016.

[81] V. Andersen, F. Ballarini, G. Battistoni, M. Campanella, M. Carboni, F. Cerutti, A. Empl, A. Fassò, A. Ferrari, E. Gadioli, M.V. Garzelli, K. Lee, A. Ottolenghi, M. Pelliccioni, L.S. Pinsky, J. Ranft, S. Roesler, P.R. Sala, and T.L. Wilson. The fluka code for space applications: recent developments. *Advances in Space Research*, 34(6):1302–1310, 2004. Space Life Sciences: Radiation Risk Assessment and Radiation Measurements in Low Earth Orbit.

[82] F Cerutti, F Ballarini, G Battistoni, P Colleoni, A Ferrari, S V Förtsch, E Gadioli, M V Garzelli, A Mairani, A Ottolenghi, A Pepe, L S Pinsky, P R Sala, D Scannicchio, and G F Steyn. Carbon induced reactions at low incident energies. *Journal of Physics: Conference Series*, 41:212–218, May 2006.

[83] K Parodi, A Ferrari, F Sommerer, and H Paganetti. Clinical ct-based calculations of dose and positron emitter distributions in proton therapy using the fluka monte carlo code. *Physics in Medicine and Biology*, 52(12):3369–3387, May 2007.

[84] Katia Parodi, Harald Paganetti, Ethan Cascio, Jacob B Flanz, Ali A Bonab, Nathaniel M Alpert, Kevin Lohmann, and Thomas Bortfeld. Pet/ct imaging for treatment verification after proton therapy: a study with plastic phantoms and metallic implants. *Medical physics*, 34(2):419–435, 2007.

[85] Uli Weber and Gerhard Kraft. Design and construction of a ripple filter for a smoothed depth dose distribution in conformal particle therapy. *Physics in Medicine Biology*, 44(11):2765, nov 1999.

[86] G Battistoni, TT Böhlen, F Cerutti, PW Chin, LS Esposito, A Fassò, A Ferrari, PG Ortega, A Mairani, PR Sala, et al. Overview of the fluka code. *Annals of Nuclear Energy*, 82:10–18, 2015.

[87] K Gunzert-Marx, H Iwase, D Schardt, and R S Simon. Secondary beam fragments produced by 200 mev/u-12c ions in water and their dose contributions in carbon ion radiotherapy. *New Journal of Physics*, 10(7):075003, July 2008.

[88] Timothy D. Malouff, Anita Mahajan, Sunil Krishnan, Chris Beltran, Danushka S. Seneviratne, and Daniel Michael Trifiletti. Carbon ion therapy: A modern review of an emerging technology. *Frontiers in Oncology*, 10, February 2020.

[89] Hitoshi Ishikawa, Yuichi Hiroshima, Nobuyuki Kanematsu, Taku Inaniwa, Toshiyuki Shirai, Reiko Imai, Hiroyoshi Suzuki, Koichiro Akakura, Masaru Wakatsuki, Tomohiko Ichikawa, and Hiroshi Tsuji. Carbon□ion radiotherapy for urological cancers. *International Journal of Urology*, 29(10):1109–1119, June 2022.

[90] Laura Marie Hélène Ghesquière-Diérickx. *Carbon-ion radiotherapy monitoring in depth using secondary ion tracking*. Dissertation, Heidelberg University, 2022.

[91] Improvement of fragmentation-vertex reconstruction in carbon-ion treatment monitoring based on monte carlo simulations. *International Journal of Particle Therapy*, 10(2):118–396, November 2023. Proceedings to the 61nd Annual Conference of the Particle Therapy Cooperative Group (PTCOG).

[92] Xue Chen, Qi Yu, Ping Li, and Shen Fu. Landscape of carbon ion radiotherapy in prostate cancer: Clinical application and translational research. *Frontiers in Oncology*, 11, November 2021.

[93] Stefania Russo, Rosalinda Ricotti, Silvia Molinelli, Filippo Patti, Amelia Barcellini, Edoardo Mastella, Andrea Pella, Chiara Paganelli, Giulia Marvaso, Matteo Pepa, Stefania Comi, Mattia Zaffaroni, Barbara Avuzzi, Tommaso Giandini, Emanuele Pignoli, Riccardo Valdagni, Guido Baroni, Federica Cattani, Mario Ciocca, Barbara Alicja Jereczek-Fossa, Ester Orlandi, Roberto Orecchia, and Barbara Vischioni. Dosimetric impact of inter-fraction anatomical changes in carbon ion boost treatment for high-risk prostate cancer (airc ig 14300). *Frontiers in Oncology*, 11, September 2021.

Acknowledgments

First and foremost, I would like to express my sincere gratitude to Prof. Dr. Oliver Jäkel and Dr. Mária Martišíková for accepting me into the Medical Physics in Radiation Oncology division at the German Cancer Research Center (DKFZ). Their support, guidance, and trust have been invaluable throughout my doctoral journey.

I would also like to thank Prof. Dr. Ladd for kindly accepting the role of referee for this thesis.

My heartfelt thanks go to all my colleagues in the Medical Physics in Radiation Oncology division at DKFZ. In particular, I am especially grateful to my research group, Novel Detection Techniques in Ion Beam Therapy, for their support and collaboration. Special thanks to Tim, Margareta, Rebekka, and Patrice for their continuous encouragement, scientific discussions, and camaraderie. I also acknowledge the contributions of all the Master's and Bachelor's students who joined our group, especially Luisa, whose dedication and commitment to simulations played a key role in shaping this work.

I would like to extend my sincere appreciation to the staff of the Heidelberg Ion Beam Therapy Center (HIT) for their support during the measurements and throughout all phases of this project. In particular, I am especially grateful to PD Dr. med. Semi Harrabi, Dr. Stephan Brons, and Dr. Andrea Mairani, their expertise, kindness, and unwavering commitment were crucial to the successful execution of this research.

I also wish to express my deepest gratitude to my former mentors, Dr. Stella Velloza and Dr. Fernando Cristancho from the National University of Colombia, who laid the foundation for my career as a researcher. More than just teaching me the principles of science, they opened doors, windows, and every possible path for me to reach my full potential. Their encouragement and belief in my abilities have been instrumental in this journey. To my lifelong friends from Colombia, now spread across the world, who, even from afar, have been my greatest supporters, always there to encourage and accompany me every step of the way.

Beyond the academic sphere, this PhD has gifted me with incredible friendships. Daniel, Iván, Luis, Yasmin, Sonja, Anahita, Mathieu, and many more, you have all made this experience truly unforgettable. Your companionship, support, and shared moments of joy have been my safe harbor throughout these years.

This dissertation is dedicated to my nana, María Inés Ochoa Suárez, who cared for me while my mother worked tirelessly. She taught me how to tie my shoelaces so I could take firm and giant steps, so that the world would not feel too big for me. Her lessons have carried me across oceans, and for that, I am eternally grateful. Tía, I love you and miss you dearly. Your love and wisdom continue to guide me every day, and I am forever thankful

for the foundation you gave me.

To my mother and my brother, I owe everything. Your unconditional support, unwavering belief in me, and countless sacrifices have made this possible. To my father, thank you for passing down your curiosity and your passion for learning. Despite the distance, your love and encouragement have always been present. To my stepfather, thank you for being a constant source of guidance and for always having my back. Your support has been invaluable to me.

I want to give a special mention to my much beloved cats, Pacha and Fausto. Feline energy is a kind of magic, and their presence has been a gentle, constant lesson in love. Despite the distance, they remain a source of comfort, joy, and stress relief. I carry them with me every day. I miss them more than words can say.

To my life partner, who has walked with me through every twist and turn of this PhD, thank you for your patience, love, and steadfast companionship. This journey would not have been the same without you.

And finally, I want to express my deepest gratitude to myself. For facing fears, for enduring the uncertainties, and for pushing forward despite illness, setbacks, and doubts. I celebrate myself for continuing to work toward becoming the person I aspire to be.

We did it, Dr. Ochoa-Parra.